Stochastic Model and Simulation of Near Fault Ground Motions for Specified Earthquake Source and Site Characteristics

Mayssa Dabaghi

Armen Der Kiureghian

Department of Civil and Environmental Engineering

University of California, Berkeley

Report to Sponsor

California Department of Transportation

December 2011

ABSTRACT

Near-fault ground motions often possess distinct characteristics, which can have strong influence on structural response. These include the rupture directivity effect in the fault-normal direction and the fling step in the fault-parallel direction. A site in the near-field region of the fault may experience forward directivity when the fault rupture propagates towards the site with a velocity almost equal to the shear-wave velocity of the ground medium. The resulting ground motion typically exhibits a two-sided, long-period, large-amplitude velocity pulse in the fault-normal direction. Backward directivity occurs when the fault rupture propagates away from the site. The resulting ground motion tends to be of low intensity and long duration. The fling step is caused by the permanent displacement of the fault and is usually characterized by a one-sided velocity pulse in the fault-parallel direction.

Due to scarcity of recorded near-fault ground motions, there is interest in developing synthetic ground motions for near-fault sites, which can be used in performance-based earthquake engineering in addition to or in place of recorded motions. It is crucial that such synthetic motions be realistic and have characteristics that are consistent with recorded near-fault ground motions. Furthermore, from a practical standpoint, it is most useful if the synthetic motions are generated in terms of information that is normally available to the design engineer. This information typically includes the type of faulting, the earthquake magnitude, the position of the site relative to the potential fault rupture, and the shear-wave velocity of the soil at the site.

In this report we develop a parameterized stochastic model of near-fault ground motion in the strike-normal direction. Not all near-fault ground motions contain a forward directivity pulse, and our model is developed to account for the pulselike and non-pulselike cases. By fitting the model to a database of near-fault ground motions, we develop predictive equations for the model parameters in terms of the earthquake source and site characteristics mentioned above. Using these predictive equations, for a given set of earthquake and site characteristics, we generate sets of model parameters and use them to generate an ensemble of synthetic near-fault ground motions. The resulting synthetic motions have the same statistical characteristics as the motions in the database, including the variability for the given set of earthquake and site characteristics. For illustration of the methodology, a set of synthetic motions for specified earthquake source and site characteristics are generated and their characteristics are compared with those of recorded motions.

ACKNOWLEDGMENTS

This work was supported by the California Department of Transportation under Contract No. 59A0582. The authors gratefully acknowledge this support. Additional support was provided by the Taisei Chair in Civil Engineering at the University of California, Berkeley.

We thank Professor Jack Baker and Shrey Shahi for providing us with their pulse-extraction code and with the extracted pulses and residuals of our database as well as for their consultation during the course of this study. We also thank Dr. Yousef Bozorgnia for valuable discussion during the course of this study.

TABLE OF CONTENTS

LIST OF FIGURES

LIST OF TABLES

1 Introduction

1.1 MOTIVATION, OBJECTIVE AND SCOPE

Near-fault ground motions often possess distinct characteristics, which can have strong influence on structural response. These include the rupture directivity effect in the fault-normal direction and the fling step in the fault-parallel direction. A site in the near-field region of the fault may experience forward directivity, which occurs when the fault rupture propagates towards the site with a velocity almost equal to the shear-wave velocity. The resulting ground motion typically exhibits a large velocity pulse, which may impose extreme demands on a structure. Forward directivity is typically characterized by the presence of a two-sided, long-period, large-amplitude velocity pulse in the fault-normal direction. Backward directivity occurs when the fault rupture propagates away from the site. The resulting ground motion tends to be of low intensity and long duration. The fling step is caused by the permanent displacement of the fault and is usually characterized by a one-sided velocity pulse in the fault-parallel direction.

Due to scarcity of recorded near-fault ground motions, there is interest in developing synthetic ground motions for near-fault sites, which can be used in performance-based earthquake engineering in addition to or in place of recorded motions. Obviously, it is crucial that such synthetic motions be realistic and have characteristics that are consistent with recorded near-fault ground motions. Furthermore, from a practical standpoint, it is most useful if the synthetic motions are generated in terms of information that is normally available to the design engineer. This information typically includes the type of faulting, the earthquake magnitude, the position of the site relative to the potential fault rupture, and the shear-wave velocity of the soil at the site.

Our objective in this study is to develop a parameterized stochastic model of near-fault ground motion in the strike-normal direction and use it to generate synthetic motions. Not all near-fault ground motions contain a forward directivity pulse, even when the conditions for such a pulse are favorable. The model proposed in this study allows consideration of both pulselike and non-pulselike motions in the same proportions as they occur among recorded near-fault ground motions for a given design scenario. The model for the pulselike motion consists of two parts: a model for the velocity pulse and a model for the residual motion, which is defined as the total ground acceleration minus the derivative of the velocity pulse. The model for the non-pulselike motion is similar in form to that of the residual component of

pulselike motions. By fitting the model to a database of near-fault ground motions, we develop predictive equations for the model parameters in terms of the earthquake source and site characteristics mentioned above. Using these predictive equations, for a given set of earthquake source and site characteristics, we generate sets of model parameters and use them to generate an ensemble of synthetic near-fault ground motions. The resulting synthetic motions have the same statistical characteristics as the motions in the database, including the record-to-record variability for the given set of earthquake source and site characteristics.

The eventual goal of our study is to generate synthetic near-fault ground motions in three components: strike-normal, strike-parallel and vertical. Furthermore, for analysis and design of bridges in near-fault regions, we wish to develop synthetic arrays of near-fault ground motions at multiple sites, including the effects of spatial variability that arise from wave passage and incoherence. The present report is focused only on the strike-normal component of the ground motion at one site. A continuing study will focus on the other components of the near-fault ground motion and on characterization of the spatial variability effects.

1.2 ORGANIZATION OF THE REPORT

After this introductory chapter, Chapter 2 gives a review of the state-of-the-art on characterization and modeling of near-fault ground motions. It starts with a discussion of the physics of near-fault ground motions. It then presents some of the spectral and time history models proposed in literature that account for the forward directivity effect. It lastly describes available models to compute the probability of occurrence of a forward directivity pulse and to predict the fling step.

In Chapter 3, a parameterized stochastic model of the near-fault ground motion in the strike-normal direction is developed. In the case of a pulselike ground motion, the stochastic model consists of two sub-models: (a) A 5-parameter modified version of the idealized velocity pulse model earlier developed by Mavroeidis and Papageorgiou (2003), and (b) the non-stationary filtered white-noise model formulated by Rezaeian and Der Kiureghian (2008) with a modified modulating function and a total of 7 parameters for the residual motion. In the absence of a pulse, the 7-parameter non-stationary filtered white-noise model by Rezaeian and Der Kiureghian (2008) is directly used to model the ground motion. The chapter also provides a review of alternative models proposed in the literature and describes the wavelet-based pulse extraction algorithm developed by Baker (2007), which is employed in later chapters.

In Chapter 4, the database of strike-normal, near-fault, pulselike ground motions used in the study is presented. Each ground motion record is decomposed into the pulse, extracted using Baker's algorithm (2007), and the residual motion. For each record in the database, the 12 parameters of the two sub-models are identified by fitting the pulse and residual models to the recorded counterparts. The samples of identified parameter values are fitted marginal distributions, which are then used to transform the parameter values to the standard normal space. Empirical predictive equations in terms of the earthquake source and site characteristics are then developed for the transformed model parameters by regression analysis. Estimated correlation coefficients between the regression residuals provide estimates of the correlations between the model parameters in the normal space.

Chapter 5 presents the procedure for simulating a synthetic pulselike ground motion. Two types of synthetic ground motions are investigated: (a) Synthetic motions generated using model parameters that are obtained by fitting the model to a recorded motion. These motions essentially represent different realizations of near-fault ground motions for the same earthquake. (b) Synthetic motions generated using randomly selected values of the model parameters for prescribed earthquake source and site characteristics, generated according to the predictive regression equations and estimated correlation coefficients. These motions represent realizations of near-fault ground motions from different earthquakes with similar source and site characteristics. Synthetic motions using both approaches are generated and compared with corresponding recorded motions. Comparisons are made between recorded and simulated pulses and residual motions, as well as the corresponding total acceleration, velocity and displacement time histories. Furthermore, response spectra of recorded and synthetic motions are compared and their characteristics are discussed. Although non-pulselike ground motions have not yet been fitted directly to a database, the model can also be used to simulate such motions. Finally, the inclusion of a model to compute the probability of occurrence of a pulse into the simulation procedure is described.

Chapter 6 summarizes the major findings and conclusions of the study. It also describes the limitations of the model and lists a number of improvements that can be undertaken.

2 Review of State of the Art

2.1 INTRODUCTION

It has been observed that earthquake ground motion recordings in the near fault region, here taken as within 30km from the fault rupture, often significantly differ from recordings of far field ground motions. Differences are usually observed in the velocity and displacement time histories and have been attributed to two effects: the rupture directivity effect and the fling step. The rupture directivity effect often manifests in the fault-normal (FN) direction, which is the direction perpendicular to the surface of the fault rupture. As illustrated in Figure 2.1, this effect appears in the form of a large, long-period velocity pulse. The fling step is observed in the fault-parallel (FP) direction, i.e., the direction parallel to the direction of slip, and appears in the form of a permanent displacement. These effects, especially the rupture directivity effect, result in large spatial variations in the amplitude and duration of near-fault ground motions, as well as in significant differences between the horizontal strike-normal (SN) and strike-parallel (SP) components. Note that when a fault is vertical and of strike slip type, then the FN direction coincides with the SN direction, and the SP direction coincides with the FP direction. In Figure 2.2, the SN component of the ground motion (which is also the FN component because the fault is vertical and strike slip) during the 1992 Landers earthquake is clearly variable at the two near-fault locations of Lucerne and Joshua Tree. While the Lucerne site, which is located in the direction of propagation of the rupture, records a large amplitude, short duration two-sided velocity pulse, the Joshua Tree site, which is located near the epicenter and away from the direction of propagation of the rupture, records a small amplitude long duration velocity time history. The differences between the SN and SP components (same as the FN and FP components in this case) can be noticed in Figure 2.1, with two-sided and one-sided velocity pulses in the SN and SP directions, respectively.

Near-fault ground motions are not properly represented in modern codes and their effects have not been properly incorporated into current ground motion prediction equations or probabilistic seismic hazard analysis methods, though efforts in this direction are ongoing (e.g., Shahi and Baker, 2011). The large pulse inherent in these motions can potentially subject structures to one or two cycles of severe inelastic deformation and result in a large amount of damage, especially in long period structures such as base-isolated buildings, tall buildings and long-span bridges. It is only after the 1994 Northridge earthquake that the severe implications of near-fault ground motions on the performance of structures and

the importance of incorporating their effects into the design process was recognized (Mavroeidis and Papageorgiou, 2003). Unfortunately, near-fault records are scarce, and thus a large effort has been recently focused on trying to understand, model and simulate these ground motions and their effects on the response of structures.

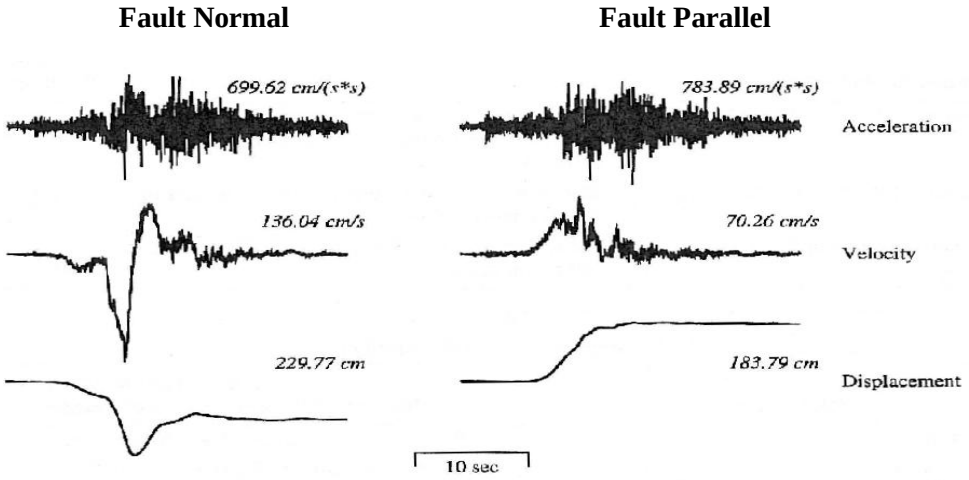

Figure 2.1: FN and FP acceleration, velocity and displacement time histories at the Lucerne near-fault forward directivity station during the 1992 Landers earthquake (from Somerville et al., 1997)

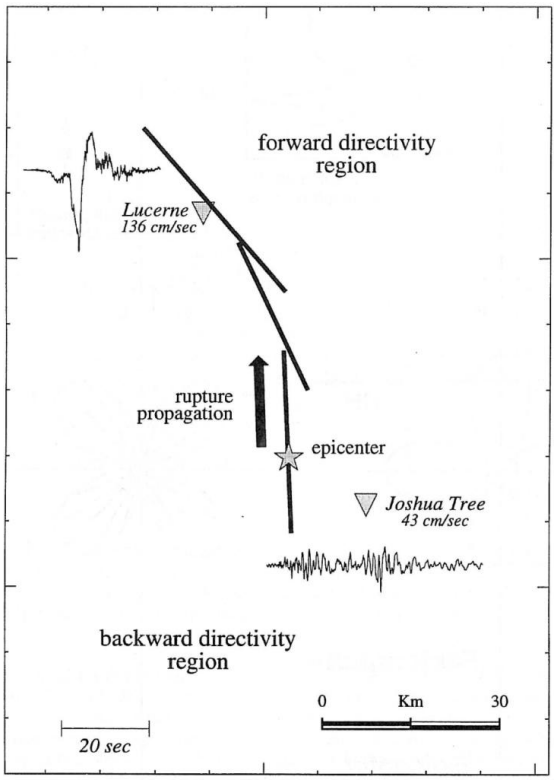

Figure 2.2: SN velocity time histories at the near-fault Lucerne (forward directivity) and Joshua Tree (backward directivity) stations (from Somerville et al., 1997)

Special attention needs to be given to the design of bridges in the near-fault region. In addition to the large velocity pulse in the FN direction and the large static displacements in the FP direction, near-fault bridges with multiple supports are often subjected to large dynamic differential motions. These may arise from wave passage and incoherence effects, as well as from spatial variations in directivity conditions and from permanent differential displacements, especially when the fault rupture reaches the surface (Somerville, 2002).

In this chapter, we present a brief overview of the state-of-the-art in understanding, predicting and modeling near-fault ground motions. A thorough understanding of the underlying phenomena and principles is needed for the developments in the subsequent chapters of this report.

2.2 PHYSICS OF NEAR-FAULT GROUND MOTIONS

For sites located sufficiently far from the earthquake source, the size of the rupture is small compared to the distance between the fault and the site. The fault appears as a point source and the radiation effectively comes from a single point, thus the distance and radiation pattern are well defined. Moreover, the arrival times of the P and S waves are quite clear. This is not the case in the near-field region, where, due to the finite nature of the fault, there no longer is a unique definition of distance or radiation angle. As the rupture propagates along the fault, the radiation angle between the fault rupture and the site continuously changes (Archuleta and Hartzell, 1981; Somerville et al. 1997). As mentioned earlier, two main effects are characteristic of near-fault ground motions and cause them to be different from far-field ground motions: the directivity effect and the fling step. The forward directivity effect results in a large amplitude, long period two-sided pulse in the velocity time history of the FN component of the ground motion. The fling step results in a one-sided velocity pulse and permanent displacement at the end of the ground motion record in the FP direction (along the fault plane, in the direction of the slip). These effects, which are currently not adequately taken into consideration in the design process, are described in greater detail in this section. They have been observed in a variety of tectonic environments but have been mostly idealized for strike-slip and dip-slip faults. Other effects that are typically ignored and that may also influence ground motions are also discussed. Finally, parameters that have been found adequate to describe directivity effects are introduced.

2.2.1 Directivity effect

An earthquake occurs when a rupture and slip suddenly occur along a fault, resulting in the release of the accumulated strain energy in the form of seismic waves. The rupture starts at the hypocenter and propagates in two dimensions along the fault plane. If the rupture propagates towards a site, the site is

said to be located in the forward directivity region. Such a site usually experiences a short duration, large amplitude pulse at the beginning of the velocity time history, in the direction perpendicular to the fault plane or the FN direction. If the rupture propagates away from the site, the site is said to be in the backward directivity region and records a small amplitude, long duration ground motion in the FN direction (Somerville et al., 1997). The polarity of the pulse depends on the location of the site relative to the epicenter (Archuleta and Hartzell, 1981).

Two conditions must be met for the forward directivity effect to be observed at a site. First, the rupture front should propagate towards the site and at a velocity almost equal to the shear wave velocity of the ground, such that all the seismic energy arrives at the site in a single, short duration pulse due to the constructive interference of the radiated waves (primarily shear or S-waves) from the fault rupture between the hypocenter and the site. The S-wave radiation pattern is typically split into SH waves and SV waves, defined below. Second, the direction of wave propagation between the hypocenter and the site should be aligned with the direction of the slip on the fault, which corresponds to the maximum of the SH radiation pattern (waves travelling in the tangential direction, normal to the fault plane), such that large amplitudes are obtained in the FN direction. In other words, the three directions (of rupture, of slip, and of wave propagation between the hypocenter and the site) should be aligned together to maximize the directivity effect (Somerville and Graves, 1993; Somerville et al., 1997). Note that when the fault plane is not vertical, the FN direction does not coincide with a horizontal direction. Only when the fault plane is vertical or near vertical does the FN direction coincide with the horizontal strike normal (SN) direction. Figure 2.3 illustrates the effect of rupture propagation and wave propagation on the waveforms in the forward and backward directivity region.

The conditions for the forward directivity effect are easily met in strike-slip faulting: the maximum in the SH radiation pattern is oriented in the direction along the strike, which is also the slip direction, as can be seen in Figure 2.4. Furthermore, the rupture propagates along the strike either unilaterally or bilaterally, resulting in constructive interference of the SH waves (tangential motion, normal to the direction of wave propagation) in one or both directions, respectively. All locations close to the fault rupture and towards which the rupture propagates will then have large dynamic motions in the FN (tangential) direction, except for locations close to the epicenter. The latter are too close to the initial rupture point for constructive interference to be significant, and the rupture mainly propagates away from them, resulting in backward directivity effects. As also illustrated in Figure 2.4, the SV radiation pattern (radial motion, in the direction of wave propagation) has a minimum in the direction along the strike, so that the dynamic motion in the FP (radial) direction will be small, even though there may still be a large static FP displacement (Somerville and Graves, 1993; Somerville et al., 1997). For strike-slip faults, the

FN direction usually corresponds with the SN direction because the fault is typically near vertical, and the FP direction corresponds with the SP direction (Mavroeidis and Papageorgiou, 2002).

Directivity conditions can also be met in dip-slip faulting, for both normal and reverse faults, but directivity effects occur less often and are less severe. This is because the maximum of the SH radiation pattern in the slip direction (along the dip of the fault) coincides with the rupture direction only in the updip direction. Therefore, for a site to experience the forward directivity effect, it must be located directly updip from the hypocenter, around the surface exposure of the fault (or its updip projection if it is a buried fault). Stations located along the strike don't experience directivity effects because the horizontal rupture direction coincides with a minimum in the total S radiation pattern. Moreover, even a favorably located station will generally have a less pronounced directivity effect than in the strike-slip case, because the length of the rupture towards the station is limited by the downdip depth of the fault (e.g., about 25km for an 18km deep hypocenter and a dip angle of 45°), while for strike-slip earthquakes the limit is the rupture length along the strike, which can reach hundreds of km (Somerville and Graves, 1993; Somerville et al., 1997). Dip-slip faults are usually far from vertical, in which case the FN direction has components in both the horizontal SN direction and the vertical direction. The larger the dip angle, the better is the FN direction approximated by the SN direction. The smaller the dip angle, the better is the FN direction approximated by the vertical direction of the ground motion (Mavroeidis and Papageorgiou, 2002).

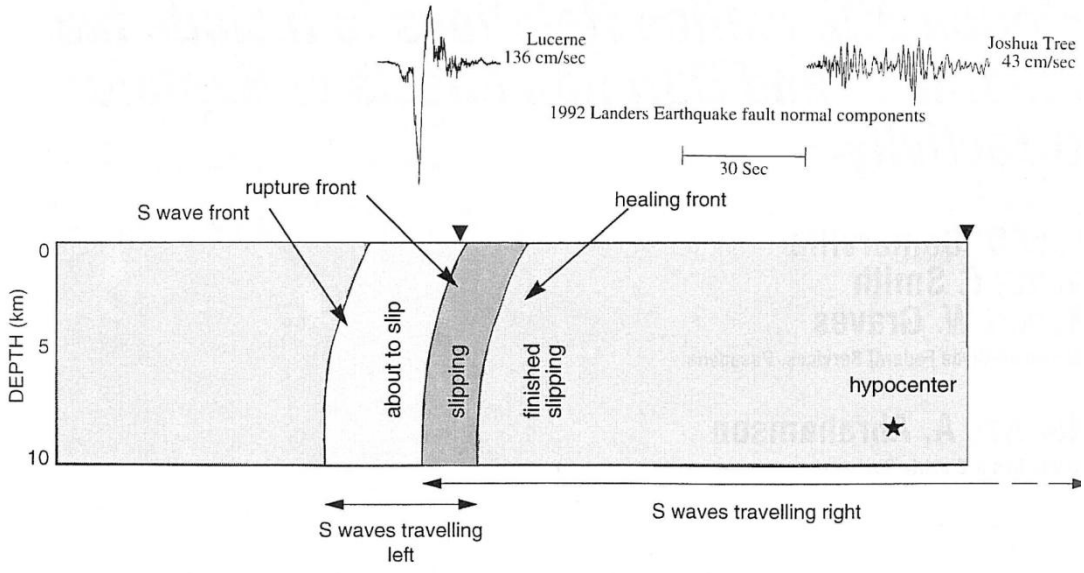

Figure 2.3: Rupture propagation and directivity effects (from Somerville et al., 1997)

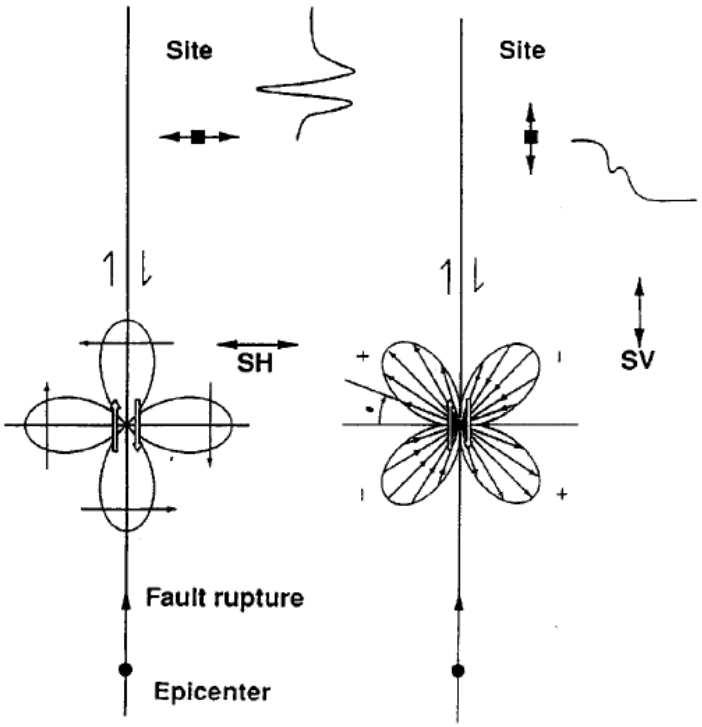

Figure 2.4: SH and SV radiation patterns for a vertical strike-slip fault (from Somerville et al., 1997)

2.2.2 Fling step

The fling step is another effect that results in a pulse in the velocity time history, but while the directivity pulse is two-sided, the fling step pulse is one-sided. When an earthquake occurs along a fault, the two sides of the rupturing fault move relative to each other, resulting in the permanent tectonic deformation of the ground. This is known as the fling step. If the fault has a surface rupture, then the displacements across the fault will be discontinuous, thus subjecting a bridge crossing the fault to large differential displacements. Static deformations occur even in the absence of surface faulting, as illustrated in Figure 2.5 for a strike-slip fault; they are maximum at some distance away from the fault and they gradually decrease as one moves away from either side of the fault (Somerville, 2002). This static ground displacement is typically observed in the FP direction along the slip direction; it appears as a discrete step in the displacement time history and as a one-sided pulse in the velocity time history. For strike-slip faults, the fling step is visible in the SP direction and for dip-slip faults it appears in the SN and vertical directions (Mavroeidis and Papageorgiou, 2002; Bray and Rodriguez-Marek, 2004). Thus, in the case of a dip-slip fault, directivity and fling both appear in the SN direction; whereas they appear separately on orthogonal horizontal SN and SP directions in the case of a strike-slip fault (Mavroeidis and Papageorgiou, 2002). It has been observed that the fling-step pulse usually has a shorter period than the

directivity pulse, but occurs at about the same time. The two effects, thus, can be be modeled separately and then treated as coincident events (Bray and Rodriguez-Marek, 2004; Somerville, 2002). It should be noted that standard filtering procedures applied to raw ground motion records for baseline correction remove the static displacement. Thus, special processing should be used to preserve this information (Mavroeidis and Papageorgiou, 2002).

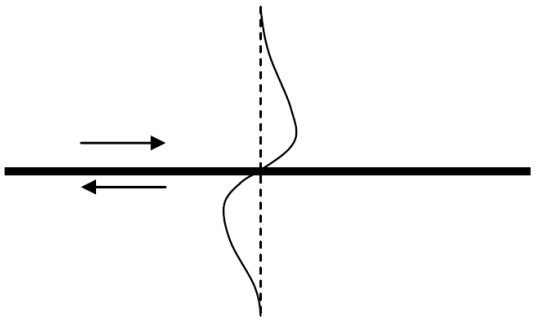

Figure 2.5: FP displacements for a strike-slip fault with buried rupture (plan view)

2.2.3 Other effects

Several effects besides the rupture directivity and fling step are present in earthquake ground motions, some of which may also produce large, long period pulses (Mavroeidis and Papageorgiou, 2002; Somerville, 2000). These include hanging wall effects (also near fault), crustal waveguide effects (path effects), and basin effects (site effects). Their inclusion in ground motion prediction equations is expected to result in a reduction of model uncertainty, as they are currently treated as randomness (Somerville, 2000).

Hanging-wall effects arise from geometrical conditions in the near-fault region. For two sites located at the same closest distance to a dip-slip fault, but with one being on the hanging wall and the other being on the footwall, the former site will experience ground motions with larger amplitudes. This is because stations on the hanging wall are closer to a greater surface of the fault rupture. These differences in amplitudes are most pronounced at short periods. Therefore, while directivity effects result in spatial variation of near-fault ground motions at longer periods, hanging-wall effects result in spatial variations at shorter periods (Mavroeidis and Papageorgiou, 2002; Somerville, 2000; Dreger et al., 2011). Mavroeidis and Papageorgiou (2002) also mention other special effects resulting in large ground motions in the near-fault region. Special geometric conditions, such as a circular barrier on the fault plane, can result in the coherent addition of seismic waves and thus in extreme accelerations. Also, supershear rupture velocity, which is an unusual but possible situation, results in large velocity pulses in the SP direction. This effect

has been modeled by Mendez and Luco (1988) as a steady-state dislocation embedded in a layered half-space.

Somerville (2000) discusses crustal waveguide effects, which highlight other differences between near-field and far-field ground motions. At close distances, say within 50km of the fault, the largest ground motion amplitudes are usually caused by direct body waves travelling upward from the source to the site. As the distance increases, these direct waves become weaker and the largest amplitudes are caused by reflected and refracted waves. These waves initially travel downward from the source until they reach interfaces below the source, where they undergo critical reflections. They arrive at the surface at distances between 50km and 100km and result in a reduction of the rate of attenuation. At this distance range, amplitudes are actually not large by themselves, but may produce damage if amplified by local soils.

Somerville (1993, 2000) also discusses basin effects, which are not accounted for in current ground motion prediction equations. Basin effects can be of two type: basin-edge effects and focusing effects. Like directivity effects, they may result in large, long period ground motions that can have damaging effects. Such effects were observed, for example, during the 1971 San Fernando and the 1989 Loma Prieta earthquakes. Compared to rock sites, much more complex waveforms were recorded at basin sites, with relatively weak direct S-waves and peak ground velocities controlled by surface waves generated within the basin (Somerville and Graves, 1993). The response of sedimentary basins, composed of alluvial deposits and sedimentary rocks with relatively small shear-wave velocity, is usually computed using 1D models in which the site is represented by horizontal layers and is characterized by the shear wave velocity in the top 30m of soil (V_{s30}). In such a representation, waves can resonate but they cannot be trapped within a layer. Thus, amplifications due to impedance contrast are reproduced, but not the trapping and focusing of seismic waves, which usually results in large amplitude surface waves and long durations of shaking. When body waves enter a basin (even a small and shallow basin) through its thickening edge, internal reflection of energy can occur and the waves can become trapped as surface waves in the basin and propagate across the basin until they reach the thinning edge, from where they escape as body waves. The amplitudes can become quite large due to constructive interference of direct waves with laterally propagating surface waves. This is known as the basin-edge effect. Moreover, at periods longer than 1s, seismic waves have wavelengths much longer than 30m and their amplitudes are controlled by deeper geologic (sedimentary and/or topographic) structures, which might not be horizontally layered and which may focus energy in spatially restricted areas on the surface, resulting in localized zones of high ground motion levels. These are known as focusing effects. To represent these basin effects, 2D or 3D basin models are needed (Somerville and Graves, 1993; Somerville, 2000).

2.2.4 Geometrical directivity parameters

Ground motion levels are generally modeled and predicted in terms of variables that describe the earthquake and site characteristics, specifically the source, the path and the site. The source is represented by the earthquake moment magnitude, denoted M_w, and by the type of faulting, which is represented here by the indicator variable F ($F = 0$ denotes a strike-slip fault, $F = 1$ denotes a dip-slip fault, etc.); the path is represented by the closest distance R between the site and the fault rupture; and the local site conditions are usually characterized by the shear-wave velocity in the top 30 meters, denoted V_{s30} (Somerville, 2000). Recent NGA ground motion prediction equations include additional terms, such as the depths to shear-wave velocities of 1.0km/s and 2.5km/s, denoted $Z_{1.0}$ and $Z_{2.5}$ respectively, and a hanging-wall factor F_{HW} (Abrahamson et al., 2008). In the near-fault region, the ground motions are more complex and more variable. As described earlier, they depend on the spatial distribution of the slip along the fault rupture, on the spatially varying radiation pattern between the fault rupture and the site, on the velocity of the rupture, and on the direction of propagation of the rupture relative to the site (Archuleta and Hartzell, 1981). Consequently, additional parameters are needed to represent near-fault effects. For the reasons presented in earlier sections, the presence and characteristics of a forward directivity pulse mainly depend on the geometric configuration of the site relative to the rupture surface and the direction of propagation of the rupture. Thus, various geometrical parameters have been proposed to model the forward directivity effect.

Somerville et al. (1997) used two parameters to characterize the forward directivity effect: (1) the fraction of the fault rupturing between the hypocenter and the site in the direction of slip, and (2) the angle between the rupture plane and the direction between the hypocenter and the site, which represents the path of the travelling waves. For strike-slip faulting, they define X as the ratio of the length of the fault rupturing between the epicenter and the site to that of the total rupture length. Similarly, for dip-slip faulting, they define Y as the ratio of the width of the fault rupturing between the hypocenter and the site to that of the total width of the rupture plane. Thus, letting s and d be the length and width of the rupture between the hypocenter and the site, respectively, and L and W be the total length and width of the rupture, respectively, we have $X = s/L$ and $Y = d/W$. They define θ as the angle in the horizontal plane between the fault rupture plane and the direction between the epicenter and the site for strike-slip earthquakes. Similarly, they define ϕ as the angle in a vertical plane between the fault rupture plane and the direction between the hypocenter and the site for dip-slip earthquakes. In reality, for near-fault sites, the radiation angle between the fault rupture and the site varies as the rupture propagates along the fault, because the dimension of the fault is large relative to the distance between the source and the site. For simplicity, however, only the radiation angle between the hypocenter and the site has been used in

directivity models. All the geometric parameters described above are illustrated in Figure 2.6, where it can be seen that X and θ are measured in the horizontal plane, while Y and ϕ are measured in the vertical plane oriented normal to the fault strike. Somerville et al. (1997) explain that they expect the ground motion amplitude to increase and the duration to decrease when the geometric conditions increasingly favor directivity effects, i.e., as the angle θ or ϕ decreases and the fraction X or Y of the rupture increases. They, thus, expect an inverse relationship between the amplitude and duration. Somerville et al. (1997) investigated simple functional forms of the directivity parameters for use in their model. They ended up selecting $Xcos\theta$ and $Ycos\phi$ for strike-slip and dip-slip earthquakes, respectively, because the cosine function gives a smooth decay when the angle increases.

Iervolino and Cornell (2008) and later Abrahamson and Watson-Lamprey (2010) and Shahi and Baker (2011) suggested using the length and width of the portion of the rupture that propagates towards the site, s and d, rather than the fractions X and Y to characterize strike-slip and dip-slip near-fault ground motions, respectively. This modification makes sense, since the constructive interference should be correlated with the length or width of the rupture between the source and the site, rather than the fraction of the rupture. In particular, a large s or d is likely to result in a directivity pulse, independently of the total length of the rupture. Note that the rupture dimensions are typically related to the earthquake magnitude (Iervolino and Cornell, 2008). In addition to the geometric parameters, Archuleta and Hartzell (1981) show that the rupture velocity also affects rupture directivity. This is confirmed by Dreger et al. (2006). However, to our knowledge, this effect has not been included in any existing prediction model. For oblique-slip earthquakes, which have components of both strike-slip and dip-slip faulting, typically the parameters for dip-slip faults have been used, though this is an incomplete representation.

It is important to note that the closest distance between the site and the fault rupture is not independent of the other geometric parameters. For strike-slip faults, R, s and θ are related by $R = s\tan\theta$ $R = s \cdot \tan\theta$, if the rupture can be represented by a straight line and if the site is located alongside the rupture. If the rupture cannot be represented by a straight line, which is sometimes the case, or if the site is not located alongside the fault rupture, this relationship does not hold. Taking the example of a vertical strike-slip fault with surface rupture, such as the one depicted in Figure 2.7, it is clear that $R_1 = s_1 \tan\theta_1$ but that $R_2 > s_2 \tan\theta_2$. Similarly, for dip-slip faults, R, d and ϕ are related by $R = d\tan\phi$, if the rupture width can be represented by a straight line and the site is located alongside the rupture width. Otherwise, this relationship does not hold.

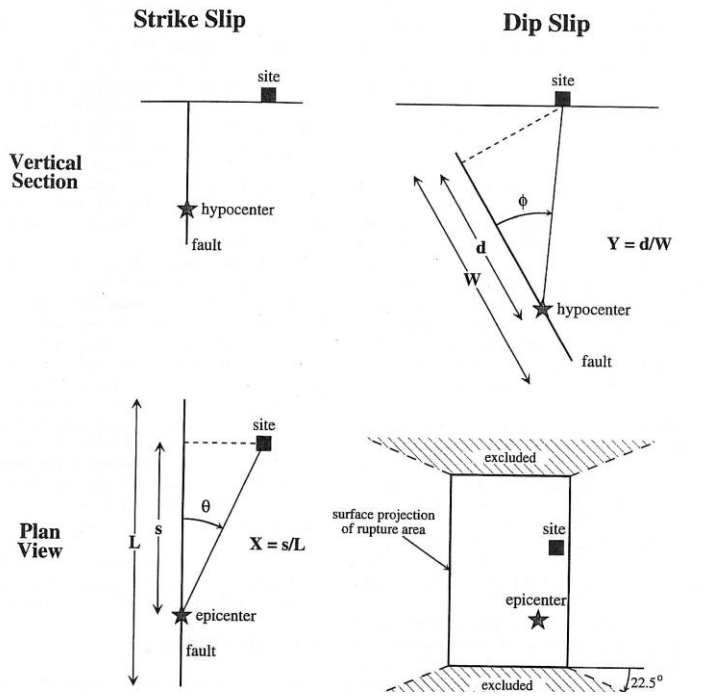

Figure 2.6: Directivity parameters (from Somerville et al. 1997)

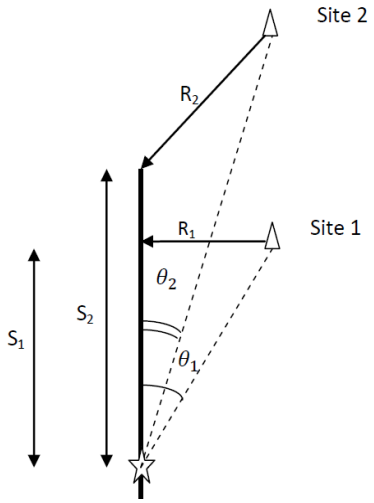

Figure 2.7: Geometric relationship between the directivity parameters for a strike-slip fault (plan view)

2.3 MODELS OF THE DIRECTIVITY EFFECT

In this section, we discuss the models that have been proposed and used to account for the near-fault rupture directivity effect. The fling step is modeled separately, but the two effects should be ultimately combined in developing ground motions. The rupture directivity models are generally of two types: (1)

those that account for the directivity effect by modifying the currently used response spectra, and (2) those that attempt to directly model the near-fault ground motion time histories. Note that most authors use the terms FN and FP to actually signify SN and SP. In this report, we make a distinction between the two notations: FN and FP are used when discussing the physics of near-fault ground motions, as the directions in which the directivity effect and fling step occur, respectively, while SN and SP are the horizontal directions for which the near-fault models are typically formulated.

2.3.1 Spectral methods

As already described, near-fault ground motions tend to exhibit a large pulse in the velocity time history in the FN direction, when forward directivity conditions are met. This is reflected by a peak in the corresponding response spectrum near the period of the pulse, and by a large ratio of the SN to SP spectral accelerations at intermediate to long periods (Somerville and Graves, 1993). These characteristics do not appear in far-field ground motions. Methods to modify response spectra developed for far-field ground motions to account for the directivity effect have been proposed by various authors. Broadband directivity models were initially formulated, before narrowband models were found to be more accurate. These are described in the following sections.

2.3.1.1 Broadband directivity model

A broadband directivity model was first developed by Somerville et al. (1997). It was later modified by Abrahamson (2000) to incorporate saturation effects and tapering for small magnitudes and large distances. Both models amplify spectral amplitudes of the SN component of the ground motion at all periods in order to account for the forward directivity effect. The amplification factor is a function of the geometrical parameters of the site relative to the fault; specifically, it is equal to $X\cos\theta$ for strike-slip faults and $Y\cos\phi$ for dip-slip faults (Somerville, 2003). Somerville et al. (2003) also developed modifications to the average duration predicted by ground motion prediction models as a function of the same geometrical parameters, and they found negative correlation between the amplitude and duration (Somerville et al. 1997). This is consistent with the finding that the forward directivity effect favors the constructive interference of waves into a pulse motion with a large amplitude and a short duration.

2.3.1.2 Narrowband directivity model

As we have seen, near-fault ground motions with forward directivity typically contain a long period pulse in the FN velocity time history, which is also observed in the SN horizontal component. This pulse is narrowband and its period tends to increase with the earthquake magnitude. For this reason, modification of the response spectrum for the forward directivity effect should scale with the earthquake magnitude

instead of being uniform at all periods, such that the peak in the response spectrum occurs at a period that increases with the magnitude. This feature has been observed in response spectra of recorded near-fault ground motions. Because of this phenomenon, it is possible that spectral amplitudes from a small earthquake at a near-fault site exceed spectral amplitudes from a larger earthquake in the intermediate period range (Somerville, 2002). This observation led to the development of narrowband directivity models, which amplify the response spectrum only in a narrowband region around the period of the velocity pulse.

Somerville (2003) suggested developing the acceleration response spectrum of the SN component of a ground motion with a forward directivity pulse of period T_p by using a conventional response spectrum and scaling it by a cosine shaped function that is centered at $0.75T_p$, has a peak amplitude of 2 and a width of $1.5T_p$. Shahi and Baker (2011) computed the amplification factor A_f in the spectral accelerations of recorded near-fault ground motions containing directivity pulses. On average, the amplification is bell-shaped and centered near the pulse period T_p, as can be observed inFigure 2.8. They fitted the following function to the mean of the logarithm of the amplification factor:

$$\begin{aligned} \mu_{lnA_f} &= 1.131 \exp\left\{-3.11\left[ln\left(\frac{T}{T_p}\right)+0.127\right]^2+0.058\right\} \qquad \text{if } T \le 0.88T_p \\ &= 0.896 \exp\left\{-2.11\left[ln\left(\frac{T}{T_p}\right)+0.127\right]^2+0.255\right\} \qquad \text{if } T > 0.88T_p \end{aligned} \tag{2.1}$$

The above function takes a maximum value of 1.19 at $T = 0.88T_p$, which corresponds to a peak median value of 3.29 of the amplification factor A_f.

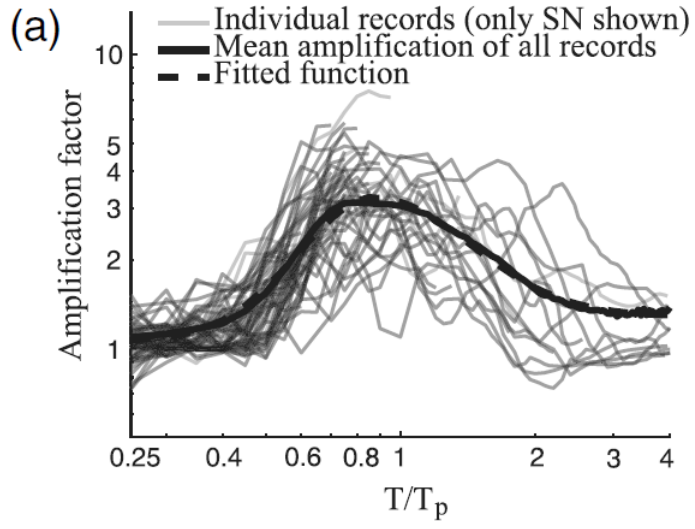

Figure 2.8: Narrowband spectral amplification factor for SN component of pulse-like ground motions (from Shahi and Baker, 2011)

2.3.2 Time history methods

Response spectra are usually appropriate to characterize the demands of far-field ground motions, which tend to be long duration processes with relatively uniform distribution of energy over the duration of strong shaking (Bray and Rodriguez-Marek, 2004). However, they are not adequate to characterize the demands resulting from shorter duration, impulsive near-fault ground motions (Somerville, 1998; Somerville, 2000). One reason is that they do not adequately represent the demand of the velocity pulse for a high rate of energy absorption, and another is that most near-fault pulses drive structures into the inelastic range, while response spectra assume linear elastic behavior (Somerville, 2002). For such cases, nonlinear dynamic analysis is required, thus the need to represent near-fault ground motions by suites of time histories, or at least by time domain parameters, such as the pulse amplitude, period and number of half-cycles, to supplement the response spectrum (Somerville, 1998).

Time histories to be used in the design and analysis of near-fault structures should be carefully selected. It is not sufficient to select time histories that have response spectra matching a design spectrum, because spectral matching cannot create a pulse in a record that does not initially contain a pulse, even if the design spectrum includes the contribution of a directivity pulse (Somerville et al., 1997; Somerville, 2000; Mavroeidis and Papageorgiou, 2002). Since near-fault recordings that contain directivity pulses are relatively scarce, there exists a need to model and simulate near-fault ground motions that include the rupture directivity effect. Below, we describe existing work on this topic. In the subsequent chapters of this study, we develop new models and simulation methods to generate synthetic near-fault ground motions containing the directivity pulse, which possess the statistical characteristics of recorded near-fault ground motions.

2.3.2.1 Velocity pulse models

Alavi and Krawinkler (2000) observed that the response of structures to near-fault ground motions had similarities with the response of structures to pulse-type motions. On this basis, they suggested that pulselike near-fault ground motions (or, more appropriately, the velocity pulses they contain) can be represented by simple time domain waveforms, formulated in terms of a few physically meaningful parameters, the most important of which are the pulse amplitude, the pulse period and the number of half-cycles of the pulse. However, there is no unique definition of the pulse amplitude and period. Mavroeidis and Papageorgiou (2002) and Bray and Rodriguez-Marek (2004) review several definitions proposed in the literature, which involve varying levels of subjectivity. Alavi and Krawinkler (2000) defined the equivalent pulse amplitude by minimizing the difference between the maximum story ductility demands estimated for the pulse-type record and the equivalent pulse; they observed that the equivalent pulse

amplitude lies within 20% of the peak ground velocity (PGV) in most cases. Mavroeidis and Papageorgiou (2003), on the other hand, determined the pulse amplitude such that both the pulse waveform and its peak pseudo-spectral velocity closely match the corresponding quantities of the actual record. As for the pulse period, Alavi and Krawinkler (2000) defined it as the period at which the pseudo-velocity response spectrum has its peak value. Mavroeidis and Papageorgiou (2003) determined the pulse period by matching the periods at which the pseudo-velocity spectra of the pulse waveform and of the recorded ground motion assume their peak values. Finally, Bray and Rodriguez-Marek (2004) defined the directivity pulse period as the period of the pulse having the largest amplitude in the recorded motion, where the pulse period is defined as twice the interval between two successive zero-level crossing times.

2.3.2.1.1 Simple pulse models

Somerville (1998) developed an improved parametrization of pulselike near-fault ground motions by including time domain parameters to complement the response spectrum representation. Parameters of the preliminary model are the amplitude and duration of the largest velocity cycle, which consists of a peak, a trough and three zero crossings. With this defintion, the pulse amplitude equals the PGV and the pulse period equals the duration of the full velocity cycle. Using recorded data, these parameters were regressed against the earthquake magnitude, M_w, and the closest distance, R. The pulse period was found to be related to the magnitude through

$$\log_{10} T_p = -2.5 + 0.425 M_w \tag{2.2}$$

With the constraint of self-similarity between the pulse period and magnitude, i.e., the constraint that the pulse period and magnitude grow in proportion with the fault dimensions, Somerville (1998) obtained

$$\log_{10} T_p = -3 + 0.5 M_w \tag{2.3}$$

Finally, assuming a linear relation between the PGV and R, which is not realistic at close distances, Somerville (1998) obtained

$$\log_{10} PGV = -1.0 + 0.5 M_w - 0.5 \log_{10} R \tag{2.4}$$

Alavi and Krawinkler (2000) investigated three idealized pulse shapes, denoted P1, P2 and P3 and shown in Figure 2.9, which are defined in terms of two parameters: the pulse period T_p and pulse amplitude $v_{g,max}$. They then related a set of near-fault records to these parameters. They found that these idealized pulse shapes are capable of representing near-fault ground motions within some limitations. Pulse P2 was capable of representing many records. They regressed the parameters of the equivalent idealized pulses against the earthquake magnitude and closest distance to the fault rupture, arriving at the following predictive relations:

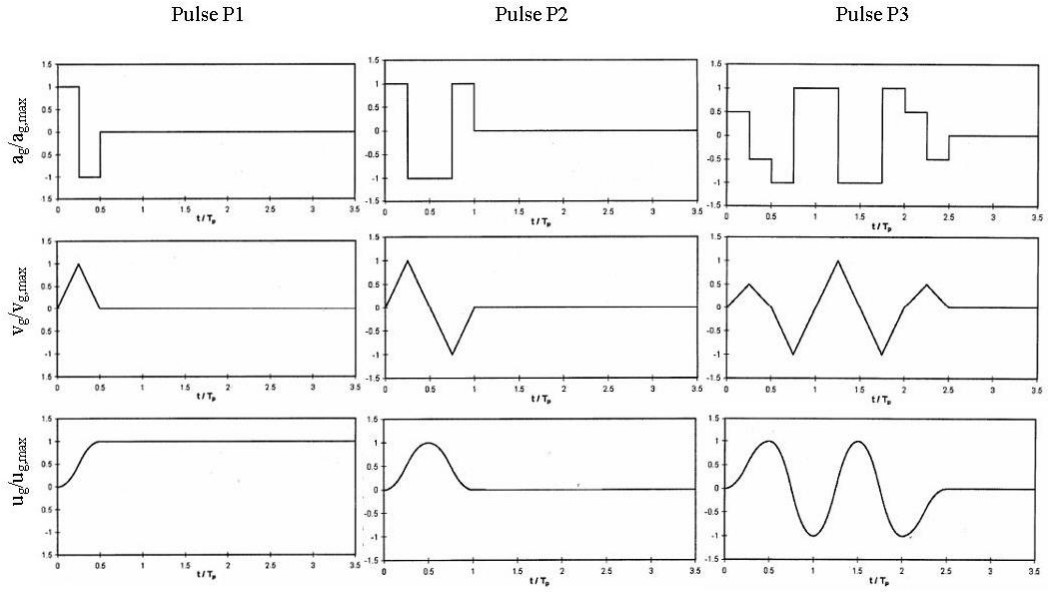

Figure 2.9: Acceleration, velocity and displacement time histories of idealized pulses P1, P2 and P3 (from Alavi and Krawinkler, 2000)

$$\log_{10} T_p = -1.76 + 0.31M_w \tag{2.5}$$

$$\log_{10} v_{g,max} = -2.22 + 0.69M_w - 0.58\log_{10} R \tag{2.6}$$

Alavi and Krawinkler (2000) warn that caution should be exercised in interpreting these results, because a small number of records was used to derive them, and they came from events with different faulting mechanisms and geologic environments, resulting in large scatters.

Somerville (2003) used simple triangular velocity pulses to incorporate the effect of the directivity pulse on response spectra. The pulse period was obtained from the database of recorded near-fault SN pulselike velocity time histories as the period of the largest cycle of motion. He assumed the period to be independent of distance from the fault and developed separate relations for rock and soil sites. For rock sites, assuming self-similarity, he obtained the relation

$$\log_{10} T_p = -3.17 + 0.5M_w \tag{2.7}$$

The relation for soil sites was allowed to depart from self-similarity in order to accommodate non-linear effects, since the soil layer tends to increase both the peak velocity and the period by amounts that depend on the level of the input ground motion and on the thickness and physical properties of the soil layer. The regression for soil sites resulted in the relation

$$\log_{10} T_p = -2.02 + 0.346M_w \tag{2.8}$$

Bray and Rodriguez-Marek (2004) chose to represent both directivity and fling velocity pulses by half-sine waves. To fully define the bi-directional motion, the pulses are represented in terms of the number, N, of equivalent half-cycles in each direction, the period, T_{vi}, and amplitude, A_i, of each half cycle, and the lag time, t_{off}, between the beginnings of the SN and SP pulses. However, for the purpose of developing a model of the SN forward directivity pulse, they chose to limit the model parameters to the PGV, the approximate period of the dominant pulse, T_p, and the number N of significant half-cycles, which are defined as half-cycles with amplitude equal to or greater than $0.5PGV$. In developing predictive equations for the parameters of near-fault pulses, Bray and Rodriguez-Marek (2004) noted that simplified functional forms can be used because distances are relatively short, eliminating the need for a complex model form that can account for a wide range of distances. They noted that the PGV of the SN component of pulselike motions varies significantly with M_w and R, that it is larger for soil than for rock sites, and that it has a nearly zero slope at close distances and linearly decreases with the logarithm of distance at larger distances. Their recommended relations are

$$\begin{aligned} \ln PGV &= 4.51 + 0.34M_w - 0.57\ln(R^2 + 7^2) \quad \text{for all sites} \\ &= 4.46 + 0.34M_w - 0.58\ln(R^2 + 7^2) \quad \text{for rock sites} \\ &= 4.58 + 0.34M_w - 0.58\ln(R^2 + 7^2) \quad \text{for soil sites} \end{aligned} \tag{2.9}$$

where R is measured in kilometers. As with previous investigators, they used a linear dependence of $\ln T_p$ on M_w, but they constrained the predicted pulse periods to be equal on rock and soil sites at $M_w = 7.6$ in order to avoid larger periods on rock than on soil for $7 < M_w$. The resulting relations are

$$\begin{aligned} \ln T_v &= -6.37 + 1.03M_w \quad \text{for all sites} \\ &= -8.60 + 1.32M_w \quad \text{for rock sites} \\ &= -5.60 + 0.93M_w \quad \text{for soil sites} \end{aligned} \tag{2.10}$$

Thus, for small magnitudes, longer periods are predicted at soil sites than at rock sites, but the differences decrease and disappear for larger magnitudes.

2.3.2.1.2 The Menun and Fu model

Menun and Fu (2002) first proposed a model of the velocity pulse time history in terms of five parameters: amplitude V_p of the pulse, period T_p of the pulse, the start time t_0 of the pulse, and shape parameters n_1 and n_2. The analytical expression of their model is

$$\begin{aligned} v(t) &= V_p \exp\left[-n_1\left(\frac{3}{4}T_p - t + t_0\right)\right]\sin\left[\frac{2\pi}{T_p}(t - t_0)\right] \qquad t_0 < t \le t_0 + \frac{3}{4}T_p \\ &= V_p \exp\left[-n_2\left(t - t_0 - \frac{3}{4}T_p\right)\right]\sin\left[\frac{2\pi}{T_p}(t - t_0)\right] \qquad t_0 + \frac{3}{4}T_p < t \le t_0 + 2T_p \\ &= 0 \qquad \text{elsewhere} \end{aligned} \tag{2.11}$$

Figure 2.10 shows plots of the above pulse model for several selections of the model parameters.

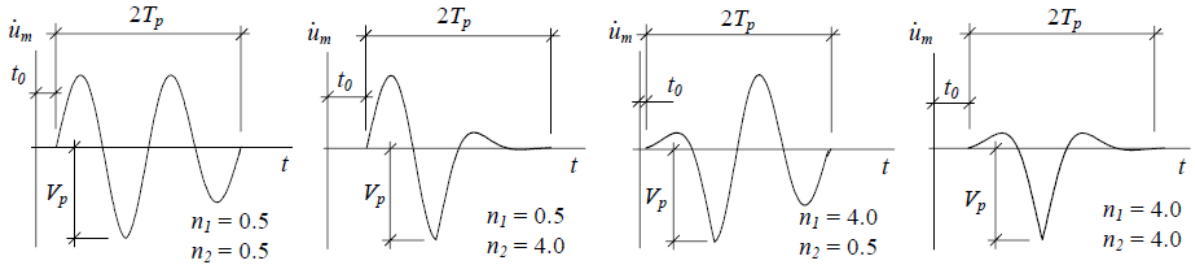

Figure 2.10: Sample velocity pulses generated by the Menun and Fu model (from Menun and Fu, 2002)

Fu and Menun (2004) later proposed a different formulation of the velocity pulse, based on idealizing the velocity pulses appearing in synthetic time histories generated according to the Haskell seismological source model (Aki and Richards 1980) with forward directivity site conditions. This formulation is in terms of four parameters: amplitude V_p of the pulse, period T_p of the pulse, the start time t_0, and a shape parameter α. The model is defined by

$$v(t) = V_p \exp\{1 - \alpha(t - t_p) - \exp[-\alpha(t - t_p)]\} \sin\left[\frac{2\pi}{T_p}(t - t_0)\right] \quad t_0 < t \le t_0 + 2T_p$$
$$= 0 \quad \text{elsewhere} \tag{2.12}$$

where $t_p = t_0 + 0.75T_p$ is the time at which the peak velocity occurs. Fu and Menun (2004) developed predictive relations for V_p, T_p and α by using a sample of recorded motions. They first developed a predictive relation for PGV in terms of M_w and R, and found V_p to be strongly correlated with PGV so that approximately $V_p = 0.8PGV$. The resulting predictive equations are

$$\log_{10} PGV = 0.49 + 0.21M_w - 0.16 \log_{10} R \tag{2.13}$$

$$\log_{10} V_p = 0.39 + 0.21M_w - 0.16 \log_{10} R \tag{2.14}$$

$$\log_{10} T_p = -3.38 + 0.54M_w \text{ (for both rock and soil)} \tag{2.15}$$

They noted that the relation for T_p is different for rock and soil conditions at small magnitudes, but the difference disappears as M_w increases. Finally, for parameter α, which influences the waveform of the velocity pulse in time domain and the width and location of the spectral content in the frequency domain, they noted that as α increases in absolute value, the length of the signal in time domain increases, but the bandwidth in frequency content decreases. On this basis, they proposed the predictive relation

$$|\alpha| = \frac{2.5}{T_p} \tag{2.16}$$

2.3.2.1.3 The Mavroeidis and Papageorgiou pulse model

Mavroeidis and Papageorgiou (2003) warned that the use of simplified waveforms (square, triangular or sinusoidal) may be misleading. Instead, they proposed a velocity pulse model in terms of five parameters: amplitude V_p of the pulse, period T_p of the pulse, parameter γ describing the oscillatory character of the pulse, the phase angle ν of the pulse, and the time t_0 at which the pulse envelope assumes it peak value. The model consists of the product of a harmonic function and a bell-shaped envelope function (a shifted haversed sine function):

$$\begin{aligned} v(t) &= \frac{1}{2}V_p\left\{1+\cos\left[\frac{2\pi}{\gamma}\left(\frac{t-t_0}{T_p}\right)\right]\right\}\cos\left[2\pi\left(\frac{t-t_0}{T_p}\right)+\nu\right] \quad t_0-\frac{\gamma}{2}T_p < t \le t_0+\frac{\gamma}{2}T_p \\ &= 0 \qquad\qquad\qquad\qquad\qquad\qquad\qquad\qquad\qquad\qquad\qquad\qquad \text{elsewhere} \end{aligned} \tag{2.17}$$

The advantages of this model are that it has a relatively simple mathematical expression, the parameters are physically meaningful, and it is sufficiently flexible to accommodate a wide range of pulse shapes.

Mavroeidis and Papageorgiou (2003) also developed predictive equations for their model parameters using regression analysis with a dataset of near-fault pulselike records. They noted that the pulse period and amplitude are directly related to the rise time and slip velocity of faulting, respectively, and that the pulse period is strongly correlated with magnitude. They also observed trends with faulting mechanism: for the same earthquake magnitude, on average, the pulse period is largest for strike-slip faults, smallest for dip-slip faults, with oblique faults, which are a combination of strike-slip and dip-slip faults, being in between. Assuming the pulse period is independent of R for R less than 10km, they obtained

$$\log_{10} T_p = -2.2 + 0.4M_w \tag{2.18}$$

To satisfy the self-similarity condition, the above was modified to read

$$\log_{10} T_p = -2.9 + 0.5M_w \tag{2.19}$$

Although PGV and V_p appear to vary with M_w and R, Mavroeidis and Papageorgiou suggest using $V_p = 100$ cm/s because PGV mostly varies between 70 and 130cm/s for the entire range of magnitudes. They found no systematic relation for γ with M_w or R.

As pointed out later in this study, one shortcoming of the Mavroeidis and Papageorgiou (2003) model is that the algebraic area underneath the velocity pulse is not zero. This results in a non-zero residual displacement, which is not pysically compliant. A modified version of this model introduced in Chapter 3 addresses this shortcoming.

2.3.2.1.4 Extraction of velocity pulse by wavelet processing

Baker (2007) proposed an automated method to extract pulses from velocity time histories of near-fault ground motions by use of wavelet-based signal processing. The extracted pulse consists of the ten Daubechies wavelets of order 4 having the largest wavelet coefficients, as computed by the wavelet transform. Baker defines the pulse period as the pseudo-period of the largest wavelet, i.e. the period associated with the maximum Fourier amplitude of the wavelet having the largest wavelet coefficient. From linear regression analysis with a database of near-fault recordings, Baker obtained a relation between the pulse period and the earthquake magnitude, which is given by

$$\mathrm{E}\left[\ln T_p\right] = -5.78 + 1.02 M_w \tag{2.20}$$

This predictive model has an error standard deviation of $\sigma_{\ln T_p} = 0.55$, which is less than what he obtained when he used the pulse period corresponding to the peak spectral velocity, indicating that the proposed wavelet pseudo-period is better correlated with the earthquake magnitude than the pulse period defined in terms of the spectral shape.

2.3.2.2 Seismological ground motion simulation models

There are two types of numerical ground motion models: stochastic models based on random process theory, and seismological models based on the broadband Green's function method. The latter are based on the physics of earthquakes and include fewer idealizations. Seismological models typically represent the earthquake source as a shear dislocation on an extended fault plane, account for spatial and temporal variations of the slip on the rupture surface (the slip distribution is usually highly variable with asperities surrounded by regions of low slip), use theoretical or empirical Green's functions to represent wave propagation, and compute the time history using the elasto-dynamic representation theorem (Somerville, 2000). Complete Green's functions containing near, intermediate and far field terms should be used, and the ground motion is computed as the convolution of the slip time function $D(t)$ with the Green's function $G(t)$ for the appropriate distance and depth, integrated over the fault rupture surface (Somerville, 2002). Numerical ground motion models based on seismological theory have been developed and validated against recorded data, and they can be used to improve near- and far-field ground motion models by adding to the database of recorded ground motions (Somerville, 2000). However, these models tend to lack the high-frequency contents of recorded ground motions. For that reason, hybrid models

involving stochastic correction for high frequencies have been studied (Douglas and Aochi, 2008). Archuleta and Hartzell (1981) used a kinematic source model to simulate and study near-fault ground motions. They modeled the earthquake as a propagating stress drop over a finite area. For simplicity, they assumed a buried circular strike-slip fault in a half-space. They used a slip function consistent with a constant propagating stress drop, as derived by Kostrov in 1964, and assumed a constant rupture velocity equal to 0.9 times the shear-wave velocity. They modeled the wave propagation based on the Green's function for semi-infinite linear elastic isotopic homogeneous medium. They noted, however, that real earthquakes have a much more complex stress and geologic environments, which were not incorporated into their model, and which tend to complicate the ground motions (Archuleta and Hartzell, 1981).

2.3.3 Comparison of predictive equations for pulse parameters

As described above, several investigators have developed predictive equations for the directivity pulse period and pulse amplitude in terms of the earthquake magnitude and the closest distance to the fault. In some cases, local site conditions have also been taken into account. All investigators have obtained similar trends, but the predictive equations are different. This is due to the fact that the investigators have used different definitions of the pulse amplitude and pulse period, they have selected different definitions of what constitutes "near fault" (maximum distances considered range from 10km to 30km), and they have used different databases of recorded (and sometimes simulated) near-fault ground motions. It should be noted that all these relations are predictions of the mean pulse amplitude and the mean pulse period. A large scatter or even outliers exist in the data due to the complex nature of the earthquake phenomenon and the fact that the models exclude many other relevant variables. For example, for a given magnitude and distance, a larger than average stress drop will result in a shorter rise time and a shorter pulse period and vice versa (Mavroeidis and Papageorgiou, 2003); yet, most existing predictive equations do not include the stress drop or the rise time as explanatory variable.

Somerville (1998) has shown that the pulse period is related to certain source parameters, namely the rise time (duration of the slip at a single point on the fault) and the fault dimensions, which tend to increase with magnitude. He regressed the rise time against the earthquake magnitude with the self-similarity constraint between the two and obtained

$$\log_{10} T_R = -3.34 + 0.5M_w \tag{2.21}$$

Comparing with the predictive equation for the pulse period given in Eq. 2.3, one has

$$T_p = 2.2T_R \tag{2.22}$$

This result is consistent with the fact that the rise time is a lower bound on the period of the pulse in the case of a point-source, when ignoring wave propagation effects. It is also confirmed by a simple analytical fault-rupture model. Moreover, Somerville indicates a correlation between the rise time and the style of faulting, with the rise time for dip-slip earthquakes being on average about half the rise time for strike-slip earthquakes. The pulse period in a dip-slip earthquake is, thus, expected to be shorter than that in a strike-slip earthquake. Moreover, a smaller rise time results in a larger amplitude, a trend which is present in the current ground motion models.

Although many authors have noted the importance of the number of impulsive half-cycles as it may significantly affect the structural response in the inelastic range (Mavroeidis and Papageorgiou, 2002; Somerville, 1998), no predictive equations have been developed. There is a need to identify the conditions that give rise to multiple cycles or pulses. One such reason could be the existence of multiple asperities on the fault rupture plane, in which case the number of pulses depends on the slip distribution, which is difficult to predict, and on the relative locations of the hypocenter, the asperities and the site (Somerville, 1998). Conversely, a uniform slip distribution, or a slip concentrated in a single zone, would result in a well defined pulse sequence (unless local site effects introduce complexities), since all nearby stations will be at more or less equal distances from the region of high slip (Bray and Rodriguez-Marek, 2004).

2.4 PROBABILITY OF OCCURRENCE OF A PULSE

Not all near-fault ground motions contain a forward directivity pulse. Some sites experience backward directivity effects. Some sites record a forward directivity pulse even when they are not in a geometric configuration that is favorable for such an event. For example, in a strike-slip earthquake, if the hypocenter is located at some depth, the rupture will also propagate updip, and sites located updip but close to the epicenter will experience some forward directivity effect. Other sites do not experience a velocity pulse even though they may have a source to site geometry that is favorable to the forward directivity effect. One such case is when the site is located at the end of the fault rupture, where most of the slip is concentrated (Bray and Rodriguez-Marek, 2004). Additionally, the largest velocity pulse might occur in a direction other than the SN direction. Several explanations can be thought of; for example, the strike direction, which is usually defined based on an idealized fault plane, might not locally coincide with the actual fault orientation, or the anisotropy of the medium in which the waves propagate might result in a modification of the orientation of the largest pulse (Mavroeidis and Papageorgiou, 2002).

In the context of probabilistic seismic hazard analysis, prediction equations are needed for both pulselike and non-pulselike ground motions. The former are expected to yield ground motion levels that

are higher than what the current models predict, while the latter are expected to yield lower intensity ground motion levels. Pulse occurrence probability models are needed to combine the two cases into a single hazard estimate. Pulse occurrence probability models are also needed to simulate pulselike and non-pulselike near-fault ground motions in appropriate proportions.

Iervolino and Cornell (2008) and later Shahi and Baker (2011) used logistic regression to develop models of the pulse occurrence probability. In these regression models, the log of the ratio of the odds is assumed to be a linear function of selected explanatory variables. Iervolino and Cornell (2008) developed a model to predict the probability of occurrence of the pulse in the SN direction. They used a database of SN near-fault records within 30km of the fault rupture, which they divided into pulselike and non-pulselike records based on the classification method developed by Baker (2007). For strike-slip earthquakes, they found the model including geometric parameters R and θ to perform best, but they elected to use a model that includes all three geometric parameters R, s and θ. In a slightly modified form, their model reads

$$\Pr[\text{pulse}|R,s,\theta] = \frac{1}{1+\exp\left(-0.85925+0.11137R-0.018704s+0.04441\theta\right)} \tag{2.23}$$

where R and s are in kilometers and θ is in degrees. The model for non strike-slip earthquakes was selected to be of the same form, even though it was not the best performing model. This was done because the non-strike-slip models were found to be less robust, probably because of the heterogeneity of the data, as it comes from different fault mechanisms, and due to the fact that the explanatory variables used are actually calibrated for dip-slip earthquakes. The model has the form

$$\Pr[\text{pulse}|R,d,\phi] = \frac{1}{1+\exp\left(-0.55278+0.0551R-0.002669d+0.0271\theta\right)} \tag{2.24}$$

where R and d are in kilometers and ϕ is in degrees. In general, the predicted probabilities of occurrence of a pulse are smaller for non-strike-slip faults than for strike-slip faults. This is reasonable, since directivity conditions are more difficult to realize in the case of non-strike-slip earthquakes. Figure 2.11 shows plots of the probability of pulse occurrence for selected values of R, s or d, and θ or ϕ, where $R = s\tan\theta$ and $R = d\tan\phi$ are assumed for strike-slip and non-strike-slip faults, respectively. As expected, the pulse probability decreases with increasing distance R from the fault rupture (except for the case of a strike-slip fault with $\theta = 5^{\text{o}}$, probably because for this small angle a large R corresponds to a large s, which has the opposite effect) and with increasing angle θ or ϕ between the direction of propagation of the rupture and the direction of wave propagation between the hypocenter and the site. It should be noted from the sign of the coefficient of d in Eq. 2.24 and from Figure 2.11 that, for the case of a non-strike-slip fault, the probability of occurrence of a pulse decreases as d increases. This seems

counterintuitive, since a large rupture width d between the hypocenter and the site should favor the directivity effect. The reason might be that the information provided by R and ϕ is sufficient to describe the geometry, making d superfluous and, thus, resulting in this unexpected trend. A similar trend is observed for the variation with s in the case of a strike-slip fault with $\theta = 30^{\circ}$. For these reasons, this model is somewhat questionable.

Shahi and Baker (2011) adopted a somewhat different approach. They looked for pulses in all directions and classified a site as "pulselike" if it experienced a pulse in at least one direction. Using the obtained pulselike and non-pulselike databases, they first developed a model to predict the occurrence of a pulse at a site in at least one direction. They used the same explanatory variables as Iervolino and Cornell (2008). For the case of a strike-slip fault, they found that only R and s are significant, resulting in the relation:

$$\Pr[\text{pulselike}|R, s] = \frac{1}{1 + \exp\left(0.642 + 0.167R - 0.075s\right)} \tag{2.25}$$

For the case of a non-strike-slip fault, their model is

$$\Pr[\text{pulselike}|R, d, \phi] = \frac{1}{1 + \exp\left(0.128 + 0.055R - 0.061d + 0.036\phi\right)} \tag{2.26}$$

Letting α be the smaller angle between the orientation being considered and the strike of the fault, the fraction of pulselike ground motions that exhibit a pulse in direction α was fitted by a capped linear model by minimizing the squared error. Thus, the probability of having a pulse in direction α for strike-slip faults is given by

$$\Pr[\text{pulse in direction } \alpha|\text{pulselike}] = \min[0.67, 0.67 - 0.0041(77.5 - \alpha)] \tag{2.27}$$

and for non-strike-slip faults, it is given by

$$\Pr[\text{pulse in direction } \alpha|\text{pulselike}] = \min[0.53, 0.53 - 0.0041(70.2 - \alpha)] \tag{2.28}$$

According to the above models, the most likely and least likely orientations to observe a pulse are the SN and SP directions, respectively. The unconditional probability of observing a pulse in direction α is obtained as

$$\Pr[\text{pulse in direction } \alpha] = \Pr[\text{pulse in direction } \alpha|\text{pulselike}]\,\Pr[\text{pulselike}] \tag{2.29}$$

Figure 2.12 shows the probability of occurrence of a pulse at $\alpha = 90^{\circ}$, i.e. in the SN direction, with R, s or d, and θ or ϕ, where, for the sake of simplicity, $R = s\tan\theta$ and $R = d\tan\phi$ are assumed for strike-slip and non-strike-slip faults, respectively. As expected, the probability decreases with increasing distance R from the fault rupture, when s is fixed, and with increasing angle θ or ϕ between the direction

of rupture propagation and the direction of wave propagation between the hypocenter and the site. The probability increases with increasing s or d, except for the case of a strike-slip fault with $\theta = 30^{o}$, possibly because at this large angle an increase in s results in a large increase in R, which has the opposite effect. When the angle θ or ϕ is fixed, the trend with R is generally increasing or constant, due to the fact that, for given θ or ϕ, as R increases s or d increases, which has the opposite effect. The trends with R, s or d, and θ or ϕ of the model by Shahi and Baker are more reasonable than those of the model by Iervolino and Cornell (2008). In later chapters of this study, the model by Shahi and Baker (2011) is used to compute the probability of occurrence of a pulse in the SN direction at a site, given its geometric configuration relative to the fault.

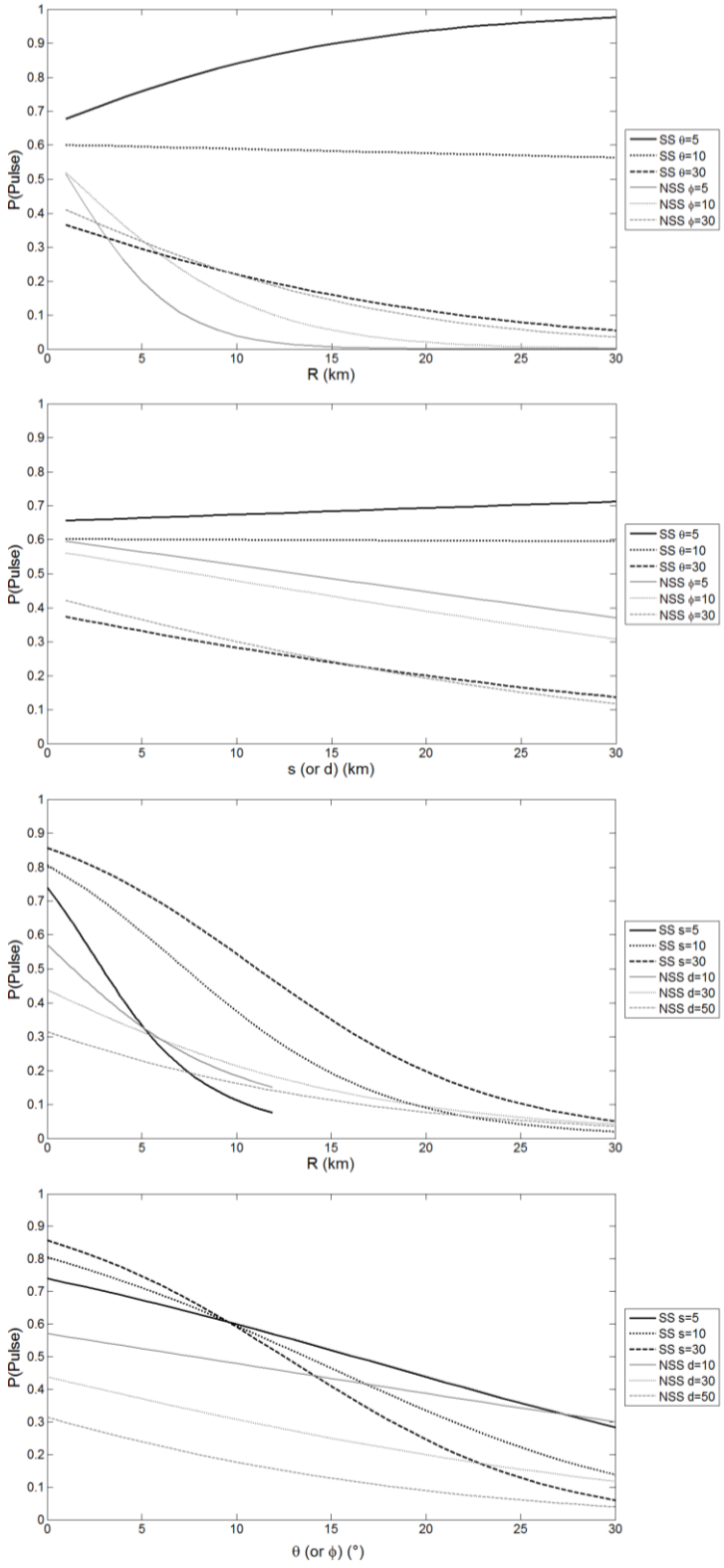

Figure 2.11: Probability of pulse occurrence in the SN direction versus directivity parameters for strike-slip (SS) and non-strike-slip (NSS) faults according to the model by Iervolino and Cornell (2008)

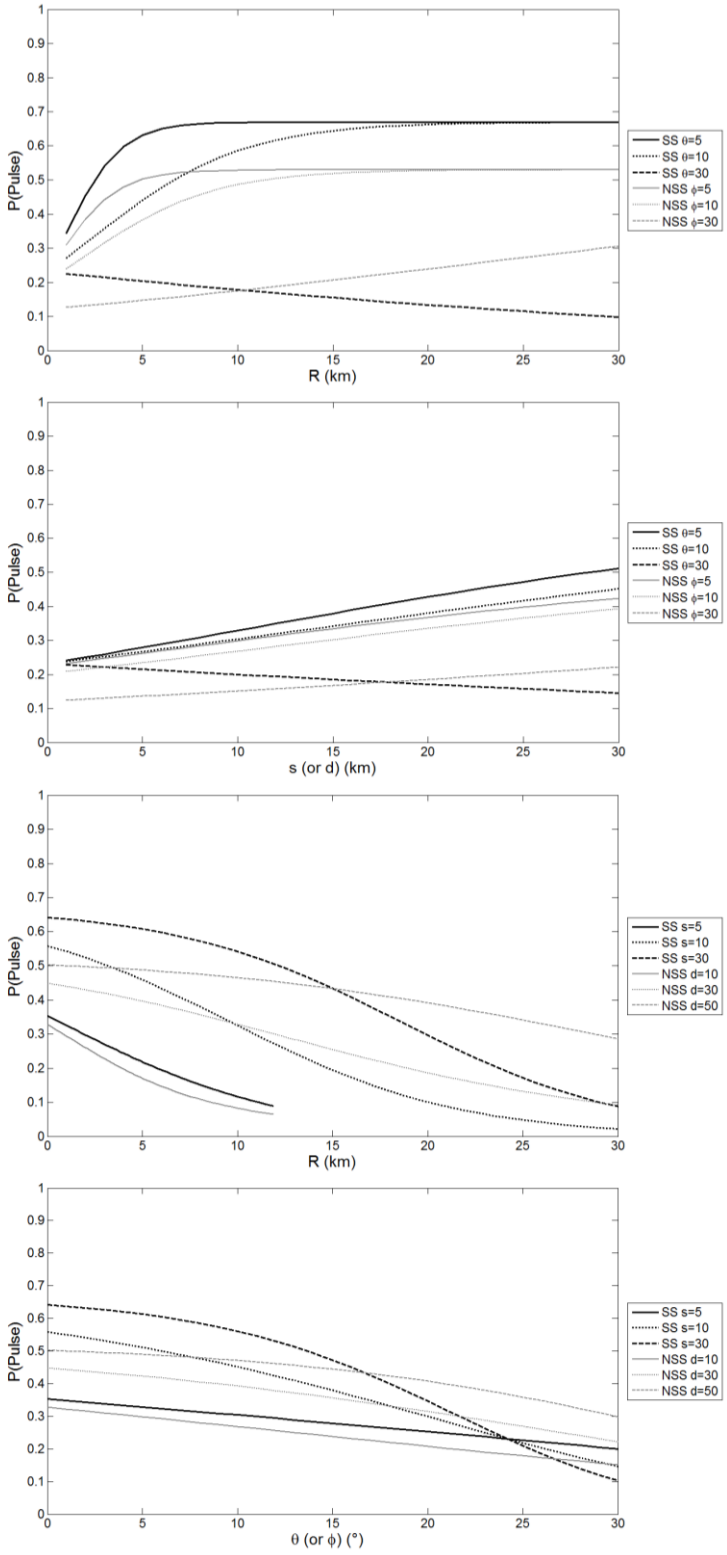

Figure 2.12: Probability of pulse occurrence in the SN direction versus directivity parameters for strike-slip (SS) and non-strike-slip (NSS) faults according to the model by Shahi and Baker (2011)

2.5 MODEL OF THE FLING STEP

The fling step is the permanent tectonic deformation of the ground. It appears in near-fault ground motion components parallel to the direction of slip. Abrahamson (2001) proposed a simple time domain model to represent the fling step, which is to be added to the FP ground motion time histories. The model is formulated in terms of three parameters: the amplitude of the fling, the period of the fling, and the arrival time of the fling. As shown in Figure 2.13, the fling is modeled as a single cycle of a sine wave in the acceleration time history.

Abrahamson (2001) proposed the following model to predict the average slip D_{fault} (in units of cm) on a fault as a function of the earthquake magnitude:

$$\ln D_{\text{fault}} = 1.15M_w - 2.83 \tag{2.30}$$

At the fault, the amplitude of the fling displacement, D_{site}, is assumed to be equal to half the average slip on the fault. The amplitude decreases with distance from the fault, while being equal and in opposite directions on the two sides of the fault. Abrahamson (2001) assumed the attenuation of the fling amplitude to follow the $\cot^{-1}$ model, which can also be written as

$$D_{\text{site}} = D_{\text{fault}}\left[\frac{1}{2} - \frac{\tan^{-1}(\alpha R)}{\pi}\right] \tag{2.31}$$

where R is the closest distance to fault rupture in km. Abrahamson (2001) also developed a model to predict the fling period,

$$\ln T_{\text{fling}} = -6.96 + 1.15M_w \tag{2.32}$$

The acceleration amplitude in units of g can then be estimated as

$$A_{\text{fling}} = \frac{D_{\text{site}}2\pi}{981T_{\text{fling}}^2} \tag{2.33}$$

It is conservatively assumed that the fling pulse arrives at the time of arrival of S-waves and that its polarity is such that constructive interference occurs between the fling and the S waves in the velocity time history.

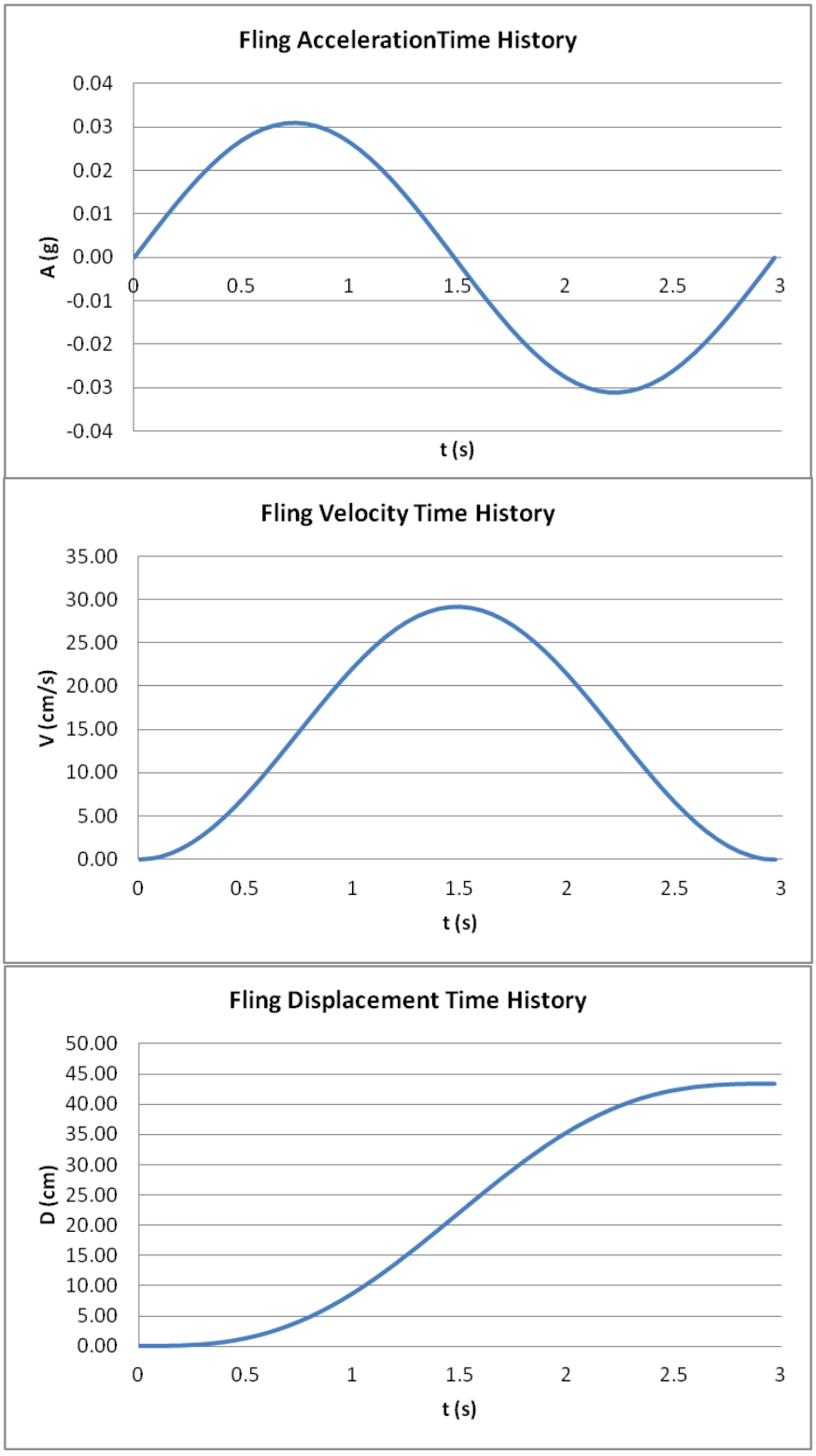

Figure 2.13: Time domain fling step model by Abrahamson (2001)

3 Stochastic Model of Near-Fault Ground Motion

3.1 INTRODUCTION

As we have seen in Chapter 2, near-fault ground motions possess distinct characteristics, which can have strong influence on the response of structures, particularly in the inelastic range. These characteristics include the rupture directivity effect in the FN or SN (fault-normal or strike-normal) direction and the fling step in the FP or SP (fault-parallel or strike-parallel) direction. A site in the near-field region of the fault may experience forward directivity when the fault rupture propagates towards the site with a velocity more or less equal to the shear-wave velocity of the ground medium. The resulting ground motion typically exhibits a large velocity pulse in the FN or SN direction, which may impose extreme demands on a structure. The fling step arises from the fault slip and manifests as a residual displacement at the end of the ground motion, in opposite directions on the two sides of the fault. Due to scarcity of recorded near-fault ground motions, there is interest in developing synthetic ground motions for near-fault sites, which can be used in performance-based earthquake engineering in addition to or in place of recorded motions. Obviously, it is crucial that such synthetic motions be realistic and have characteristics that are consistent with those of recorded near-fault ground motions.

In this chapter we develop a parameterized stochastic model of the near-fault ground motion in the SN direction, able to account for the directivity effect. Not all near-fault ground motions contain a forward directivity pulse, and our model is developed to cater for both the pulselike and non-pulselike cases. In the case of a pulselike ground motion, the stochastic model consists of two sub-models, one for the directivity pulse and one for the residual motion, i.e., the total motion minus the directivity pulse. An existing wavelet-based method by Baker (2007) is used to characterize the directivity pulse and extract it from the total motion of recorded accelerograms. A modified version of the idealized pulse model by Mavroeidis and Papageorgiou (2003) is employed and fitted to the extracted pulse, thereby generating a sample of data for the five parameters of the model. For the residual, a modified version of the non-stationary filtered white-noise model by Rezaeian and Der Kiureghian (2008, 2010) is employed and its seven parameters are identified by fitting to the database of residual motions. In the absence of a pulse, the non-stationary filtered white-noise model by Rezaeian and Der Kiureghian is directly used to model the ground motion and its seven parameters are directly fitted to the database of non-pulselike acceleration time histories.

In the present study, we do not consider the fling step in the FP or SP component of the near-fault ground motion. That component is being considered in a follow-up study, so that the two studies together will provide a complete bi-directional model of the near-fault ground motion.

In the subsequent sections of this chapter, we introduce the two sub-models and their parameterization. However, before doing that, we review and discuss other stochastic near-fault ground motion models that have been proposed in the literature, followed by a brief description of the pulse extraction algorithm developed by Baker (2007). One remark regarding notation: in this report we distinguish between the FN direction, which is perpendicular to the fault plane, and the SN direction, which is the horizontal direction perpendicular to the strike of the fault. Similarly, we make a distinction between the FP direction, which is in the plane of the fault in the direction of the slip, and the SP direction, which is the horizontal direction parallel to the strike of the fault. For a vertical strike-slip fault, the two pairs of directions naturally coincide.

3.2 EXISTING MODELS

Menun and Fu (2002, 2004), whose velocity pulse models were presented in Chapter 2, proposed a method for simulating near-fault pulselike ground motions at a site with specified seismic environment. They first noted that models developed to represent the velocity pulse, such as their 2002 and 2004 models, when fitted to recorded ground motions, did well at predicting the displacement demands caused by the recorded motion within a range of periods centered around the period of the pulse. However, this model underestimated demands outside of this range, especially at shorter periods. This is because the fitted pulse cannot replicate the frequency content beyond that associated with the pulse itself, namely it lacks the high frequency content (Fu and Menun, 2004; Menun and Fu, 2002). They thus proposed to model both the velocity pulse and the non-stationary high frequency content and to superimpose them. They opted for a stochastic process with a deterministic modulating function and randomly generated phase angles and frequency coefficients to model the high frequency content. They noted that, contrary to far-field ground motions that are typically characterized by an initial build up of energy followed by a relatively long quasi-stationary phase and a gradually decaying tail, the high frequency content of near-fault ground motions does not have a long, stationary strong motion phase. They fitted their model to a database of recorded ground motions in the SN direction and developed empirical relations to predict the model parameters, given the earthquake and site characteristics. They later used these predictive equations to generate synthetic pulselike ground motions for arbitrary sites. They evaluated the suitability of their model by comparing linear and nonlinear displacement demands imposed by recorded and simulated ground motions (Fu and Menun, 2004).

Mavroeidis and Papageorgiou (2003) also proposed a mathematical model of the velocity pulse (presented in Chapter 2) and noted that their model can accurately replicate the intermediate to long period features of near-fault pulselike ground motions, but not the high frequency content. They thus proposed a methodology to model and simulate realistic near-fault pulselike ground motions: they used their velocity pulse model to describe the coherent, long period velocity pulse, and they suggested using a stochastic approach based on a seismological source model (because of the small distance to the source) to describe the incoherent high frequency content. They fitted the parameters of the pulse model to a database of recorded pulselike ground motions in the SN direction, and developed empirical relations to predict the pulse model parameters, given the earthquake and site characteristics. They then used these predictive equations to generate a synthetic velocity pulse and the corresponding acceleration, to which they added a synthetic acceleration time history generated from a source model, such as the specific barrier model. The procedure involves additional details that are not presented here. The interested reader should consult their paper (Mavroeidis and Papageorgiou, 2003)..

The procedure we present in this study is similar in concept to that of Fu and Menun (2004). There are, however, several important differences. Firstly, we select different models to represent the velocity pulse and the high frequency content (or residual), while Fu and Menun (2004) do not make such a distinction. Secondly, Fu and Menun (2004) ignore the uncertainty inherent in the predictive equations and the correlations between the model parameters; they simply use the predicted mean values of the parameters as input to their model in order to simulate ground motions. We fully account for the parameter uncertainties and correlations; as a result our simulated models have the same level of variability as recorded near-fault ground motions with similar earthquake and site characteristics. Finally, we develop and fit our model to account for both pulselike and non-pulselike near-fault ground motions, while Fu and Menun only fit their model to pulselike ground motions.

3.3 EXTRACTION OF THE VELOCITY PULSE

Having a database of recorded near-fault ground motions, the first step is to determine whether or not each recorded motion contains a velocity pulse in the FN direction. In the case of strike-slip faults, the FN direction is typically the horizontal SN direction. For dip-slip faults, the FN direction has components in both the horizontal SN direction and the vertical direction. For now, and for simplicity, only the horizontal SN direction is examined for the presence of a pulse. It is noted, however, that in a recent work Shahi and Baker (2011) performed classification at several orientations to determine the range of orientations over which the motion is pulselike. In fact, a pulse might be present in a large range of

directions, including or excluding the SN direction (Shahi and Baker, 2011) , but these details are overlooked for now.

We use a quantitative method proposed by Baker (2007) to identify and extract pulses from the velocity time history of recorded ground motions. Prior to Baker's work, classification of near-fault records as pulselike or non-pulselike was based on visual identification of pulses and, thus, depended a lot on the analyst's judgment. Baker (2007) proposed an automated method for detecting pulses and classifying near-fault ground motions, which uses wavelet-based signal processing. The method identifies and extracts the largest velocity pulse from a ground motion and classifies it as an actual pulse or a non-pulse based on the value of a Pulse Indicator (PI). The approach only depends on signal-processing and cannot distinguish between the causal mechanisms of the pulse, i.e., whether the pulse is caused by forward directivity or some other phenomenon, such as an asperity in the fault rupture, basin effects, etc. Furthermore, the method cannot detect the fling step.

Similar to the way Fourier analysis decomposes a signal into the summation of sine waves of different amplitudes, periods and phase angles, wavelet analysis decomposes a signal into wavelets localized in time that represent a narrow range of frequencies. Since earthquake records are non-stationary signals, they are more easily represented by wavelets than by stationary sine waves. Wavelets are basis functions satisfying a set of mathematical requirements. There are many wavelet prototypes that can be used to decompose a signal. A Daubechies wavelet of order 4 (Figure 3.1) was selected by Baker because it approximates the shape of many velocity pulses. This mother wavelet is then scaled and translated in time to form a set of basis functions. Any signal can then be represented as a linear combination of these basis functions. The corresponding coefficients are determined from a convolution integral (or summation for digital signals) computed by the continuous wavelet transform. The presence of a pulse is indicated by a significant portion of the original record being described by one or a few wavelets with large coefficients (Baker, 2007).

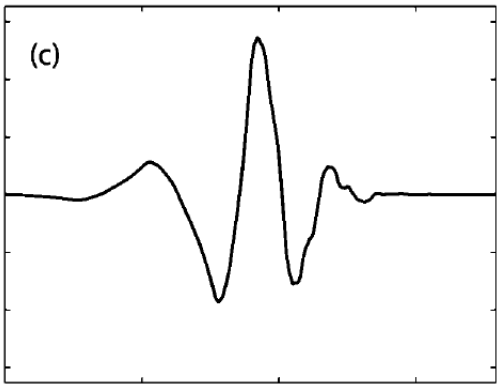

Figure 3.1: Daubechies wavelet of order 4 (from Baker, 2007)

The largest velocity pulse is identified and extracted as follows: Using the wavelet transform, the wavelet coefficients, which are also measures of the energy in each wavelet, are computed for the velocity time history. The wavelet having the largest coefficient, thus the largest energy, is subtracted from the original ground motion. This wavelet determines the period and location of the velocity pulse. The procedure is repeated on the time history from which the largest wavelet was subtracted, to extract the next largest wavelet having the same period and located in nearby times. This is repeated until the 10 largest wavelets are extracted. The sum of the 10 largest wavelets constitutes the extracted velocity pulse. The extracted pulse does not contain high frequency components; it captures the velocity and displacement time histories well, but not the acceleration time history. The residual velocity time history is defined as the original time history minus the extracted pulse (Baker, 2007).

According to Baker's method, ground motions are classified as pulselike or non-pulselike based on the significance of the extracted pulse relative to the original ground motion. This is measured by a Pulse Indicator (PI) defined by Baker (2007) and computed for each SN rotated velocity time history. Baker first manually classified the SN rotated records from the NGA database (with $5.5 < M_w$ and $R < 30$km) as pulselike, non-pulselike and ambiguous by visual inspection. He then built a statistical predictive model to reproduce the manual classifications as closely as possible. He found two intuitive and easy-to-compute variables to have good predictive ability: The PGV ratio (ratio of the PGV of the residual to the PGV of the original ground motion) and the energy ratio (ratio of the energy of the residual to the energy of the original ground motion, where energy is computed as the cumulative squared velocity of the record). The predictive equation for the pulse indicator, obtained using logistic regression, is given by

$$PI = \frac{1}{1 + \exp[-23.3 + 14.6(\text{PGV ratio}) + 20.5(\text{Energy ratio})]} \tag{3.1}$$

The PI takes values between 0 and 1; the higher the value, the stronger the indication that the motion is pulselike. Baker selected thresholds for the automated classification procedure based on the value of the PI computed for each record. Thus, records with PI greater than 0.85 are classified as pulselike, records with PI less than 0.15 are classified as non-pulselike, and the remaining records are classified as ambiguous (Baker, 2007).

Up to this point, the extraction and classification procedure only depends on processing of the ground motion record and conveys no information about whether the pulse is caused by forward directivity or not. Baker thus includes two additional criteria that should be satisfied for the record to be classified as pulselike: (1) the pulse should arrive early in the ground motion record, as is the case with forward directivity pulses, and (2) the PGV of the record should be greater than 30cm/s to exclude lower

intensity ground motions that may appear pulselike only because their time history is simple. With this classification procedure, Baker (2007) identified 91 records from the NGA database to be pulselike in the SN direction.

Having identified and extracted the velocity pulse from a pulselike record, it is important to identify the period of the pulse in order to compare it with the fundamental period of a structure, as it can strongly influence the response. Contrary to sine waves, there is no well defined concept of period for wavelets. Baker defines the pulse period as the pseudo-period of the largest wavelet, i.e., the period associated with the maximum Fourier amplitude of the wavelet having the largest wavelet coefficient. It is worth noting that the wavelet pseudo-period is generally slightly larger than the period associated with the peak velocity response spectrum of the original record(Baker, 2007).

In this study, we use Baker's algorithm to identify SN components of near-fault ground motions that are pulselike and to extract the pulse from their velocity time histories. The derivative of the extracted velocity pulse is then subtracted from the total acceleration time history to obtain the residual acceleration time history.

3.4 MODEL OF THE VELOCITY PULSE

For the purpose of developing a stochastic model of the near-fault ground motion, we need a simple mathematical model of the directivity pulse in terms of a few, preferably physically meaningful, parameters.. After examining several models proposed in the literature and reviewed in Chapter 2, we selected the analytical forward directivity pulse model proposed by Mavroeidis and Papageorgiou (2003). In its original formulation, the model for the velocity pulse consists of the product of a harmonic function and a bell-shaped envelope function (a shifted haversed sine function). Although the expression is given in Chapter 2, we repeat it here for convenience:

$$\begin{aligned} v(t) &= \frac{1}{2}V_p\left\{1+\cos\left[\frac{2\pi}{\gamma}\left(\frac{t-t_0}{T_p}\right)\right]\right\}\cos\left[2\pi\left(\frac{t-t_0}{T_p}\right)+\nu\right] \quad t_0-\frac{\gamma}{2}T_p < t \le t_0+\frac{\gamma}{2}T_p \\ &= 0 \qquad\qquad \text{elsewhere} \end{aligned} \tag{3.2}$$

The five model parameters are: the pulse amplitude V_p, the pulse period T_p, parameter γ characterizing the number of oscillations in the pulse, the phase angle ν, and the time of the peak of the envelope t_0. Closed-form expressions for the corresponding acceleration and displacement time histories are given in Mavroeidis and Papageorgiou (2003). The above formulation, however, results in a non-zero displacement at the end of the pulse given by

$$D_r = V_p T_p \frac{\sin(\nu + \gamma\pi) - \sin(\nu - \gamma\pi)}{4\pi(1-\gamma^2)} \tag{3.3}$$

We address this problem by slightly modifying the pulse model to achieve zero residual displacement. Specifically, we add to the expression in (3.2) a shifted haversed sine function of the same form as in the original formulation and set its amplitude so as to achieve zero displacement at the conclusion of the pulse. Replacing t_0 by $t_{max,p}$ and rearranging terms, the resulting expression of the velocity pulse is

$$\begin{aligned} v(t) &= \left\{\frac{1}{2}V_p \cos\left[2\pi\left(\frac{t-t_{max,p}}{T_p}\right)+\nu\right] - \frac{D_r}{\gamma T_p}\right\}\left\{1+\cos\left[\frac{2\pi}{\gamma}\left(\frac{t-t_{max,p}}{T_p}\right)\right]\right\} \quad t_{max,p} - \frac{\gamma}{2}T_p < t \le t_{max,p} + \frac{\gamma}{2}T_p \\ &= 0 \qquad\qquad \text{elsewhere} \end{aligned} \tag{3.4}$$

Note that the modified pulse is still defined by the five parameters described earlier. Hereafter, we call the model defined by (3.3) and (3.4) as the modified Mavroeidis-Papageorgiou (mMP) pulse model. In this study, we fit this model to extracted velocity pulses and later use it to simulate velocity pulses.

3.5 MODEL OF THE RESIDUAL AND NON-PULSELIKE GROUND MOTION

The residual motion is defined as the remainder of the acceleration time series after subtracting the derivative of the velocity pulse. The residual motion is typically a broad-band process with slowly evolving temporal and spectral characteristics. Following Rezaeian and Der Kiureghian (2008, 2010), we model it as a modulated, filtered white-noise process with the filter having time varying parameters. The model for the acceleration process is described as

$$a(t) = q(t)\left\{\frac{1}{\sigma_h(t)}\int_{-\infty}^{t} h[t-\tau, \boldsymbol{\lambda}(\tau)]w(\tau)d\tau\right\} \tag{3.5}$$

where $w(t)$ is a white-noise process, $h[t-\tau, \boldsymbol{\lambda}(\tau)]$ is the unit-impulse response function (IRF) of a linear filter with time-varying parameters $\boldsymbol{\lambda}(\tau) = [\omega_f(\tau), \zeta_f(\tau)]$, $\sigma_h(t)$ is the standard deviation of the process defined by the integral (so that the process inside the curled brackets has unit variance), and $q(t)$ is a time-modulating function that characterizes the root-mean-square of the acceleration process. For the IRF, the form selected in Rezaeian and Der Kiureghian (2008) is adopted:

$$\begin{aligned} h[t-\tau, \boldsymbol{\lambda}(\tau)] &= \frac{\omega_f(\tau)}{\sqrt{1-\zeta_f^2(\tau)}} \exp\left[-\zeta_f(\tau)\omega_f(\tau)(t-\tau)\right] \times \sin\left[\omega_f(\tau)\sqrt{1-\zeta_f^2(\tau)}(t-\tau)\right] \quad \tau \le t \\ &= 0 \qquad\qquad \text{elsewhere} \end{aligned} \tag{3.6}$$

For the modulating function $q(t)$, Rezaeian and Der Kiureghian (2008) used a 3-parameter model that is proportional to the gamma probability density function. That model was found to be appropriate for far-field ground motions. However, as also noted by Fu and Menun (2004), while far-field ground motions are typically characterized by an initial build up of energy followed by a relatively long quasi-stationary phase and a gradually decaying tail, near-fault ground motions do not have a long quasi-stationary strong-motion phase. Thus, we replace the gamma modulating function by a 4-parameter piecewise function that exhibits sharper build-up and decay segments with no quasi-stationary phase in between. Starting at t_0, the modulating function peaks at time $t_{max,r}$ and consists of a build-up phase in the form of a polynomial of order α up to $t_{max,r}$, followed by a decay phase in the form of an exponential function decaying at a rate of β. Parameter c controls the amplitude of the modulating function, which is given by

$$q(t) = \begin{cases} 0 & t \le t_0 \\ c\left(\dfrac{t - t_0}{t_{max,r} - t_0}\right)^{\alpha} & t_0 < t \le t_{max,r} \\ c\exp\left[-\beta(t - t_{max,r})\right] & t_{max,r} < t \end{cases} \tag{3.7}$$

Of the four parameters, $t_{max,r}$ is the time of the maximum of the root-mean-square of the acceleration process. Following Rezaeian and Der Kiureghian (2010), the remaining three parameters (c, α, β) are mapped onto the physical quantities of the expected Arias intensity, I_a, the effective duration, D_{5-95} (corresponding to the interval between 5% and 95% of Arias intensity values), and the time to the 30% Arias intensity value, t_{30}, as described in greater detail in Chapter 4. Figure 3.2 shows plots of the modulating function for selected typical values of the model parameters. The initial part of the modulating function is convex when $\alpha < 1$, linear when $\alpha = 1$ and concave when $\alpha > 1$. Parameter β controls the shape of the tail of the modulating function; as β increases energy decays more rapidly.

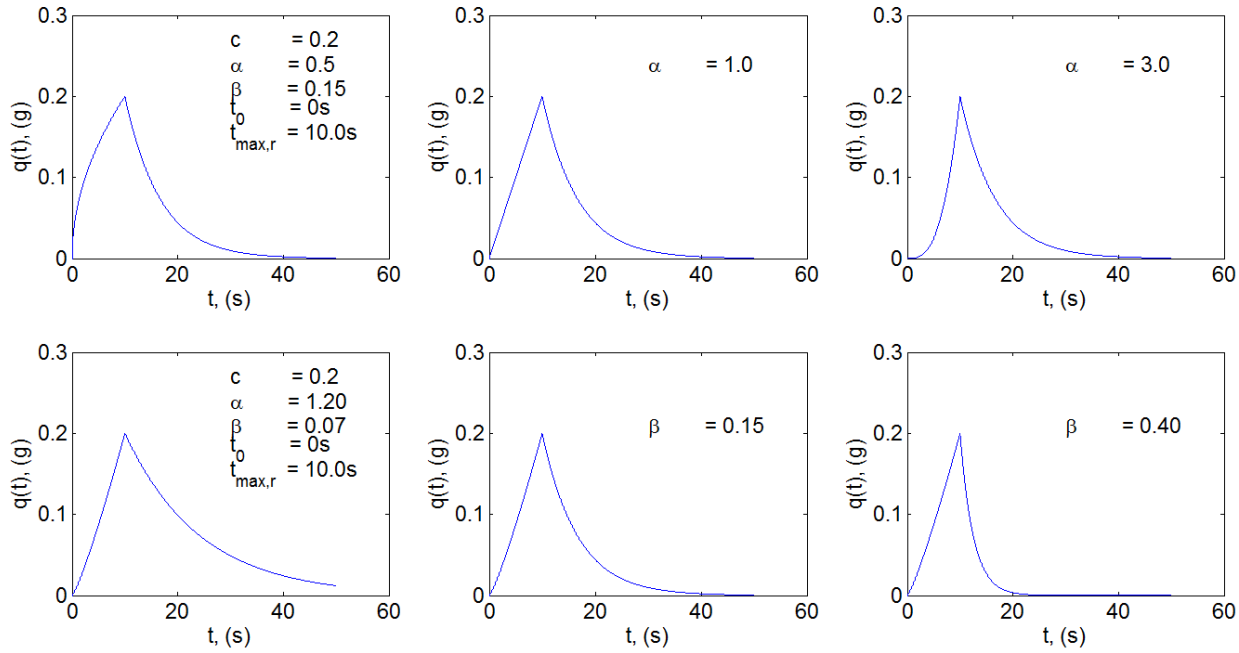

Figure 3.2: Plots of the modulating function for selected model parameter values; varying α parameter (top) and varying β parameter (bottom)

One of the advantages of using the model by Rezaeian and Der Kiureghian (2008, 2010) is that it separates the temporal and spectral non-stationarities of the process, so that the selection and fitting) of the modulating function is independent of the selection and fitting of the IRF. This advantage will be exploited in Chapter 4 when identifying the model parameters from recorded motions.

For the filter frequency, which represents the predominant frequency of the residual motion, the linear form:

$$\omega_f(\tau) = \omega_{mid} + \omega'(\tau - t_{45}) \tag{3.8}$$

used by Rezaeian and Der Kiureghian (2008, 2010) is adopted, where ω_{mid} is the filter frequency at the middle of the ground shaking, taken as the time t_{45} to the 45% Arias intensity value of the residual motion, and ω' is the rate of change of the frequency with time. Finally, the filter damping, representing the bandwidth of the process, is taken to be a constant,

$$\zeta_f(\tau) = \zeta_f \tag{3.9}$$

as was also done in Rezaeian and Der Kiureghian (2010). Thus, the seven physically relevant parameters $(I_a, D_{5-95}, t_{30}, t_{max,r}, \omega_{mid}, \omega', \zeta_f)$ completely define the process representing the residual motion. In the following chapter, we describe a method for estimating these parameters.

We expect non-pulselike near-fault ground motions to have characteristics that are similar to those of the residuals of pulselike near-fault ground motions after removal of the pulse. Hence, the same model as described above is used to describe non-pulselike near-fault ground motions.

4 Estimation of Model Parameters

4.1 INTRODUCTION

Having formulated the model for both pulselike and non-pulselike near-fault ground motions in Chapter 3, we next estimate the model parameters by fitting to recorded near-fault ground motions. The 12 parameters of the pulselike model, consisting of the 5 parameters $(V_p, T_p, \gamma, \nu, t_{max,p})$ of the pulse (see Eq. 3.4) and the 7 parameters $(\alpha, \beta, c, t_{max,r}, \omega_{mid}, \omega', \zeta_f)$ of the residual motion (see Eqs. 3.5-3.9), are fitted to pulselike motions, while the 7 parameters $(\alpha, \beta, c, t_{max}, \omega_{mid}, \omega', \zeta_f)$ of the non-pulselike model are fitted to non-pulselike ground motions. For each pulselike record, the parameters of the pulse model are determined by first extracting the velocity pulse by use of Baker's wavelet method (Baker 2007) and then fitting to it the modified Mavroeidis-Papageorgiou (mMP) model defined in Eq. 3.4. The parameter values are determined by minimizing the difference between the extracted pulse and the idealized mMP pulse. The parameters of the model for the residual motion or for non-pulselike motions are determining by use of the statistical characteristics of the recorded motion, i.e., the cumulative mean square (Arias intensity), the cumulative number of zero-level crossings, and the cumulative number of negative peaks and positive minima, by methods described in Rezaeian and Der Kiureghian (2010). Details are presented below. Once the model parameters for the available database of recorded near-fault ground motions are determined, the sample of estimated parameters is used to develop empirical predictive equations by regressing the model parameters (in a transformed space) against earthquake and site characteristics, such as the earthquake magnitude, the type of faulting, the position of the site relative to the potential fault rupture, and the shear-wave velocity of the site. In Chapter 5, these predictive equations are used to generate sets of model parameters, which are in turn used in the stochastic models developed in Chapter 3 to generate suites of synthetic ground motions for given earthquake and site characteristics.

In this chapter, we first present the database of SN near-fault ground motions used in the study. We then describe the methods of fitting and parameter identification for the pulse and the residual motions. The samples of identified parameters are then fitted marginal distributions. Empirical predictive equations of the pulse and residual model parameters are next developed by regression analysis of the data after transformation to the normal space. Estimated correlation coefficients between the regression residuals provide estimates of the correlations between the model parameters in the normal space. The same procedure is used to estimate the parameters of the model for non-pulselike near-fault ground

motions. However, this analysis is still in progress and final results are not included in this report. They will be included in an expanded version of this report in due time.

4.2 DATABASE OF NEAR-FAULT GROUND MOTIONS

The data used in this study consists of the near-fault records listed in the Pacific Earthquake Engineering Research (PEER)'s Next Generation Attenuation (NGA) database (http://peer.berkeley.edu/nga/). Only records with closest distance to the fault rupture $R \leq 30$km are considered. In order to have a reasonable sample size, no limit is set for the shear-wave velocity V_{s30} at the recording site; the effect of the local site is partially accounted for by including V_{s30} as a predictive variable in the regressions. Only records from shallow crustal earthquakes in active tectonic regions are considered. The data was recently expanded to include records from the March 2011 unofficial version of the NGA West 2 database, which is currently under development. This data was provided to us by Dr. J. Baker with permission from PEER.

The pulse classification for the near-fault records in the database was performed by Shahi and Baker (2011) based on the wavelet-based method of Baker (2007) to identify and extract "directivity pulses". They identified the ground motions in the NGA West 2 database displaying a pulse in any orientation, as well as those with a pulse in the SN direction, which is the direction of interest in this study. Restricting the latter group to those that have closest distance to the fault rupture less than 30km, we end up with a sample of 100 recorded motions that are pulselike in the SN direction. This data is summarized in a table at the end of this chapter. For each ground motion record in this data set, Shahi and Baker provided us with the acceleration and velocity time histories rotated to the SN direction of the total ground motion, the extracted pulse, and the corresponding residual motion (total ground motion minus the pulse motion).

From PEER's NGA database, 571 near-fault recorded motions in the SN direction are identified as non-pulselike. They constitute the non-pulselike database of recorded motions that will be used for estimating the model parameters for the non-pulselike near-fault ground motion.

4.3 IDENTIFICATION OF MODEL PARAMETERS FOR PULSELIKE MOTIONS

For each pulselike ground motion record, the parameters $(V_p, T_p, \gamma, \nu, t_{max,p})$ of the mMP pulse model are identified by fitting the model to the pulse extracted from the record by use of Baker's method. The fitting is done by use of an optimization algorithm that minimizes the squared difference between the two velocity pulse waveforms. To overcome arbitrariness in the starting time of a recorded motion, parameter t_0 (see Eq. 3.7) of the residual model is set to the 0.01% Arias intensity (to be defined below) point of the

recorded residual motion. Parameter $t_{max,p}$ of the velocity pulse, which denotes the time of the peak of the pulse envelope (see Eq. 3.4), is then measured from t_0. In a few cases, the residual acceleration record does not start from a zero value because of premature truncation. In these cases, t_0 is set by visual inspection.

The FN component of the NGA record number 285, which was recorded at the Bagnoli Irpinio Station during the 1980 Irpinia earthquake in Italy, will be used throughout this report to illustrate the fitting and simulation procedures. The acceleration, velocity and displacement time histories of this record are plotted in Figure 4.1. The acceleration time history of the velocity pulse extracted from this record, as well as that of the resulting residual and total motions are plotted in Figure 4.2. Figure 4.3 shows the fit of the mBP pulse to the extracted velocity pulse using the method described above, as well as the corresponding displacement waveforms. The identified model parameter values are listed in Table 4.1. It can be seen that the fit to the extracted velocity pulse is excellent, and that the fit to the corresponding displacement waveform is also quite good. Note that the fitted displacement waveform has zero residual displacement. This would not have been the case had we used the original Mavroeidis and Papageorgiou (2003) pulse model. The adequacy of the fit is also confirmed by comparing the pseudo-acceleration response spectra of the extracted and fitted pulses together with that of the total recorded motion, see Figure 4.4. The response spectrum of the extracted pulse captures the shape of the response spectrum of the total acceleration at periods longer than 1s. Furthermore, the response spectrum of the fitted pulse closely matches that of the extracted pulse, especially at periods longer than about 0.7s.

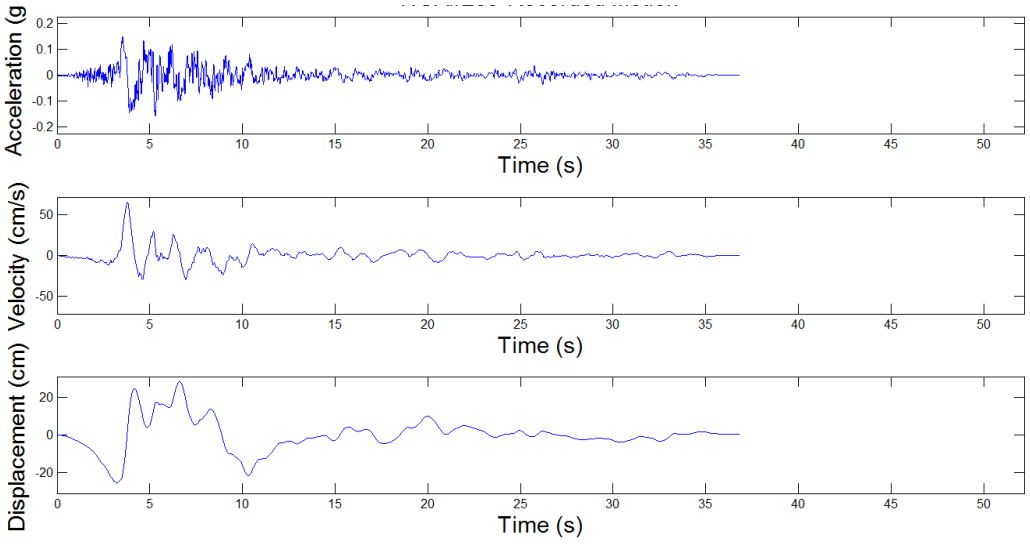

Figure 4.1: Acceleration, velocity and displacement time histories of NGA record #285

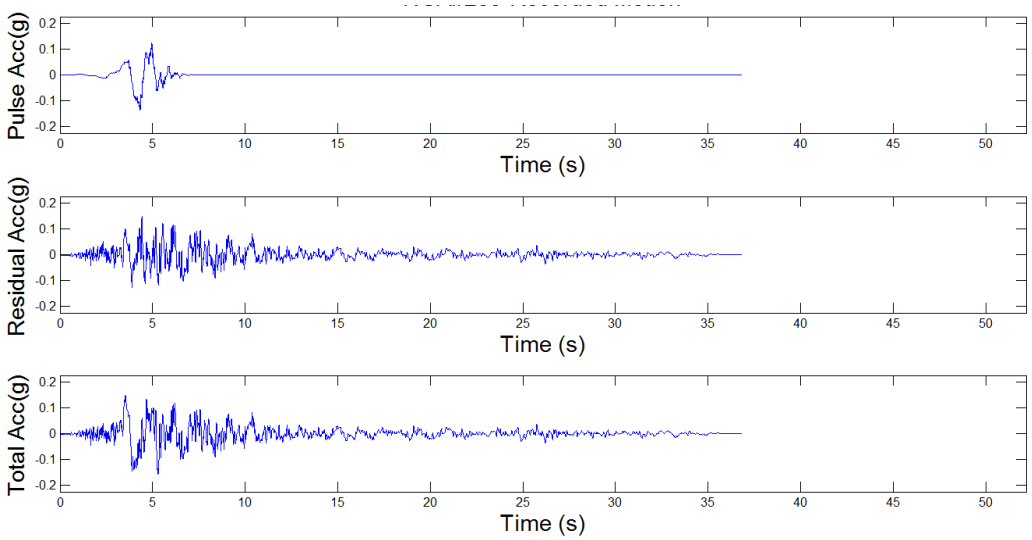

Figure 4.2: Acceleration time history (bottom), derivative of extracted velocity pulse (top), and residual acceleration time history (middle) of NGA record #285

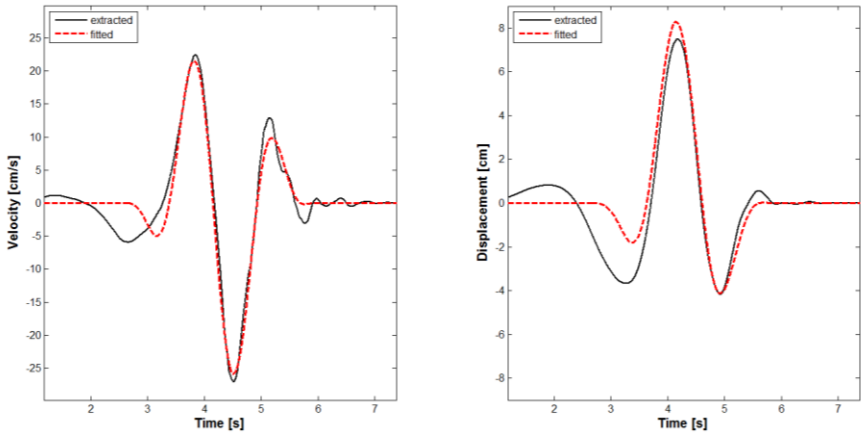

Figure 4.3: Extracted and fitted velocity pulses and corresponding displacement waveforms for NGA record #285

Table 4.1: Identified pulse model parameters for NGA record #285

	V_p	T_p	γ	ν/π	$t_{max,p}$
	cm/s	s		rad	s
NGA#285	27.1	1.55	2.13	0.662	4.28

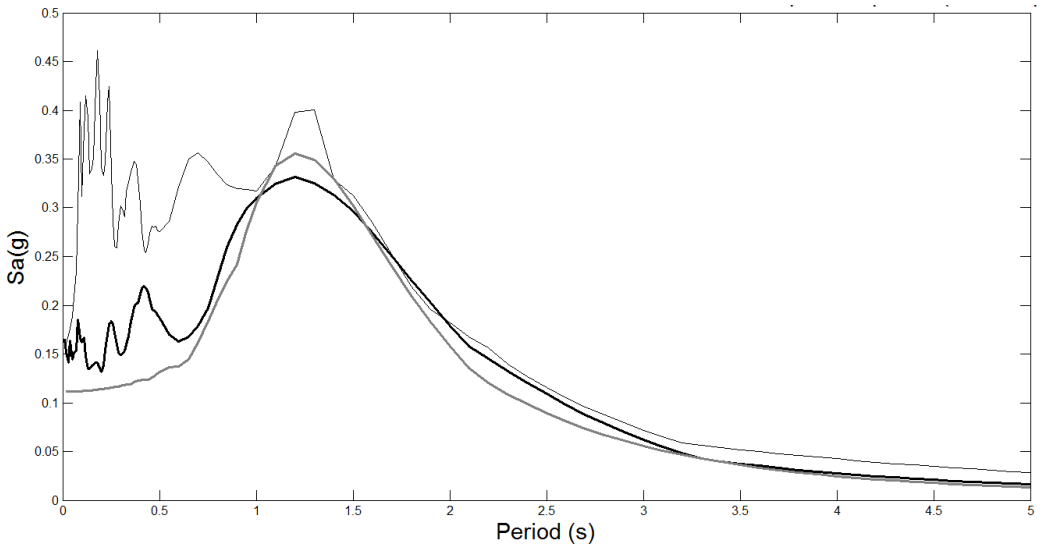

Figure 4.4: Pseudo-acceleration response spectra at 5% damping of recorded motion (thin grey line), extracted pulse (thick black line) and fitted pulse (thick grey line) for NGA record #285

In a similar manner, the seven parameters $(\alpha, \beta, c, t_{max,r}, \omega_{mid}, \omega', \zeta_f)$ of the residual model are fitted to the residual acceleration of each pulselike ground motion record. One of the advantages of the non-stationary filtered white-noise model by Rezaeian and Der Kiureghian (2008) is that it separates the temporal and spectral non-stationarities of the process, thus allowing the selection and fitting of the modulating function to be independent of the selection and fitting of the filter model. The details are described below.

It is preferable to relate the four parameters $(\alpha, \beta, c, t_{max,r})$ of the modulating function (see Eq. 3.7) to physically meaningful characteristics of the ground motion. We first set $t_{max,r}$, i.e., the time at which the modulating function takes its maximum value, equal to the time at which the smoothed root-mean-square function of the residual acceleration time history takes its maximum value. Since the database consists of near-fault ground motions, a clear peak in the smoothed root-mean-square residual acceleration is observed for most records. In some cases, however, two or more large peaks are observed, in which case setting $t_{max,r}$ equal to the time of the earliest peak usually provides a good fit. In a few cases where these selections result in inadequate fit of the modulating function, $t_{max,r}$ is selected in between the times of the large peaks such that an acceptable fit of the modulating function to the smoothed root-mean-square function is visually achieved. The remaining parameters α, β and c are related to the Arias intensity I_a, effective duration D_{5-95}, and the time to the 30% of Arias intensity, t_{30}, of the residual acceleration process. Denoting the residual acceleration process as $x_r(t)$, its Arias intensity, which is a measure of the total energy in the motion, is defined as

$$I_a = E\left[\frac{\pi}{2g}\int_0^{t_n} x_r^2(t)dt\right]$$
$$= \frac{\pi}{2g}\int_0^{t_n} q^2\left(t;\alpha,\beta,c,t_{max,r}\right)dt \tag{4.1}$$

where g is the gravitational acceleration and t_n is the total duration of the ground motion. The second equation is obtained by switching the orders of the expectation and integration operations and noting that the modulating function is identical to the mean-square function of the process. D_{5-95} is the effective duration of the residual ground motion defined as the time between the 5% and 95% time points of the cumulative Arias intensity function of the residual. More details about these two parameters are available in Rezaeian and Der Kiureghian (2010). Lastly, t_{30} is the time at which 30% of the cumulative Arias intensity of the residual is reached. This is measured from t_0, the "starting" time of the residual ground motion as defined earlier.

A Husid plot is a plot of the time history of the normalized Arias intensity of an acceleration time history (in %) showing the buildup of the energy of the ground motion over time. Following Rezaeian and Der Kiureghian (2008, 2010), we perform fitting of the selected modulating function by matching it to the Husid plot of the target residual acceleration as closely as possible. This is done by matching the Arias intensity, the effective duration, and the time of the 30% Arias intensity of the modulating function to those of the target residual acceleration. For the selected form of the modulating function, assuming $t_5 < t_{max,r} < t_{95}$, we can easily show that

$$t_5 = t_0 + \left(t_{max,r} - t_0\right)\left[0.05 + \frac{0.05(2\beta+1)}{2\alpha\left(t_{max,r} - t_0\right)}\right]^{1/(2\beta+1)} \tag{4.2}$$

$$t_{95} = t_{max,r} + \left(-\frac{1}{2\alpha}\right)\ln\left[0.05 + \frac{0.05(2\alpha)\left(t_{max,r} - t_0\right)}{2\beta+1}\right] \tag{4.3}$$

$$t_{30} = t_0 + \left(t_{max,r} - t_0\right)\left[0.30 + \frac{0.30(2\beta+1)}{2\alpha\left(t_{max,r} - t_0\right)}\right]^{1/(2\beta+1)} \qquad t_{30} \le t_{max,r}$$
$$= t_{max,r} + \left(-\frac{1}{2\alpha}\right)\ln\left[0.70 + \frac{0.70(2\alpha)\left(t_{max,r} - t_0\right)}{2\beta+1}\right] \qquad t_{max,r} < t_{30} \tag{4.4}$$

We identify parameters α and β of the modulating function by solving the simultaneous equations

$$t_{95}(\alpha,\beta) - t_5(\alpha,\beta) = D_{5-95,\text{target}} \tag{4.5}$$

$$t_{30}(\alpha,\beta) - t_0 = t_{30,\text{target}} \tag{4.6}$$

where $D_{5-95,\text{target}}$ and $t_{30,\text{target}}$ are the values for the residual acceleration record, the latter measured from t_0. These simultaneous equations are solved numerically by minimizing the sum of the squared differences between the two sides of the two equations. With α and β identified, parameter c is determined by setting the Arias intensity of the recorded residual equal to that of the model residual process. Using the second line of Eq. 4.1, it can be shown that for large t_n,

$$I_a = \frac{\pi}{2g}\int_0^{t_n} q^2\left(t;\alpha,\beta,c,t_{max,r}\right)dt = \frac{\pi}{2g}c^2\left[\frac{t_{max,r}-t_0}{2\beta+1}+\frac{1}{2\alpha}\right] \tag{4.7}$$

Thus,

$$c = \sqrt{\frac{I_{a,\text{target}}}{\frac{\pi}{2g}\left(\frac{t_{max,r}-t_0}{2\beta+1}+\frac{1}{2\alpha}\right)}} \tag{4.8}$$

where $I_{a,\text{target}}$ is the Arias intensity of the recorded residual acceleration. Later, for the purpose of simulating the residual acceleration of a pulselike motion, the values of I_a, D_{5-95}, and t_{30} are first simulated. These are used along with Eqs. 4.5, 4.6 and 4.8 to back-calculate α, β and c, which are then used together with $t_{max,r}$ and $t_0 = 0$ to compute the simulated modulating function.

As an example, Figure 4.5(a) shows the fitted modulating function over the acceleration time history of the residual ground motion in the FN direction of the NGA record number 285. Part (b) of the same figure shows the Husid plots for both the recorded residual acceleration and the fitted modulating function. Accuracy of the fit can be readily examined. It is noted that the two Husid plots, which are normalized by the Arias intensity of the residual ground motion, intersect at 30% and 100% Arias intensity times. The two figures also show the identified model parameter values and the percent error in the fit, which is defined as the area between the Husid curves of the recorded residual motion and the fitted modulating function divided by the effective duration D_{5-95} of the recorded residual motion.

$$Error = \frac{\int_0^{t_n} abs\left(I_{a,\text{target}}(t) - I_{a,\text{fitted}}(t)\right)dt / I_{a,\text{target}}(t_n)}{D_{5-95}} \tag{4.9}$$

The three parameters $(\omega_{mid}, \omega', \zeta_f)$ of the filter control the evolving predominant frequency and the bandwidth of the residual acceleration process. Specifically, ω_{mid} defines the predominant frequency in the middle of the ground shaking, ω' defines the rate of change of the predominant frequency with time (assuming the change is linear in time, see Eq. 3.8), and ζ_f controls the bandwidth of the process. Following Rezaeian and Der Kiureghian (2010), parameters ω_{mid} and ω' are identified by fitting a second-order polynomial to the cumulative number of zero-level up-crossings of the recorded residual

acceleration time history. Parameter ω_{mid} is taken as the slope of the fitted polynomial at the middle of the strong shaking, which is defined as the time t_{45} at 45% of Arias intensity of the record. Parameter ω' is determined as the second derivative of the fitted polynomial. Figure 4.5(c) shows this procedure for the recorded residual motion mentioned above. Following Rezaeian and Der Kiureghian (2010), the bandwidth of the process is measured in terms of the rate of positive minima and negative maxima. With the identified filter frequency parameters ω_{mid} and ω', a set of motions are simulated with varying filter damping ζ_f. The expected cumulative number of positive minima and negative maxima of these simulated motions are compared with the corresponding cumulative curve of the residual motion. The filter damping value that has a similar rate (slope of the cumulative curve) is selected as the value of parameter ζ_f. Figure 4.5(d) shows this process. All the identified parameter values of the residual model are listed in Table 4.2. More details about these fitting procedures can be found in Rezaeian and Der Kiureghian (2010).

Table 4.2: Identified residual model parameters for NGA record #285

	$I_a/\left(\frac{\pi}{2g}\right)$	D_{5-95}	t_{30}	$t_{max,r}$	ω_{mid}	ω'	ζ_f
	g^2s	s	s	s	Hz	Hz/s	
NGA#285	0.0209	17.4	4.75	4.58	4.58	-2.87E-02	0.23

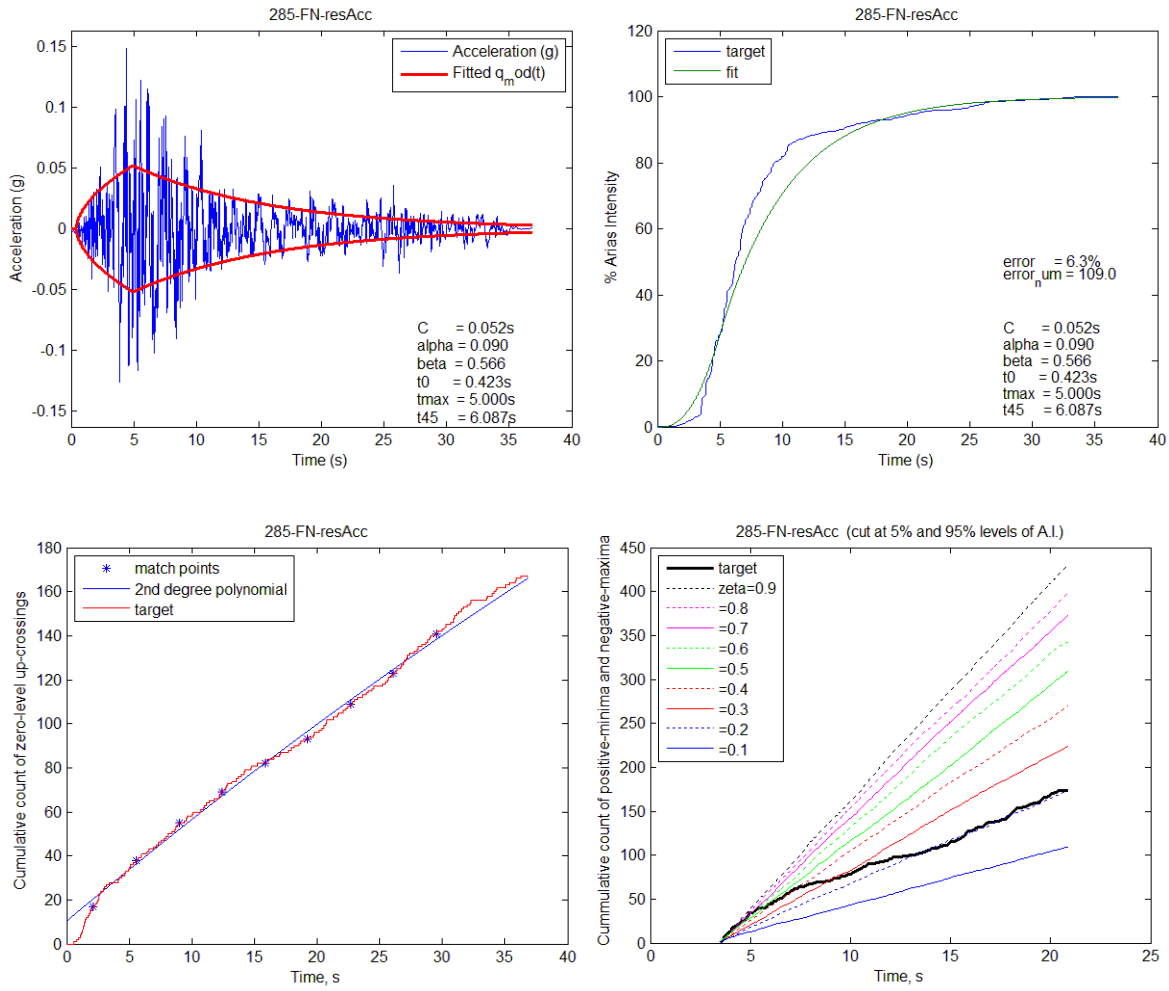

Figure 4.5: Fitting parameters of the residual model to the recorded residual motion for NGA record #285: (a) residual acceleration time history and fitted modulating function, (b) Husid plots of target residual acceleration and fitted modulating function; (c) target and fitted cumulative counts of zero-level up-crossings, and (d) target and fitted cumulative counts of positive minima and negative maxima

After identifying the pulse and residual parameters for the records in the database, a marginal probability distribution is fitted to the sample data of each parameter. As explained by Rezaeian and Der Kiureghian (2010), this is done to satisfy the normality assumption in the subsequent development of regression models. Note that when fitting the marginal distributions to the sample data, the sample values of $t_{max,p}$, t_{30} and $t_{max,r}$ are measured from t_0, which is set to zero for simulation purposes. The form of each distribution is selected by visual inspection of the corresponding histogram, and the distribution parameters are estimated by use of the maximum likelihood method. When applicable, the bounds of the distribution are selected based on the range of the observed data, also taking into consideration physical restrictions. All the fitted distributions are found to be not rejected at the 5% significance level by the

Kolmogorov-Smirnov test. The fitted distributions are summarized in Tables 4.3 and 4.4 for the parameters of the pulse and the residual, respectively. In Table 4.3, "t. exponential" stands for the exponential distribution truncated at both ends. The histograms of the model parameters are plotted in Figure 4.6 along with the fitted marginal distributions. As described below, these marginal distributions are used to transform the sample parameter values to the standard normal space. Figure 4.7 shows the QQ-plots of the transformed parameter data versus the standard normal quantiles. It is observed that in most cases the normality assumption is satisfied between the mean plus and minus two standard deviations of the distribution (the data follow a linear trend within the range -2 to $+2$).

Table 4.3: Marginal distributions of the parameters of the velocity pulse model

Parameter	Unit	Fitted Distribution	Lower bound	Upper bound	Mean	Standard Deviation
V_p	cm/s	lognormal	0.00	-	52.58	26.30
T_p	s	t. exponential	0.40	12.00	4.06	2.91
$\ln\gamma$	-	beta	0.67	1.50	0.87	0.12
ν/π	rad	uniform	0.00	2.00	1.00	0.58
$t_{max,p}$	s	t. exponential	1.00	42.00	10.00	7.95

Table 4.4: Marginal distributions of the parameters of the residual model

Parameter	Unit	Fitted Distribution	Lower bound	Upper bound	Mean	Standard Deviation
$I_a/\left(\frac{\pi}{2g}\right)$	g^2s	lognormal	0.00	-	0.11	0.12
D_{5-95}	s	beta	4.00	48.00	16.18	8.91
$\ln t_{30}$	ln(s)	beta	0.22	3.14	1.91	0.74
$\ln t_{max,r}$	ln(s)	beta	0.22	3.40	1.96	0.82
ω_{mid}	Hz	gamma	0.00	-	4.08	1.66
ω'	Hz/s	two-sided exponential	-1.10	0.60	-0.11	0.16
ζ_f	-	beta	0.02	1.00	0.39	0.22

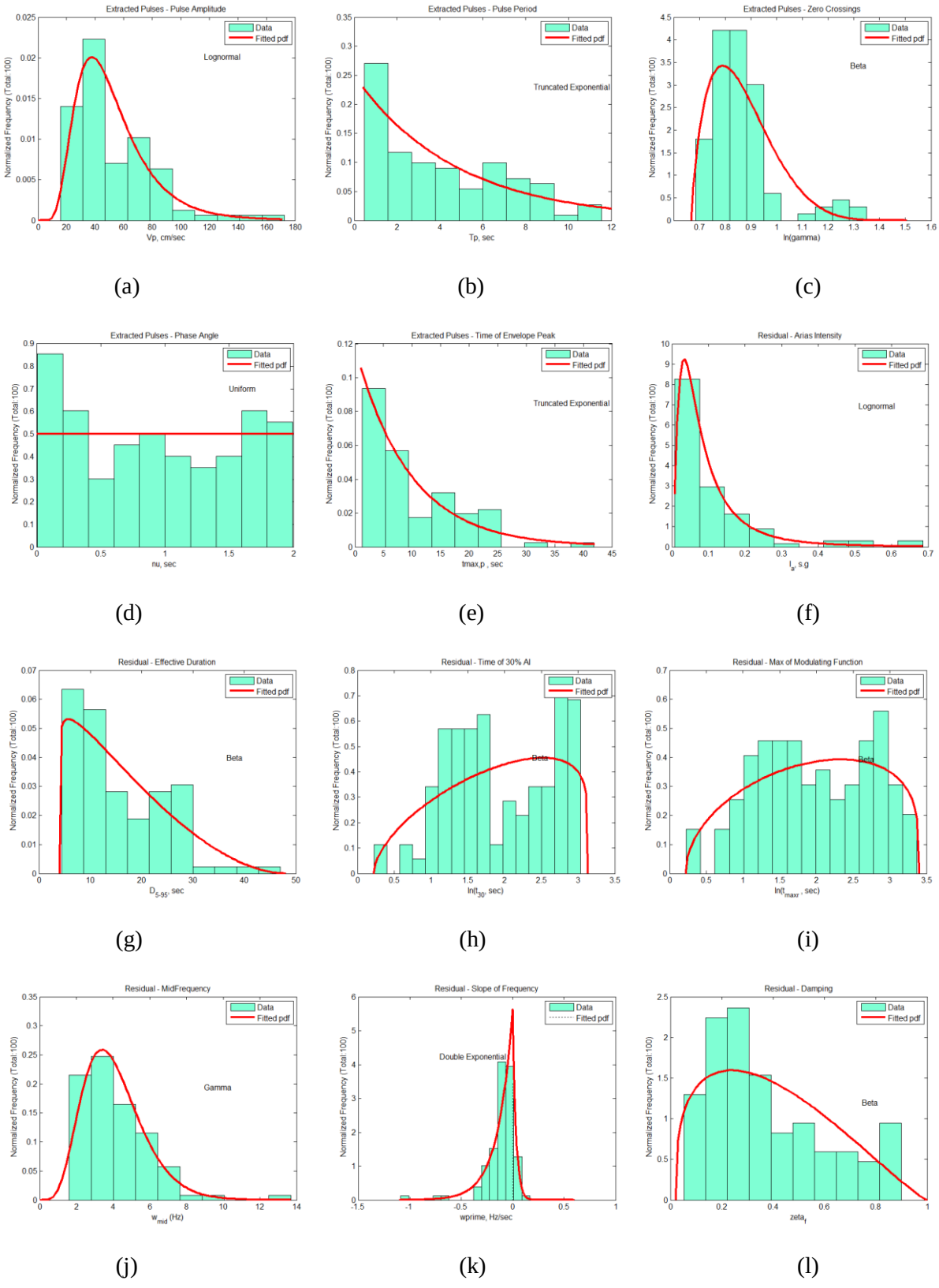

Figure 4.6: Histograms of model parameters with fitted marginal distributions: Pulse parameters (a) to (e), residual parameters (f) to (l)

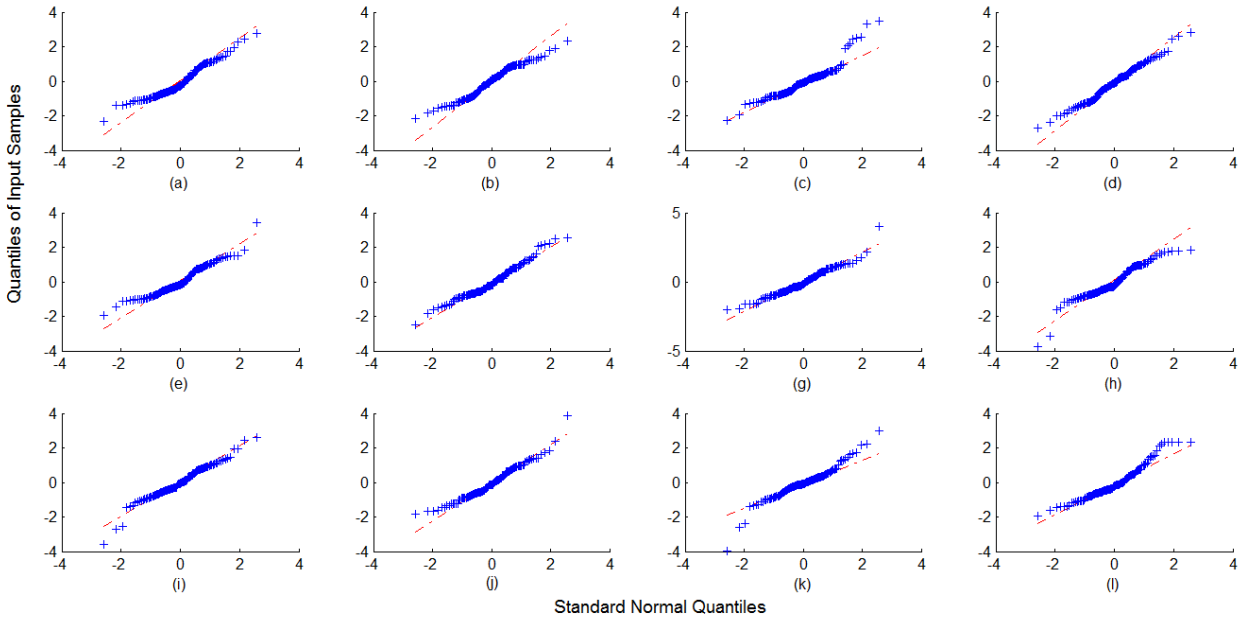

Figure 4.7: QQ-plots of transformed model parameters data: Pulse parameters (a) to (e), residual parameters (f) to (l)

4.4 PREDICTIVE EQUATIONS FOR MODEL PARAMETERS

Our aim is to generate synthetic ground motions for a specified design scenario. For this purpose, it is necessary to develop predictive equations for the model parameters in terms of earthquake and site characteristics that are normally available to the design engineer. We accomplish this by developing a regression formula for each model parameter in terms of explanatory variables defining the earthquake source and site characteristics. To satisfy the normality requirement of regression analysis, the data for each parameter is transformed to the standard normal space according to its marginal distribution before it is regressed against the earthquake and site characteristics. The selected explanatory variables can be classified into three categories: earthquake source characteristics, site characteristics, and parameters describing the source to site geometry. The earthquake source characteristics are the type of faulting, F, taken equal to 1 for strike-slip and 0 for non-strike-slip earthquakes (mostly reverse-oblique earthquakes), and the moment magnitude M_w of the earthquake. The site characteristics are represented by the shear-wave velocity in the top 30m of the soil at the site, V_{s30} (in meters per second). The source to site geometry is described by the closest distance to the fault rupture, R (in kilometers), and two directivity parameters that are only considered in the predictive relations for the pulse parameters (see Iervolino and Cornell, 2008, and Shahi and Baker, 2011). The directivity parameters are s and θ for strike-slip faulting, where s is the length of the fault rupturing towards the site (in kilometers) and θ is the angle between the

site-to-epicenter direction and the direction of the fault rupture (in degrees). For dip-slip faulting, the parameters are d and ϕ, where d is the width of the fault rupturing towards the site (in kilometers) and ϕ is the angle in a vertical plane between the fault rupture plane and the direction between the hypocenter and the site. We also use d and ϕ for all other non strike-slip faulting cases. Only variables having significant explanatory power are retained in the predictive equations. These were identified as those having coefficients with only positive or only negative 95% confidence intervals, and those with confidence intervals strongly skewed to either positive or negative direction. For NGA records 6960, 6966 and 6969, which were recorded during the 2010 Darfield New Zealand earthquake, V_{s30} was not documented. For these sites, the value of $V_{s30} = 274.5$m/s, which was recorded at other near-fault stations of this earthquake, is used.

Let α_i denote the ith parameter of the idealized model, $i = 1$ denoting V_p, $i = 2$ denoting T_p, $i = 3$ denoting γ , $i = 4$ denoting ν, $i = 5$ denoting $t_{max,p}$ (the pulse parameters), and $i = 6$ denoting $I_a/(\frac{2\pi}{g})$, $i = 7$ denoting D_{5-95}, $i = 8$ denoting t_{30}, $i = 9$ denoting $t_{max,r}$, $i = 10$ denoting ω_{mid}, $i = 11$ denoting ω', and $i = 12$ denoting ζ_f (the residual parameters). The marginal transformations

$$z_i = \Phi^{-1}\left[F_{\alpha_i}(\alpha_i)\right], \qquad i = 1, \cdots, 12 \tag{4.9}$$

where $F_X(x)$ denotes the cumulative distribution function of random variable X and $\Phi^{-1}[.]$ denotes the standard normal cumulative probability function, then define a set z_i of standard normal variables. Using this transformation, the data for each model parameter is transformed to data in the standard normal space. The latter data are then regressed against the variables defining the earthquake and site characteristics defined above.

After considering a number of predictive model forms, linear predictive relations of the form

$$z_i = \beta_{i,0} + \beta_{i,1}F + \beta_{i,2}M_w + \beta_{i,3}\ln R + \beta_{i,4}\ln V_{s30} + \beta_{i,5}\theta + \beta_{i,6}s + \epsilon_i \,, i = 1,2,3 \tag{4.10.a}$$

$$z_i = \beta_{i,0} + \beta_{i,1}F + \beta_{i,2}M_w + \beta_{i,3}R + \beta_{i,4}\ln V_{s30} + \epsilon_i \,, i = 5 \tag{4.10.b}$$

$$z_i = \beta_{i,0} + \beta_{i,1}F + \beta_{i,2}M_w + \beta_{i,3}\ln R + \beta_{i,4}\ln V_{s30} + \epsilon_i \,, i = 6 \tag{4.10.c}$$

$$z_i = \beta_{i,0} + \beta_{i,1}F + \beta_{i,2}M_w + \beta_{i,3}R + \beta_{i,4}V_{s30} + \epsilon_i \,, i = 7, \cdots, 12 \tag{4.10.d}$$

are used, where ε_i denotes the regression error, θ stands for both directivity angles θ and ϕ, and s stands for both rupture lengths s and d, since the distinction between the different faulting mechanisms is made through the variable F. No viable predictive relation was found for z_4, which corresponds to the pulse parameter ν. As more data becomes available, separate predictive relations can be developed for strike-slip and non-strike-slip cases. Moreover, because we are in the near-fault environment, we might be

dealing with very small distances R. Terms of the form $\ln(R + c_i)$ might need to be considered in the future instead of the $\ln R$ terms, in order to better represent such cases.

Table 4.5 lists the estimates of the regression coefficients along with the corresponding R^2 statistics and estimates of the variances of the regression errors for the pulse model parameters, except for z_4 (corresponding to ν), for which no predictive relation could be found. Table 4.6 lists the same for the parameters of the residual model. Tables 4.7 and 4.8 list the 95% confidence intervals of the two sets of model parameters, respectively. The regression analysis shows that V_p is weakly explained by M_w, $\ln R$, and θ; T_p is explained by F, M_w, $\ln V_{s30}$ and s; γ is weakly explained by M_w, $\ln R$ and $\ln V_{s30}$; and $t_{max,p}$ is explained by M_w, R and $\ln V_{s30}$. Furthermore, I_a is weakly explained by F, M_w, $\ln R$ and $\ln V_{s30}$. Of the remaining parameters of the residual model, D_{5-95} is explained by F, M_w, R and V_{s30}; t_{30} and $t_{max,r}$ are explained by M_w, R and V_{s30}; ω_{mid} is weakly explained by M_w and V_{s30}; and ω' and ζ_f are weakly explained by M_w, R and V_{s30}.

Table 4.5: Estimates of regression coefficients and error variances for pulse model parameters (z_1 to z_5)

i	α_i	$\beta_{i,0}$	$\beta_{i,1}$	$\beta_{i,2}$	$\beta_{i,3}$	$\beta_{i,4}$	$\beta_{i,5}$	$\beta_{i,6}$	R^2	σ^2
1	V_p	−1.22	-	0.28	−0.48	-	0.01	-	0.28	0.74
2	T_p	−6.81	0.13	1.28	-	−0.38	-	0.02	0.71	0.29
3	γ	−1.99	-	0.44	0.20	−0.23	-	-	0.14	0.89
4	ν/π	-	-	-	-	-	-	-	-	1.27
5	$t_{max,p}$	−5.64	-	1.05	0.04	−0.32	-	-	0.71	0.25

Table 4.6: Estimates of regression coefficients and error variances for residual model parameters (z_6 to z_{12})

i	α_i	$\beta_{i,0}$	$\beta_{i,1}$	$\beta_{i,2}$	$\beta_{i,3}$	$\beta_{i,4}$	$\beta_{i,5}$	$\beta_{i,6}$	R^2	σ^2
6	$I_a/\left(\frac{\pi}{2g}\right)$	−3.04	−0.16	0.30	−0.36	**0.29**	-	-	0.24	0.80
7	D_{5-95}	−7.86	**0.09**	1.12	4.2E-02	−6.0E-04	-	-	0.62	0.39
8	t_{30}	−8.38	-	1.20	3.6E-02	−4.0E-04	-	-	0.66	0.36
9	$t_{max,r}$	−8.27	-	1.18	3.4E-02	−3.0E-04	-	-	0.62	0.40
10	ω_{mid}	3.27	-	−0.51	-	4.0E-04	-	-	0.11	0.92
11	ω ’	−4.01	-	0.57	**−1.3E-02**	**5.0E-04**	-	-	0.16	0.82
12	ζ_f	0.89	-	**−0.14**	−1.7E-02	5.0E-04	-	-	0.05	0.98

Table 4.7: 95% confidence intervals of regression coefficients for pulse model parameters (z_1 to z_5)

i	α_i		$\beta_{i,1}$	$\beta_{i,2}$	$\beta_{i,3}$	$\beta_{i,4}$	$\beta_{i,5}$	$\beta_{i,6}$
1	V_p	LB	-	0.00	−0.64	-	0.00	-
		UB	-	0.57	−0.32	-	0.02	-
2	T_p	LB	−0.20	1.04	-	−0.63	-	0.00
		UB	0.45	1.51	-	−0.13	-	0.03
3	γ	LB	-	0.13	0.03	−0.63	-	-
		UB	-	0.75	0.37	0.17	-	-
4	ν/π	LB	-	-	-	-	-	-
		UB	-	-	-	-	-	-
5	$t_{max,p}$	LB	-	0.88	0.03	−0.53	-	-
		UB	-	1.21	0.06	−0.10	-	-

Table 4.8: 95% confidence intervals of regression coefficients for residual model parameters (z_6 to z_{12})

i	α_i		$\beta_{i,1}$	$\beta_{i,2}$	$\beta_{i,3}$	$\beta_{i,4}$	$\beta_{i,5}$	$\beta_{i,6}$
6	$I_a/\left(\frac{\pi}{2g}\right)$	LB	−0.62	−0.03	−0.53	−0.13	-	-
		UB	0.29	0.63	−0.19	0.70	-	-
7	D_{5-95}	LB	−0.22	0.89	0.025	−0.0011	-	-
		UB	0.40	1.36	0.059	−0.0002	-	-
8	t_{30}	LB	-	1.00	0.021	−0.0008	-	-
		UB	-	1.40	0.052	0.0001	-	-
9	$t_{max,r}$	LB	-	0.98	0.017	−0.0007	-	-
		UB	-	1.39	0.050	0.0002	-	-
10	ω_{mid}	LB	-	−0.82	-	−0.0002	-	-
		UB	-	−0.19	-	0.0011	-	-
11	ω'	LB	-	0.27	−0.036	−0.0002	-	-
		UB	-	0.87	0.011	0.0011	-	-
12	ζ_f	LB	-	−0.47	−0.043	−0.0002	-	-
		UB	-	0.18	0.009	0.0012	-	-

The amplitude of the forward directivity pulse is expected to be positively related to the magnitude and to the length of the rupture (or its width, in the case of dip-slip faulting) between the epicenter and the site, and inversely related to the closest distance to the fault and to the angle between the fault rupture and the site. The results of the regression analysis show that V_p is indeed positively related to M_w and inversely related to R, as the sign of the coefficient $\beta_{1,2}$ is positive and that of $\beta_{1,3}$ is negative. Similar trends were documented in previous findings (Bray and Rodriguez-Marek, 2004, Fu and Menun, 2004). However, the regression analysis shows that V_p is positively related to θ, as the sign of the coefficient $\beta_{1,4}$ is positive, and no significant dependence of the pulse amplitude on the length or width of the rupture is found. It is possible that variables M_w, R and θ provide the requisite information. Also, we

would have expected the soil stiffness to be significant in predicting V_p; this is not borne out with the present data. The pulse period T_p tends to increase with the magnitude and decrease with site stiffness, which is as expected and agrees with previous observations, even though T_p is not uniquely defined in the literature (Sommerville, 1998; Mavroieidis and Papageorgiou, 2003, Bray and Rodriguez-Marek, 2004; Fu and Menun, 2004; Baker, 2007). It appears that strike-slip earthquakes result in pulses with periods longer than those with reverse earthquakes (the majority of the non-strike-slip earthquakes in our database). Moreover, as s increases, T_p tends to increase, which is as expected since wave periods tend to lengthen with distance. The oscillatory characteristic parameter γ tends to increase with the magnitude and distance and to decrease with soil stiffness. Finally, $t_{max,p}$, which defines the time position of the pulse within the record, tends to increase with the magnitude and distance and to decrease with the soil stiffness. These trends are as expected.

For the residual model parameters, the trends with magnitude, distance and site stiffness make sense overall. The Arias intensity tends to increase with magnitude and to decrease with distance, and it tends to be larger for reverse earthquakes than for strike-slip earthquakes. These trends are as expected. However, the regression results indicate that Arias intensity of the residual motion increases with increasing site stiffness, which is contrary to what was observed by Rezaeian and Der Kiureghian (2010) for far-field motions. This might be due to nonlinearity of softer soils at strong levels of ground shaking that occur at the short distances considered. It is also important to keep in mind that this result is for the Arias intensity of the residual motion only, not that of the total ground motion. The time and duration parameters D_{5-95}, t_{30} and $t_{max,r}$ increase with magnitude and distance and decrease with site stiffness. The predominant frequency at the middle of ground shaking decreases with magnitude and increases with site stiffness. The rate of change of predominant frequency increases with magnitude and with site stiffness, and decreases with distance. Finally, the filter damping, which is a measure of the bandwidth of the residual ground motion, decreases with magnitude and distance and increases with site stiffness. Several of the trends for the filter parameters vary from those documented in Rezaeian and Der Kiureghian (2010) for far-field motions. These are highlighted with bold fonts in Table 4.6.

The correlations between the parameters z_i, $i = 1, \dots, 12$, are estimated as the correlations between the corresponding regression residuals ε_i, $i = 1, \dots, 12$, where $\varepsilon_4 = z_4$, since no predictive relation is found for this parameter. Table 4.9 lists the estimated correlation coefficients. We find strong negative correlation (-0.4) between z_1 and z_2, which correspond to the velocity pulse amplitude V_p and the velocity pulse period T_p. This is consistent with the inverse relation between the amplitude and duration factors found by Somerville et al. (1997). As expected, we find strong positive correlation (0.5) between the velocity pulse amplitude V_p and the Arias intensity of the residual, I_a. A pulselike motion

with a large pulse amplitude tends to have a high intensity residual. We also find strong positive correlation of the pulse period T_p with the time of the peak of the velocity pulse envelope $t_{max,p}$ (0.5) and with the time of the peak of the modulating function of the residual $t_{max,r}$ (0.4). The time and duration parameters $t_{max,p}$, D_{5-95}, t_{30} and $t_{max,r}$ are all positively correlated with each other, as expected. There is strong positive correlation of the time of the peak of the velocity pulse envelope $t_{max,p}$ with the effective duration D_{5-95} (0.4), with the time of the 30% Arias intensity of the residual motion t_{30} (0.7), and with the time of the peak of the modulating function of the residual $t_{max,r}$ (0.5). There is mild positive correlation (0.3) between D_{5-95} and t_{30}. Finally, t_{30} and $t_{max,r}$ are very strongly positively correlated (0.9). Concerning the filter parameters of the residual model, a mild negative correlation (-0.3) is found between the frequency at the middle of ground shaking, ω_{mid}, and the rate of change of frequency ω'. Practically no correlation is found between the frequency contents of the pulse and of the residual, namely between T_p and ω_{mid}.

Table 4.9: Estimated correlation matrix of regression errors

	z_1	z_2	z_3	z_4	z_5	z_6	z_7	z_8	z_9	z_{10}	z_{11}	z_{12}
	V_p	T_p	γ	ν/π	$t_{max,p}$	$I_a/\left(\frac{\pi}{2g}\right)$	D_{5-95}	t_{30}	$t_{max,r}$	ω_{mid}	ω'	ζ_f
z_1	1	−0.4	0.1	0.0	−0.1	0.5	−0.2	−0.1	−0.1	−0.3	0.1	0.4
z_2		1	0.1	−0.1	0.5	−0.2	0.2	0.4	0.4	−0.1	0.1	−0.2
z_3			1	−0.3	0.3	0.2	0.3	0.1	0.1	−0.1	0.1	0.1
z_4				1	0.0	0.1	0.0	0.0	0.1	0.1	0.0	0.0
z_5					1	−0.2	0.4	0.7	0.5	−0.1	−0.1	0.0
z_6						1	0.1	−0.1	−0.2	0.1	0.1	0.0
z_7							1	0.3	0.1	0.1	−0.1	0.1
z_8								1	0.9	0.0	0.1	0.0
z_9			Symmetric						1	−0.1	0.1	0.0
z_{10}										1	−0.3	−0.1
z_{11}											1	0.1
z_{12}												1

4.5 ALTERNATIVE MODEL OF PULSE AMPLITUDE

In the above, we used a model formulated in terms of the five parameters $(V_p, T_p, \gamma, \nu, t_{max,p})$ to describe the extracted velocity pulse. When regressing the transformed model parameters against earthquake and site characteristics, we obtained an R^2 value of only 0.28, and a large variance of 0.74 for the parameter z_1 describing the amplitude of the velocity pulse V_p. Here we consider an alternative model for the pulse amplitude.

Since the velocity pulse model is defined by an analytical expression, we can differentiate it to obtain an expression for the acceleration time history of the pulse. Let A_p be the amplitude of the pulse acceleration time history. For the mMP pulse model, one can show that A_p is approximately given by

$$A_p = \frac{2\pi}{T_p} V_p \tag{4.11}$$

Next, we compute A_p according to (4.11) for all the fitted pulses and fit a lognormal distribution to the sample data. The distribution is then used to transform the data to the standard normal space z_{A_p}. The adequacy of the fit is demonstrated in Figure 4.8, which compares the fitted marginal distribution to the histogram of the sample A_p data and the QQ-plot showing that the transformed z_{A_p} data is approximately normal. The transformed z_{A_p} data is then regressed against the earthquake and site characteristics, using a regression equation of the same form as that used for z_1, the transformed velocity pulse amplitude. The result is

$$z_{A_p} = \beta_{A_p,0} + \beta_{A_p,1} F + \beta_{A_p,2} M_w + \beta_{A_p,3} \ln R + \beta_{A_p,4} \ln V_{s30} + \beta_{A_p,5} \theta + \beta_{A_p,6} s + \epsilon_{A_p} \tag{4.12}$$

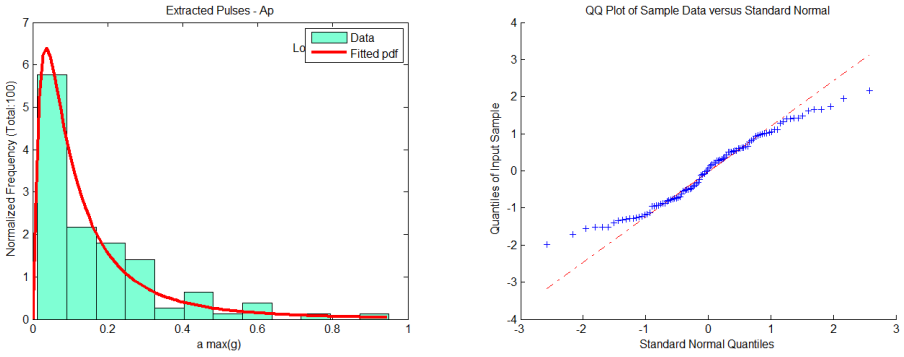

Figure 4.8: Histogram of the sample data for A_p and fitted lognormal distribution (Left), and QQ-plot of the transformed sample data (Right)

The estimated regression coefficients and their 95% confidence intervals are listed in Table 4.10. The regression results indicate that A_p is explained by F, M_w, $\ln R$, $\ln V_{s30}$ and s. It tends to be smaller for strike-slip earthquakes than for reverse earthquakes and it decreases with distance as expected. However, contrary to what one would expect, A_p tends to decrease with magnitude and with the length/width of rupture between the hypocenter and the site, and it increases with site stiffness. This is probably due to the fact that A_p is inversely proportional to the pulse period T_p, which increases with magnitude and with the length/width of the rupture between the hypocenter and the site, and decreases with site stiffness. The R^2 value of 0.53 is larger than that for z_1, and the variance of 0.50 is smaller than that for z_1, indicating that A_p is better explained by the earthquake and site characteristics than V_p. Thus, one possible improvement of the model is to define it in terms of the five parameters $(A_p, T_p, \gamma, \nu, t_{max,p})$, and to back-calculate V_p using

$$V_p = \frac{A_p T_p}{2\pi} \tag{4.13}$$

Table 4.10: Regression coefficients and 95% confidence intervals for z_{Ap}

	$\beta_{A_{p,0}}$	$\beta_{A_{p,1}}$	$\beta_{A_{p,2}}$	$\beta_{A_{p,3}}$	$\beta_{A_{p,4}}$	$\beta_{A_{p,5}}$	$\beta_{A_{p,6}}$	R^2	σ^2
A_p	6.41	-0.32	-1.07	-0.25	0.29	-	-0.01	0.53	0.50
LB	3.22	-0.76	-1.38	-0.38	-0.04	-	-0.03	-	-
UB	9.59	0.12	-0.76	-0.11	0.62	-	0.00	-	-

The above alternative model is not further pursued at this time. However, we intend to consider this model as well as other alternative models for possible improvement of the predictive equations in the future course of this study.

4.6 NON-PULSELIKE MOTIONS: MODEL PARAMETERS AND PREDICTIVE EQUATIONS

The model for non-pulselike motions is similar to that used for the residual motion, i.e., the modulated, filtered white-noise process with time varying filter parameters developed by Rezaeian and Der Kiureghian (2008, 2010) with the modified modulating function described in Eq. 3.7. Its seven parameters are identified by fitting the model to SN components of non-pulselike near-fault accelerograms. The procedure is similar to that reported above for the residuals of pulselike ground motions. After identifying

the model parameters for the records in the database, a marginal probability distribution should be fitted to the sample data of each parameter. As described earlier, this is done to satisfy the normality assumption of the subsequent regression analysis. This analysis has not been performed yet. For now, it is assumed that non-pulselike near-fault ground motions are similar to the residuals of pulselike near-fault ground motions in terms of their statistical characteristics. Identical marginal probability distributions, predictive equations and correlation matrix of regression errors are assumed. A more detailed analysis of non-pulselike motions will be performed in the next stage of this study.

4.7 PULSELIKE DATABASE

Table 4.11 below lists the 100 recorded ground motions that are used in this study and that are pulselike in the SN direction. It includes information about the earthquake name and year of occurrence, in addition to the name of the recording station. The earthquake and site characteristics used as explanatory variables in the regression analysis are also given, namely the type of faulting, F, the moment magnitude M_w, the closest distance to the fault rupture, R, the shear-wave velocity in the top 30m of the soil at the site, V_{s30}, and the two directivity parameters s and θ for strike-slip (or d and ϕ for dip-slip) faulting.

Table 4.11: Earthquake and site characteristics of the ground motions included in the pulselike database

NGA#	Earthquake Name	Year	Station Name	F	M_w	R (km)	V_{s30} (m/s)	θ or φ ($^\circ$)	s or d (km)
77	San Fernando	1971	Pacoima Dam (upper left abut)	0	6.6	1.8	2016	7.5	21.9
150	Coyote Lake	1979	Gilroy Array #6	1	5.7	3.1	663	17.0	4.1
159	Imperial Valley-06	1979	Agrarias	1	6.5	0.7	275	24.6	2.4
161	Imperial Valley-06	1979	Brawley Airport	1	6.5	10.4	209	10.5	38.1
170	Imperial Valley-06	1979	EC County Center FF	1	6.5	7.3	192	18.2	27.6
171	Imperial Valley-06	1979	El Centro - Meloland Geot. Array	1	6.5	0.1	265	5.4	19.4
173	Imperial Valley-06	1979	El Centro Array #10	1	6.5	6.2	203	17.5	25.1
178	Imperial Valley-06	1979	El Centro Array #3	1	6.5	12.9	163	23.2	26.3
179	Imperial Valley-06	1979	El Centro Array #4	1	6.5	7	209	11.5	26.6
180	Imperial Valley-06	1979	El Centro Array #5	1	6.5	4	206	4.7	27.7
181	Imperial Valley-06	1979	El Centro Array #6	1	6.5	1.4	203	0.8	27.5
182	Imperial Valley-06	1979	El Centro Array #7	1	6.5	0.6	211	4.8	27.5
184	Imperial Valley-06	1979	El Centro Differential Array	1	6.5	5.1	202	14.6	26.4
185	Imperial Valley-06	1979	Holtville Post Office	1	6.5	7.7	203	17.7	18.9
285	Irpinia, Italy-01	1980	Bagnoli Irpinio	0	6.9	8.2	1000	26.0	11.9
316	Westmorland	1981	Parachute Test Site	1	5.9	16.7	349	42.3	6.0
451	Morgan Hill	1984	Coyote Lake Dam (SW Abut)	1	6.2	0.5	597	0.4	24.6
459	Morgan Hill	1984	Gilroy Array #6	1	6.2	9.9	663	1.0	26.5
568	San Salvador	1986	Geotech Investig Center	1	5.8	6.3	545	12.1	6.0
611	Whittier Narrows-01	1987	Compton - Castlegate St	0	6.0	23.4	309	8.6	0.2
614	Whittier Narrows-01	1987	Downey - Birchdale	0	6.0	20.8	245	14.1	0.2
615	Whittier Narrows-01	1987	Downey - Co Maint Bldg	0	6.0	20.8	272	14.0	0.2
645	Whittier Narrows-01	1987	LB - Orange Ave	0	6.0	24.5	270	6.2	0.2
723	Superstition Hills-02	1987	Parachute Test Site	1	6.5	0.9	349	3.4	16.0
766	Loma Prieta	1989	Gilroy Array #2	0	6.9	11.1	271	16.2	14.5

NGA#	Earthquake Name	Year	Station Name	F	M_w	R (km)	V_{s30} (m/s)	θ or φ ($^\circ$)	s or d (km)
828	Cape Mendocino	1992	Petrolia	0	7.0	8.2	713	50.7	6.7
900	Landers	1992	Yermo Fire Station	1	7.3	23.6	354	17.2	65.8
982	Northridge-01	1994	Jensen Filter Plant	0	6.7	5.4	373	13.7	19.5
983	Northridge-01	1994	Jensen Filter Plant Generator	0	6.7	5.4	526	13.7	19.5
1045	Northridge-01	1994	Newhall - W Pico Canyon Rd.	0	6.7	5.5	286	11.0	19.5
1051	Northridge-01	1994	Pacoima Dam (upper left)	0	6.7	7	2016	1.5	19.5
1063	Northridge-01	1994	Rinaldi Receiving Sta	0	6.7	6.5	282	18.3	19.5
1085	Northridge-01	1994	Sylmar - Converter Sta East	0	6.7	5.2	371	12.2	19.5
1086	Northridge-01	1994	Sylmar - Olive View Med FF	0	6.7	5.3	441	6.3	19.5
1114	Kobe, Japan	1995	Port Island (0 m)	1	6.9	3.3	198	14.6	18.7
1120	Kobe, Japan	1995	Takatori	1	6.9	1.5	256	13.3	12.8
1161	Kocaeli, Turkey	1999	Gebze	1	7.5	10.9	792	23.9	46.6
1176	Kocaeli, Turkey	1999	Yarimca	1	7.5	4.8	297	13.9	19.2
1182	Chi-Chi, Taiwan	1999	CHY006	0	7.6	9.8	438	0.1	9.1
1244	Chi-Chi, Taiwan	1999	CHY101	0	7.6	10	259	4.3	11.4
1403	Chi-Chi, Taiwan	1999	NSY	0	7.6	13.2	600	11.9	14.9
1476	Chi-Chi, Taiwan	1999	TCU029	0	7.6	28.1	474	15.5	14.9
1480	Chi-Chi, Taiwan	1999	TCU036	0	7.6	19.8	273	15.9	14.9
1481	Chi-Chi, Taiwan	1999	TCU038	0	7.6	25.4	273	17.7	14.9
1482	Chi-Chi, Taiwan	1999	TCU039	0	7.6	19.9	541	12.3	14.9
1483	Chi-Chi, Taiwan	1999	TCU040	0	7.6	22.1	362	17.7	14.9
1486	Chi-Chi, Taiwan	1999	TCU046	0	7.6	16.7	466	5.4	14.8
1489	Chi-Chi, Taiwan	1999	TCU049	0	7.6	3.8	487	10.4	14.9
1491	Chi-Chi, Taiwan	1999	TCU051	0	7.6	7.7	273	12.6	14.9
1492	Chi-Chi, Taiwan	1999	TCU052	0	7.6	0.7	393	6.6	14.4
1493	Chi-Chi, Taiwan	1999	TCU053	0	7.6	6	455	12.3	14.9
1502	Chi-Chi, Taiwan	1999	TCU064	0	7.6	16.6	273	17.6	14.9

NGA#	Earthquake Name	Year	Station Name	F	M_w	R (km)	V_{s30} (m/s)	θ or φ ($^\circ$)	s or d (km)
1503	Chi-Chi, Taiwan	1999	TCU065	0	7.6	0.6	306	6.0	14.2
1505	Chi-Chi, Taiwan	1999	TCU068	0	7.6	0.3	487	7.0	14.7
1510	Chi-Chi, Taiwan	1999	TCU075	0	7.6	0.9	573	4.1	13.4
1511	Chi-Chi, Taiwan	1999	TCU076	0	7.6	2.8	615	0.1	11.8
1519	Chi-Chi, Taiwan	1999	TCU087	0	7.6	7	474	8.9	14.9
1528	Chi-Chi, Taiwan	1999	TCU101	0	7.6	2.1	273	10.8	14.9
1529	Chi-Chi, Taiwan	1999	TCU102	0	7.6	1.5	714	10.1	14.9
1530	Chi-Chi, Taiwan	1999	TCU103	0	7.6	6.1	494	12.7	14.9
1548	Chi-Chi, Taiwan	1999	TCU128	0	7.6	13.2	600	11.9	14.9
1550	Chi-Chi, Taiwan	1999	TCU136	0	7.6	8.3	474	14.7	14.9
1595	Chi-Chi, Taiwan	1999	WGK	0	7.6	10	259	4.3	11.4
1605	Duzce, Turkey	1999	Duzce	1	7.1	6.6	276	25.3	1.5
2457	Chi-Chi, Taiwan-03	1999	CHY024	0	6.2	19.6	428	7.4	6.5
2495	Chi-Chi, Taiwan-03	1999	CHY080	0	6.2	22.4	553	13.9	6.5
2627	Chi-Chi, Taiwan-03	1999	TCU076	0	6.2	14.7	615	13.7	6.5
2628	Chi-Chi, Taiwan-03	1999	TCU078	0	6.2	7.6	443	76.6	1.8
3473	Chi-Chi, Taiwan-06	1999	TCU078	0	6.3	11.5	443	14.8	12.0
3548	Loma Prieta	1989	Los Gatos - Lexington Dam	0	6.9	5	1070	5.3	14.5
4040	Bam, Iran	2003	Bam	1	6.6	1.7	487	2.7	12.6
4065	Parkfield-02, CA	2004	PARKFIELD - EADES	1	6.0	2.9	339	8.5	9.8
4098	Parkfield-02, CA	2004	Parkfield - Cholame 1E	1	6.0	3	339	5.0	10.0
4100	Parkfield-02, CA	2004	Parkfield - Cholame 2WA	1	6.0	3	185	3.1	10.0
4101	Parkfield-02, CA	2004	Parkfield - Cholame 3E	1	6.0	5.5	376	24.9	10.0
4102	Parkfield-02, CA	2004	Parkfield - Cholame 3W	1	6.0	3.6	339	7.2	10.0
4103	Parkfield-02, CA	2004	Parkfield - Cholame 4W	1	6.0	4.2	438	12.4	10.0
4107	Parkfield-02, CA	2004	Parkfield - Fault Zone 1	1	6.0	2.5	339	0.4	8.4
4113	Parkfield-02, CA	2004	Parkfield - Fault Zone 9	1	6.0	2.9	438	7.3	9.9

NGA#	Earthquake Name	Year	Station Name	F	M_w	R (km)	V_{s30} (m/s)	θ or φ ($^\circ$)	s or d (km)
4115	Parkfield-02, CA	2004	Parkfield - Fault Zone 12	1	6.0	2.6	339	5.1	11.0
4116	Parkfield-02, CA	2004	Parkfield - Stone Corral 4E	1	6.0	8.8	376	80.2	1.5
4126	Parkfield-02, CA	2004	PARKFIELD - STONE CORRAL 1E	1	6.0	3.8	371	24.3	6.5
4483	L'Aquila, Italy	2009	L'Aquila - Parking	0	6.3	5.4	717	35.2	7.6
4816	Wenchuan, China	2008	Mianzhuqingping	0	7.9	6.6	760	32.5	9.5
4874	Chuetsu-oki	2007	Oguni Nagaoka	0	6.8	20	407	58.6	12.2
4875	Chuetsu-oki	2007	Kariwa	0	6.8	12	214	84.2	1.2
4879	Chuetsu-oki	2007	Yan Sakuramachi City watershed	0	6.8	19	203	74.9	3.7
4896	Chuetsu-oki	2007	SERVICE HALL: 2.4 M DEPTH	0	6.8	11	310	88.9	0.2
5810	Iwate	2008	Machimukai Town	0	6.9	24.1	467	67.8	5.3
5832	El Mayor-Cucapah	2010	TAMAULIPAS	0	7.2	26.6	275	66.4	2.9
6877	Joshua Tree, CA	1992	Indio - Jackson Road	1	6.1	25.5	208	1.3	0.5
6887	Darfield, New Zealand	2010	CBGS	1	7.0	18.1	275	6.4	29.0
6927	Darfield, New Zealand	2010	LINC	1	7.0	7.1	275	6.9	29.0
6942	Darfield, New Zealand	2010	NNBS	1	7.0	26.8	275	8.5	29.0
6952	Darfield, New Zealand	2010	PPHS	1	7.0	18.7	275	11.5	29.0
6960	Darfield, New Zealand	2010	RHSC	1	7.0	13.6	275	6.8	29.0
6962	Darfield, New Zealand	2010	ROLC	1	7.0	1.5	275	0.1	26.9
6966	Darfield, New Zealand	2010	SHLC	1	7.0	22.3	275	8.7	29.0
6969	Darfield, New Zealand	2010	SMTC	1	7.0	20.9	275	14.7	29.0
6975	Darfield, New Zealand	2010	TPLC	1	7.0	6.1	275	6.6	29.0

5 Simulation of Near-Fault Ground Motions

5.1 INTRODUCTION

With the stochastic model of the SN component of near-fault ground motions formulated (Chapter 3) and predictive equations for its parameters developed (Chapter 4), it is now possible to simulate artificial near-fault ground motions that possess the physical and statistical characteristics of real near-fault ground motions, including the characteristics of the velocity pulse arising due to the directivity effect. In this chapter we consider two simulation approaches: (a) simulating near-fault ground motions that have the same model parameters as those identified for a recorded near-fault ground motion, and (b) simulating near-fault ground motions for specified earthquake source and site characteristics. The former are useful to examine how other realizations of the same event may have appeared. This approach is also useful for validating the simulation method by way of comparing various characteristics of the simulated motions with those of the recorded motion. The second approach is useful for design situations, where the specification is in terms of the characteristics of an earthquake source (type of faulting, location of hypocenter, magnitude, rupture dimensions) and a site (position relative to the fault rupture, shear-wave velocity). This approach produces near-fault ground motions that have the same natural variability that is present in a collection of recorded ground motions with the specified earthquake source and site characteristics.

In this chapter we simulate samples of SN components of near-fault ground motions using both methods. By comparing various characteristics of the simulated motions with those of recorded motions, we provide validation for the proposed models and the predictive equations of the model parameters.

5.2 SIMULATION BY USE OF FITTED MODEL PARAMETERS

Given the pulselike SN component of a recorded near-fault ground motion, we first extract the velocity pulse by use of the wavelet-based method by Baker (2007) and subtract its derivative from the acceleration record to obtained the residual motion. Next we identify the model parameters by use of the methods described in Section 3 of Chapter 4. Specifically, the modified Mavroeidis-Papageorgiou (mMP) pulse is fitted to the extracted velocity pulse and its five parameters $(V_p, T_p, \gamma, \nu, t_{max,p})$ are identified. Also, the modulated filtered white-noise model is fitted to the residual motion and its seven parameters

$(I_a, D_{5-95}, t_{30}, t_{max,r}, \omega_{mid},\ \omega', \zeta_f)$, or equivalently $(c, \alpha, \beta, t_{max,r}, \omega_{mid}, \omega', \zeta_f)$, are identified. An artificial motion is simulated by first generating a band-limited white-noise process (the upper frequency limit is determined by the choice of the time step Δt, see Rezaeian and Der Kiureghian, 2008) and using it in Eq. 3.5 along with the filter IRF and the modulating function with the identified parameters. This motion is then high-pass filtered (see Rezaeian and Der Kiureghian, 2008) to assure zero velocity and displacement at the end of the record. This constitutes the residual acceleration motion. The derivative of the identified mMP pulse is then added to obtain the total acceleration waveform. The resulting acceleration time history naturally has zero velocity and displacement values at the end of the record. This is because both the pulse and residual models possess these characteristics. It is noted that applying the high-pass filter to the sum of the simulated pulse and the simulated residual motion instead would have resulted in the undesirable loss of the characteristic large period velocity pulse. Integrations of the total acceleration motion yield the velocity and displacements time histories of the artificial ground motion. Note that the velocity pulse in each of the simulated motions is the same, as are the filter IRF and modulating function of the residual motion. However, the residual motion randomly varies from sample to sample due to the randomness in the underlying white-noise process. This is reasonable, since we are considering realizations of the same event. The variations due to the underlying white noise can be thought of as variations in the sequence of ruptures in the fault, while the overall rupture size and slip direction remain the same for all realizations – thus, a unique velocity pulse form but varying residuals.

5.2.1 Example application

As a first example, consider the NGA record #285, which was recorded at the Bagnoli Irpinio Station during the 1980 Irpinia earthquake in Italy. The acceleration, velocity and displacement time histories of this record were plotted in Figure 4.1. Furthermore, the acceleration time history of the velocity pulse extracted from this record, as well as that of the resulting residual motion were plotted in Figure 4.2. The fitted mMP velocity pulse and the modulating function for this record are those shown in Figures 4.3 and 4.5a, respectively. The identified pulse parameters and parameters of the fitted residual model for this record were listed in Tables 4.1 and 4.2, respectively. These are used as input parameters to our stochastic model, which is used to generate 20 artificial acceleration time histories, as described above. Figures 5.1 and 5.2 show details of one of these simulated motions. Figure 5.1 shows the derivative of the fitted velocity pulse according to the mMP model, the simulated residual acceleration, and the total acceleration time history. Comparing with Figure 4.2, we observe clear similarities between the features of the recorded and simulated motions. Figure 5.2 shows the acceleration, velocity and displacement time histories of the simulated ground motion. Again similarities can be observed when comparing this figure

with Figure 4.1 for the recorded motion, though peak velocity and displacement values are somewhat smaller for this simulated motion.

Figure 5.3 shows an overlay of the 20 simulated motions as thin grey lines together with the recorded motion in thick black line. The thin lines illustrate the range of possible realizations of acceleration time histories using the fitted model parameters. It can be seen that the general features of the simulated and recorded acceleration time histories are similar. Furthermore, the recorded motion is well within the range of the 20 simulated motions.

Elastic pseudo-acceleration response spectra at 5% damping are computed for the recorded and simulated ground motions. Figure 5.4 shows the spectrum for the recorded motion by a thick black line and the spectra of the simulated motions with thin grey lines. The geometric mean of the spectra of the simulated motions is shown by a thick grey line. One can observe that the response spectrum of the recorded motion falls within the range spanned by the spectra of the simulated motions at most periods. Moreover, the geometric mean spectrum of the simulated motions is comparable to the spectrum of the recorded motion at periods larger than about 1s. However, at periods below 1s, where the spectra are primarily influenced by the residual motions, the recorded and simulated spectra show significant differences. This is due to the idealized nature of our model for the residual. Obviously, with smooth models of the modulating function and the filter IRF, and with a small number of model parameters, it is not possible to capture all the details of the recorded ground motion. What is important is to capture the essential characteristics. In this case, given the pulselike nature of the motion, the long-period segment of the response spectrum is the important feature, and that is well captured by the model. The extracted and simulated velocity pulses have a period of $T_p = 1.55$s. A peak in the response spectra of both the recorded and simulated ground motions can be seen in Figure 5.4 at periods around 1.2s to 1.3s. This is due to the velocity pulse. The lower period of the peak is consistent with observations made by Somerville (2003) and Shahi and Baker (2011) regarding the characteristics of the response spectra of near-fault acceleration time histories. For example, Somerville (2003) suggested scaling up conventional response spectra by a cosine shaped function centered at $0.75T_p$ to account for a forward directivity pulse of period T_p. For the present case, this would correspond to a peak in the response spectrum at a period of 1.16s. Shahi and Baker (2011) computed the mean amplification in the pseudo-acceleration spectrum due to the presence of a pulse in the ground motion and found that it takes a maximum value at $0.88T_p$. For the present case, this would correspond to a peak in the response spectrum at a period of 1.36s. It is evident that the simulated pulselike motions are consistent with these findings.

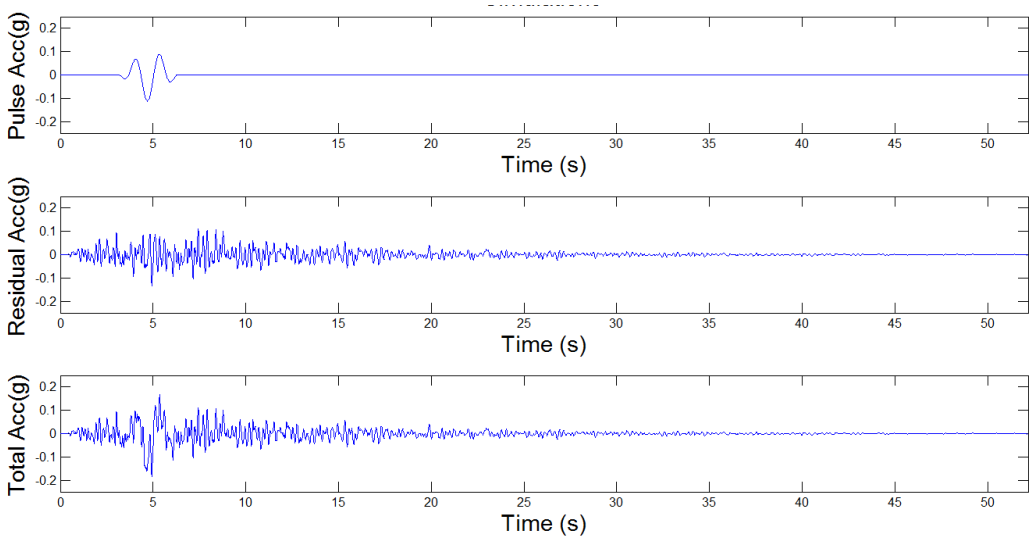

Figure 5.1: Simulated motion with parameters identified for NGA record #285: derivative of simulated velocity pulse (top), simulated residual motion (middle), and total simulated acceleration record (bottom)

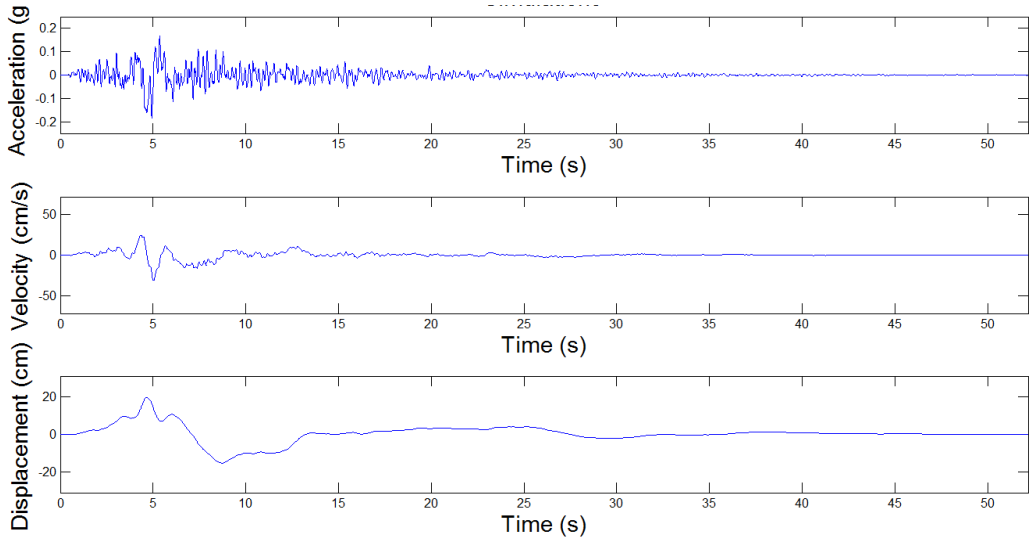

Figure 5.2: Simulated motion with parameters identified for NGA record #285: acceleration, velocity and displacement time histories

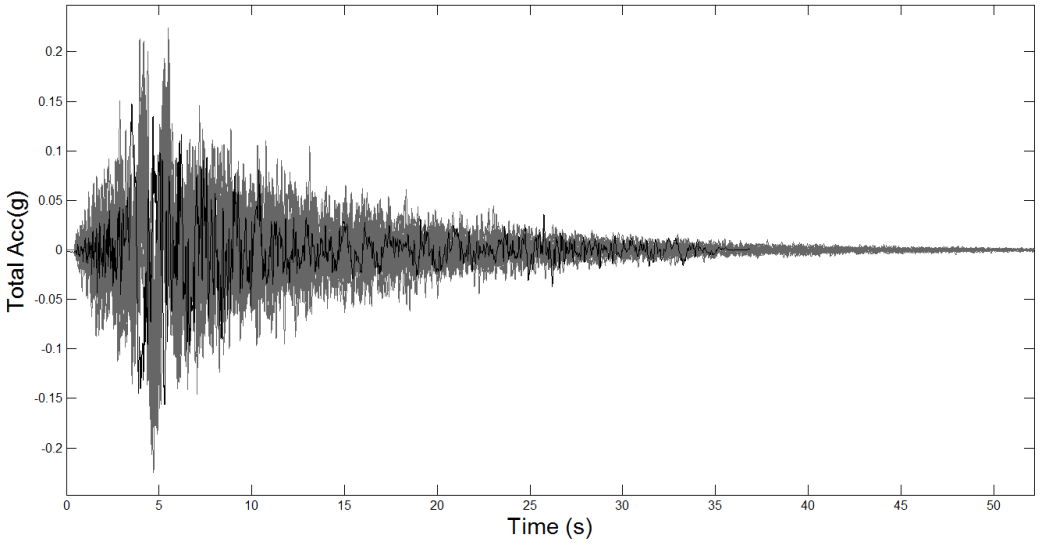

Figure 5.3: Acceleration time history of NGA record #285 (black thick line) and 20 simulated acceleration time histories using the fitted parameters

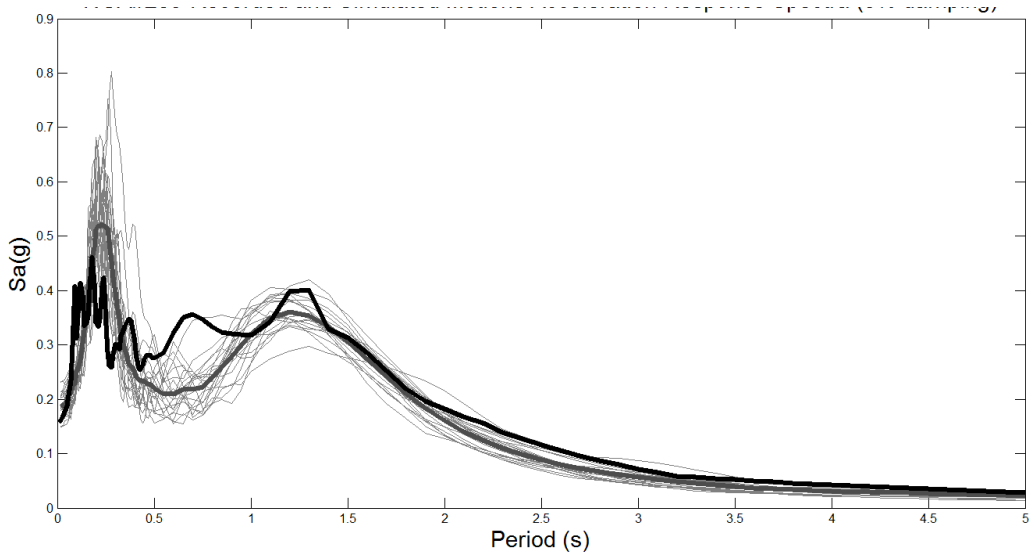

Figure 5.4: Pseudo-acceleration response spectra at 5% damping of the NGA record #285 (black thick line), of 20 simulated ground motions using the fitted parameters (grey lines), and of their geometric mean (thick grey line)

5.3 SIMULATION OF NEAR-FAULT GROUND MOTIONS FOR SPECIFIED EARTHQUAKE SOURCE AND SITE CHARACTERISTICS

To simulate a SN component of pulselike near-fault ground motion for a given set of earthquake source and site characteristics, we proceed as follows: Given the set of earthquake and site characteristic variables $F, M_w, R, V_{s30}, \theta$ and s, we first compute the conditional mean values of the transformed model parameters $z_1, \dots, z_{12}$, except for z_4, by use of the predictive equations presented in Eqs. 4.10, while neglecting the error terms. We set the mean value of z_4 to zero. We then add to these mean values simulated values of the corresponding error terms ϵ_i, $i = 1, \dots, 12$, generated as correlated normal random variables with zero means and variances and correlation coefficients as listed in Tables 4.3, 4.4 and 4.7. Note that z_4 has a sample variance of 1.27. The generated z_i values are then transformed back to the original space according to the inverse of the relations in Eq. 4.9. The pulse velocity waveform is computed according to Eq. 3.4 using the generated pulse parameters $(V_p, T_p, \gamma, \nu, t_{max,p})$. The generated residual parameters $(I_a, D_{5-95}, t_{30}, t_{max,r})$ are used in Eqs. 4.5, 4.6 and 4.8 to back-calculate the modulating function parameters $(c, \alpha, \beta, t_{max,r})$. These are used in Eq. 3.7 to compute the modulating function. The generated residual parameters $(\omega_{mid}, \omega', \zeta_f)$ define the filter as given in Eqs. 3.8 and 3.9. The modulating function and the filter are then used in Eq. 3.5, together with a simulated band-limited white-noise process, to generate a motion, which after high-pass filtering, constitutes a sample of the residual motion. Adding the derivative of the generated velocity pulse to the generated residual acceleration, the total acceleration record is obtained. This procedure, beginning with the generation of new parameter values, is repeated to generate as many near-fault synthetic ground motions for the specified earthquake source and site characteristics as is necessary for the given design scenario.

The set of near-fault SN component ground motions simulated by the above approach possess the variability inherent in recorded ground motions for the specified earthquake source and site characteristics. This is because the model is fitted to the database of recorded ground motions from different earthquakes. Thus, for the same earthquake source and site characteristics, we will have simulated motions that will have large, medium or small velocity pulses with a range of periods, and residuals that will have a variety of intensities, frequency contents and durations. These should be viewed as ground motions resulting from different earthquakes that happen to have common source and site characteristics. If we use the earthquake source and site characteristics of a particular record to generate artificial records, the recorded motion can then be seen as one realization arising from these earthquakes with common source and site characteristics. Since in the design or risk assessment stage one only has information about the general characteristics of the earthquake source and the site, the simulated near-

fault ground motions obtained by this approach would be the proper set for design or risk assessment considerations.

5.3.1 Example application

To illustrate the proposed procedure, we simulate five FN acceleration time histories with forward directivity pulses for the set of earthquake source and site characteristics $F = 0$, $M_w = 6.9$, $R = 8.2$km, $V_{s30} = 1000$m/s, $\theta = 26^o$, and $s = 11.89$km. These values correspond to the NGA record #285, recorded at the Bagnoli Irpinio Station during the 1980 Irpinia earthquake in Italy, which is the same record considered in Section 2.1 of this Chapter as well as in Chapter 4.

Table 5.1 lists the parameters of the mMP pulse model fitted to the velocity pulse extracted from the recorded ground motion (see Figure 4.1 for a plot of this pulse) along with those of the simulated mMP pulses. The entry $T_{p,\text{wavelet}}$ is described below. The first row of the table shows the median values of the pulse parameters, which are obtained by back transforming the predicted mean values of the standard normal variables $z_1, \ldots, z_5$. The second row lists the identified parameters of the recorded motion, and the remaining rows show the generated parameter values of the five synthetic pulses. Plots of the synthetic pulses are shown in Figures 5.5-5.9 as black solid lines. The recorded velocity pulse has an amplitude and a period that are significantly smaller than the corresponding median values computed using the predictive equations (peak velocity of 27.1cm/s versus 46.5cm/s and period of 1.55s versus 2.19s, respectively). Thus, based on the available data set of SN near-fault recorded ground motions, this particular recorded motion has a smaller pulse amplitude and a smaller pulse period than would be expected, on the average, from such an earthquake. The simulated velocity pulses have amplitudes ranging from 25.70cm/s to 68.30cm/s, thus bracketing the predicted median value of 46.53cm/s. Their periods range from 1.09s to 3.84s, bracketing the predicted median value of 2.19s. Simulated values for the other parameters, γ, ν and $t_{max,p}$, also show significant variabilities around their respective predicted median values. As mentioned earlier, these variabilities reflect the randomness that is inherent in the directivity pulses of near-fault ground motions for a given set of earthquake source and site characteristics.

Table 5.1: Parameters of the recorded and simulated pulses for prescribed earthquake source and site characteristics

	V_p	T_p	γ	ν/π	$t_{max,p}$	$T_{p,\text{wavelet}}$
	cm/s	s		rad	s	s
Median	46.5	2.19	2.29	1.00	5.90	
Recorded	27.1	1.55	2.13	0.66	4.28	1.71
Simulation 1	39.3	2.02	2.39	0.03	4.39	2.40
Simulation 2	54.2	1.13	2.07	1.98	5.25	6.46
Simulation 3	68.3	1.09	2.51	0.48	5.44	1.15
Simulation 4	44.1	2.10	2.84	1.41	5.43	2.76
Simulation 5	25.7	3.84	2.82	0.55	8.81	3.85

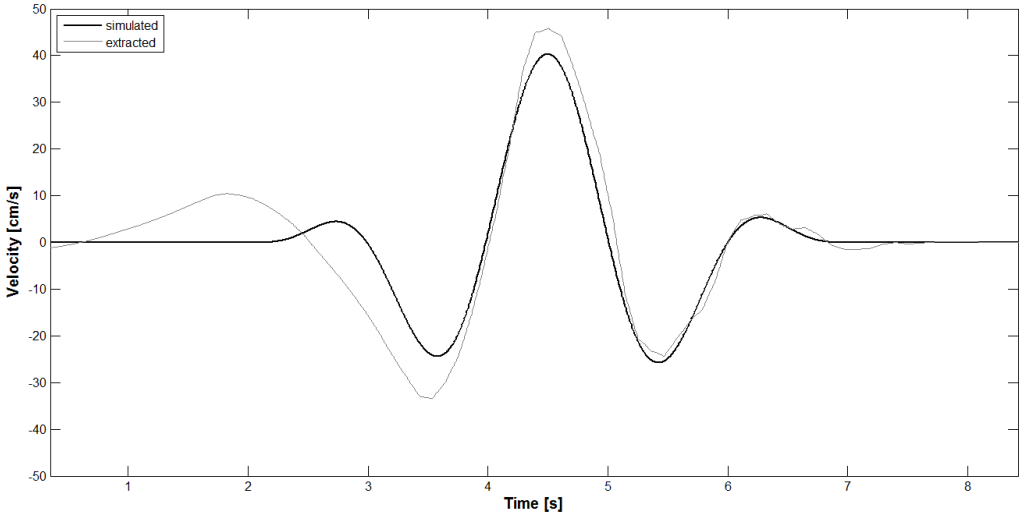

Figure 5.5: Simulated mMP velocity pulse #1 (black line) and extracted pulse from total simulated motion #1 (grey line)

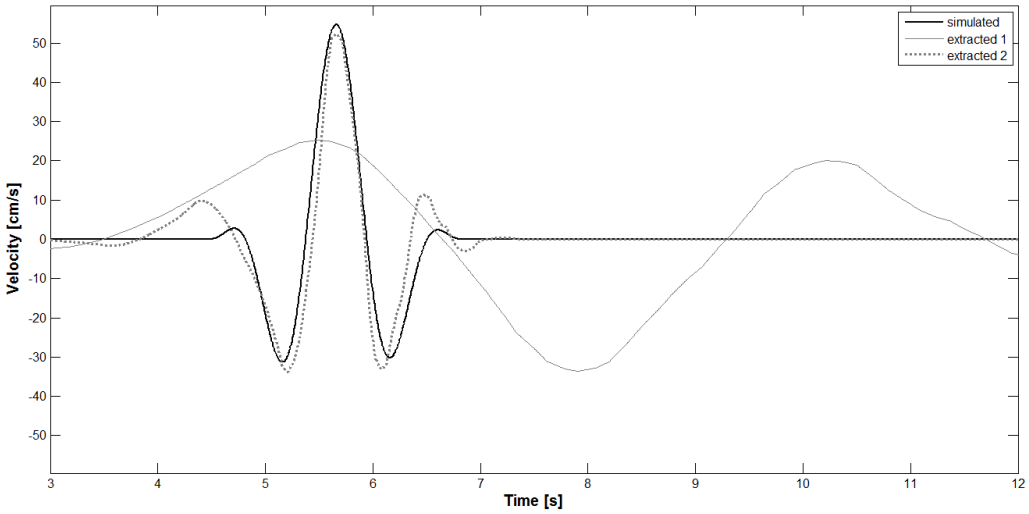

Figure 5.6: Simulated mMP velocity pulse #2 (black line) and two extracted pulses from total simulated motion #2 (grey lines)

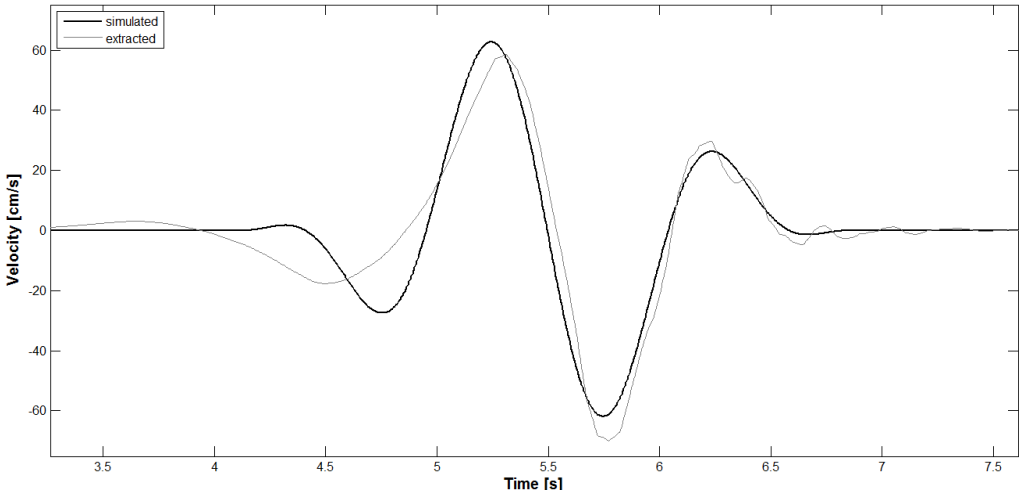

Figure 5.7: Simulated mMP velocity pulse #3 (black line) and extracted pulse from total simulated motion #3 (grey line)

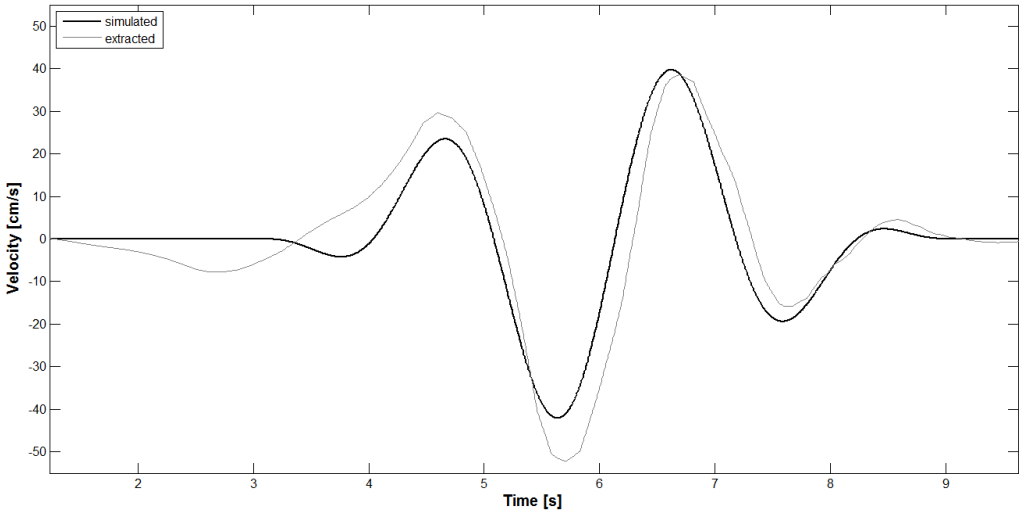

Figure 5.8: Simulated mMP velocity pulse #4 (black line) and extracted pulse from total simulated motion #4 (grey line)

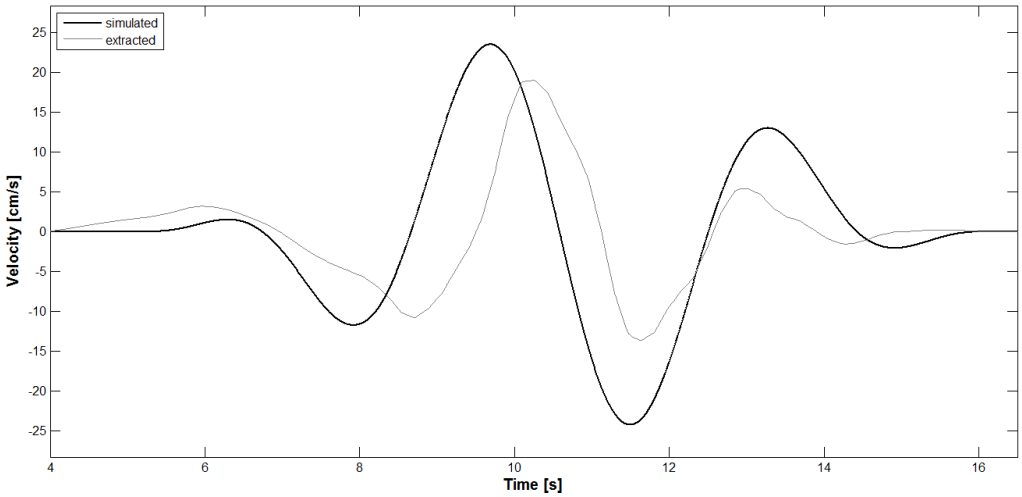

Figure 5.9: Simulated mMP velocity pulse #5 (black line) and extracted pulse from total simulated motion #5 (grey line)

Table 5.2 lists the parameters of the residual parts of the recorded and simulated motions. The first row lists the predicted median values, which are obtained by back transforming the predicted mean values of the standard normal variables $z_6, \ldots, z_{12}$. The second row lists the identified parameters of the recorded residual motion, and the remaining rows show the generated parameter values of the five synthetic residual motions. As can be observed, the recorded residual has a scaled Arias intensity of $I_a/(\frac{2g}{\pi}) = 0.0209g^2$s, an effective duration of 17.4s, and a predominant frequency of 4.58Hz at the middle of the strong shaking of the residual motion. These are respectively much smaller, much longer

and slightly larger than the corresponding median values ($0.0930g^2$s, 11.1s and 4.13Hz) computed using the predictive equations. Thus, the residual motion of this particular record has a much lower intensity and a much longer effective duration than would be expected, on the average, from a ground motion generated by an earthquake of the given source and site characteristics, while its predominant frequency is slightly above average. The simulated residuals have scaled Arias intensities ranging from $0.0575g^2$s to $0.234g^2$s, effective durations ranging from 7.37s to 14.6s, and predominant frequencies ranging from 2.52Hz to 5.34Hz. These all bracket the predicted median values. Simulated values of the other parameters, t_{30}, $t_{max,r}$, ω' and ζ_f, also show significant variabilities around their respective predicted median values. As mentioned earlier, these variabilities reflect the randomness that is inherent in the residuals of near-fault ground motions for a given set of earthquake source and site characteristics.

Table 5.2: Parameters of the recorded and simulated residuals for prescribed earthquake source and site characteristics

	$I_a/(\frac{\pi}{2g})$	D_{5-95}	t_{30}	$t_{max,r}$	ω_{mid}	ω'	ζ_f
	g^2s	s	s	s	Hz	Hz/s	
Median	0.0930	11.1	6.01	6.44	4.13	-4.05E-02	0.443
Recorded	0.0209	17.4	4.75	4.58	4.58	-2.87E-02	0.230
Simulation1	0.0753	14.0	6.27	6.80	5.34	-9.46E-02	0.786
Simulation2	0.234	7.37	2.79	2.97	2.52	-4.85E-02	0.139
Simulation3	0.0622	11.0	4.35	6.29	3.64	-9.84E-02	0.846
Simulation4	0.213	12.0	6.24	6.72	3.47	-3.91E-02	0.326
Simulation5	0.0575	14.6	8.77	8.64	3.41	5.50E-02	0.415

The acceleration, velocity and displacement time histories of NGA record #285 were earlier shown in Figure 4.1. Furthermore, Figure 4.2 showed the acceleration time history, the derivative of the extracted velocity pulse, and the corresponding residual motion for this recorded motion. Figures 5.10, 5.12, 5.14, 5.16, and 5.18 show the same components for the five simulated motions. The derivative of the simulated velocity pulse is shown at the top, the simulated residual acceleration is shown in the middle, and the total simulated acceleration, obtained by adding the derivative of the pulse to the residual, is shown in the bottom. Furthermore, Figures 5.11, 5.13, 5.15, 5.17, and 5.19 show the acceleration, velocity and displacement time histories of the simulated total motions. Note that all simulated motions have zero residual velocity and displacement values at their ends. The set of total motions, including the recorded one, should be regarded as random realizations of the FN component of the ground motion

resulting for an earthquake with source and site characteristics as prescribed above. It is noted, again, that the variabilities observed in the pulse characteristics, intensities, durations, and frequency contents of these motions reflect the randomness that is inherent in FN components of near-fault ground motions having common earthquake source and site characteristics.

Figure 5.20 shows the elastic pseudo-acceleration response spectra at 5% damping of the recorded (grey line) and simulated (black lines) ground motions. For each case, the period of the corresponding mMP velocity pulse is shown as a circular marker on the spectrum curve. A peak in the spectrum at or slightly below the pulse period is observed in all cases. The variability in the spectrum shapes is a reflection of the variability in the ground motion properties (intensities, frequency contents, and durations) that can be realized for a prescribed set of earthquake source and site characteristics. It is also observed that the recorded motion has much smaller spectral amplitudes than most of the simulated motions. This is because the recorded motion has a pulse amplitude and a residual intensity that are much smaller than expected, on the average, from a near-fault ground motion of the given earthquake source and site characteristics.

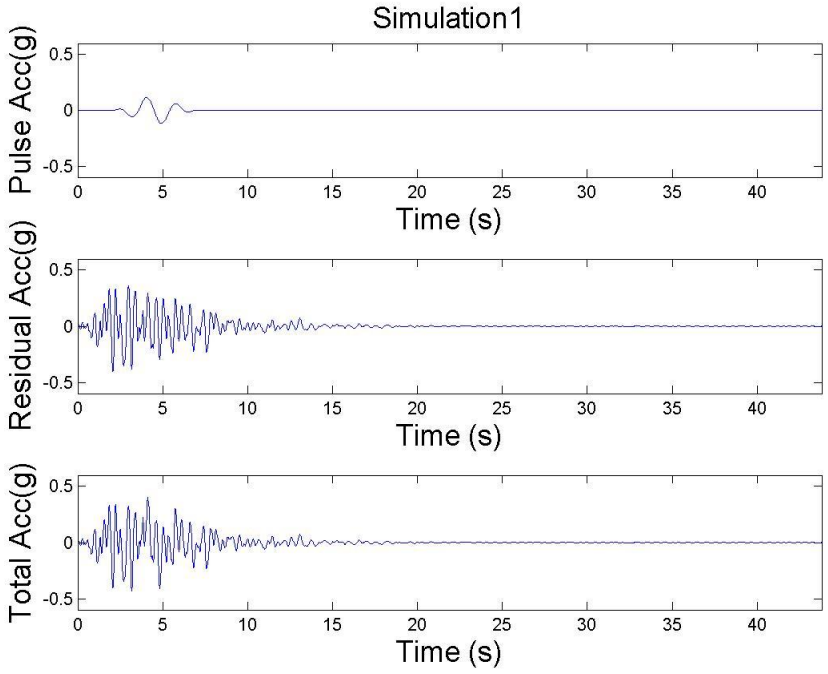

Figure 5.10: Simulated motion #1: derivative of simulated pulse (top), simulated residual motion (middle) and total simulated acceleration record (bottom)

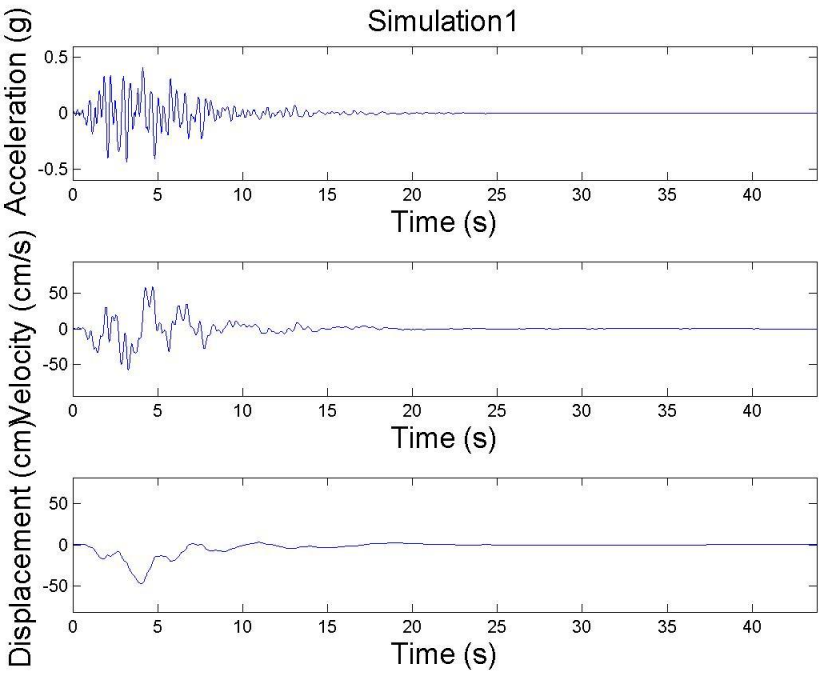

Figure 5.11: Simulated motion #1: acceleration, velocity and displacement time histories

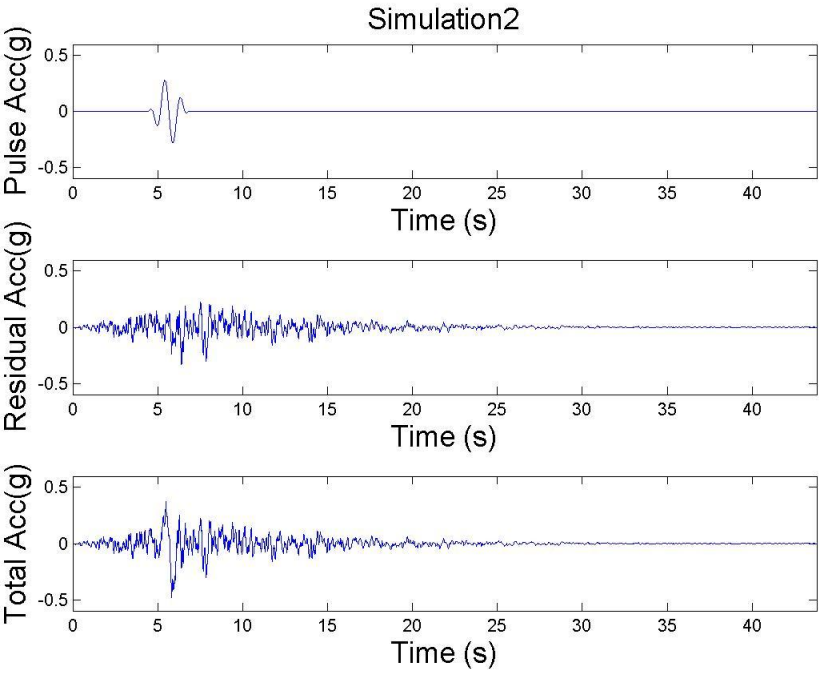

Figure 5.12: Simulated motion #2: derivative of simulated pulse (top), simulated residual motion (middle) and total simulated acceleration record (bottom)

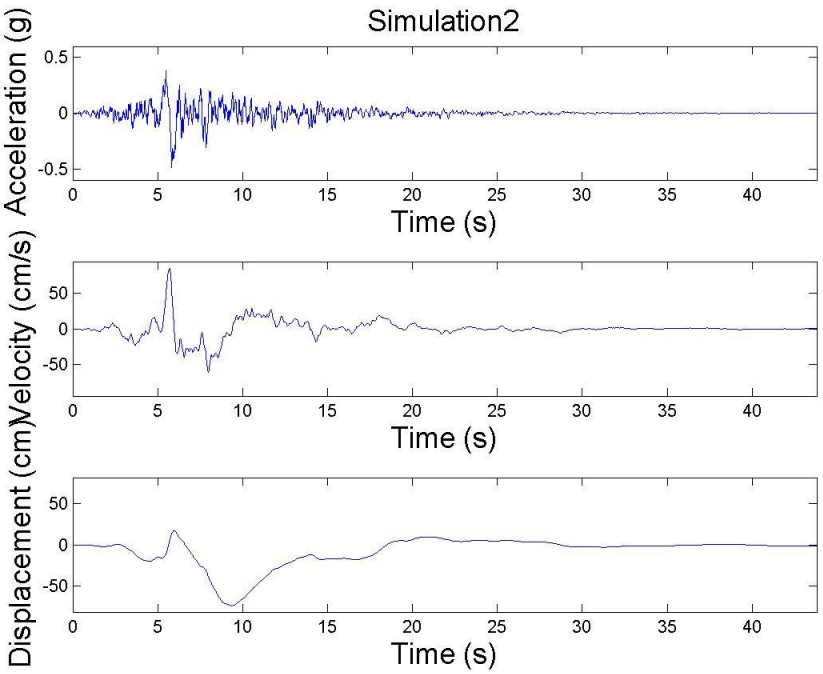

Figure 5.13: Simulated motion #2: acceleration, velocity and displacement time histories

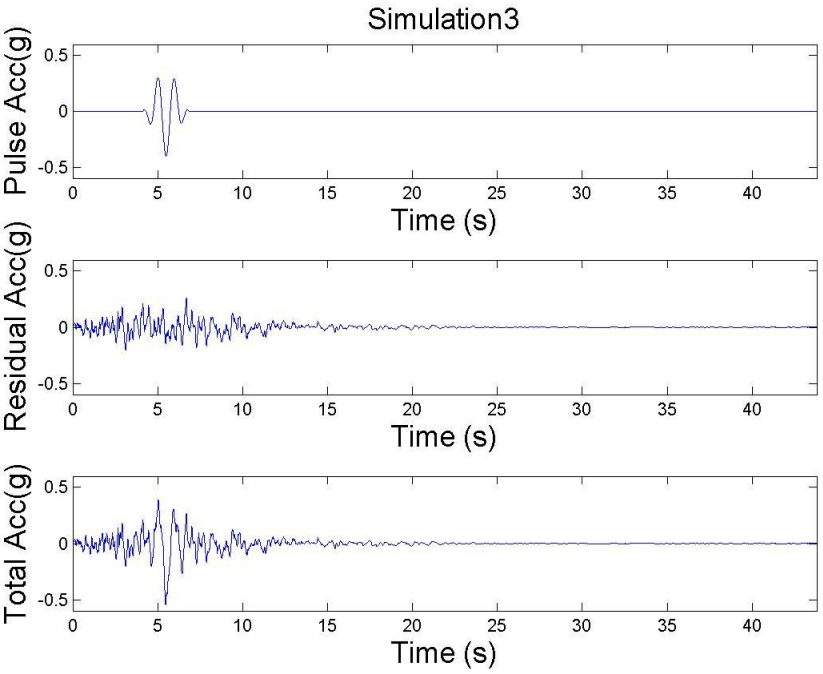

Figure 5.14: Simulated motion #3: derivative of simulated pulse (top), simulated residual motion (middle) and total simulated acceleration record (bottom)

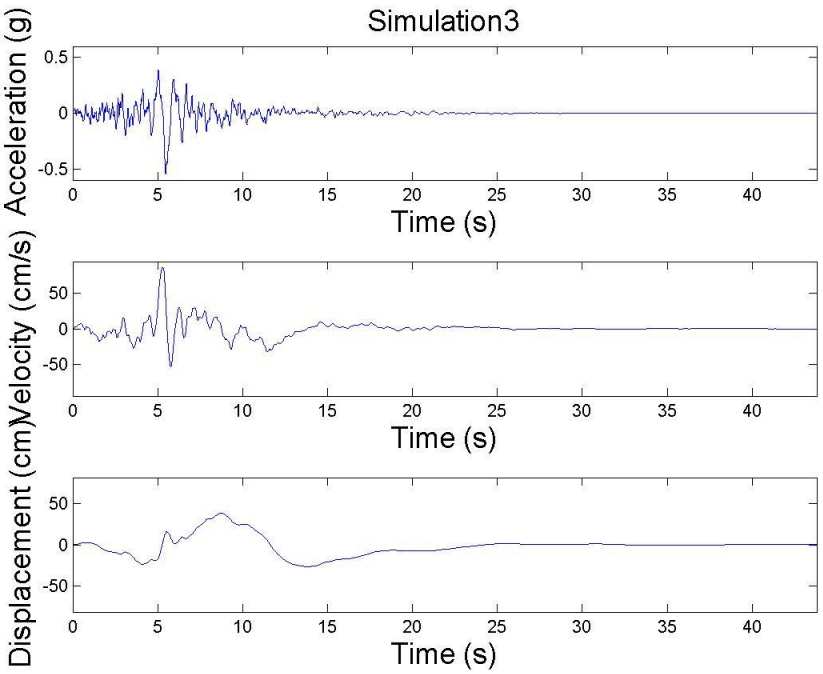

Figure 5.15: Simulated motion #3: acceleration, velocity and displacement time histories

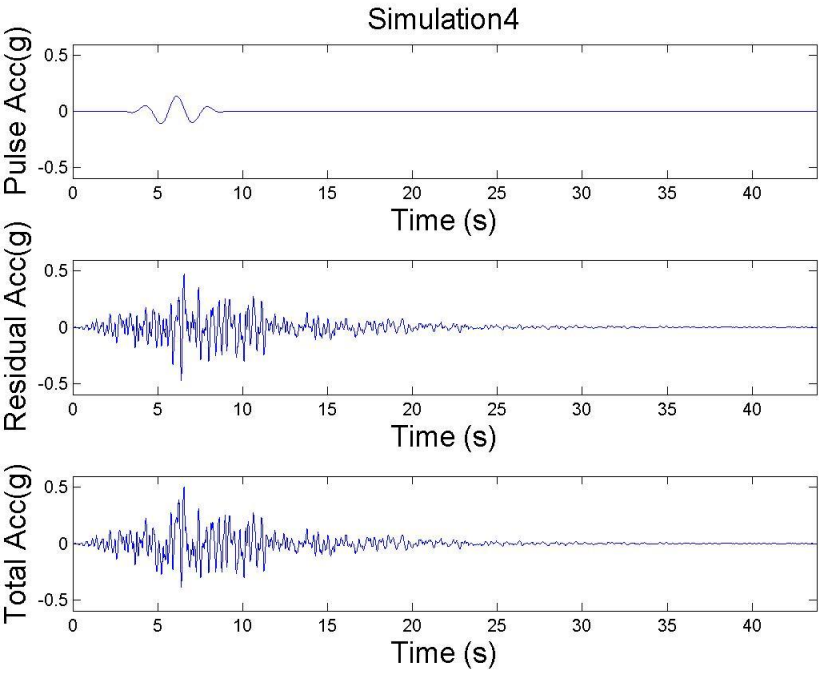

Figure 5.16: Simulated motion #4: derivative of simulated pulse (top), simulated residual motion (middle) and total simulated acceleration record (bottom)

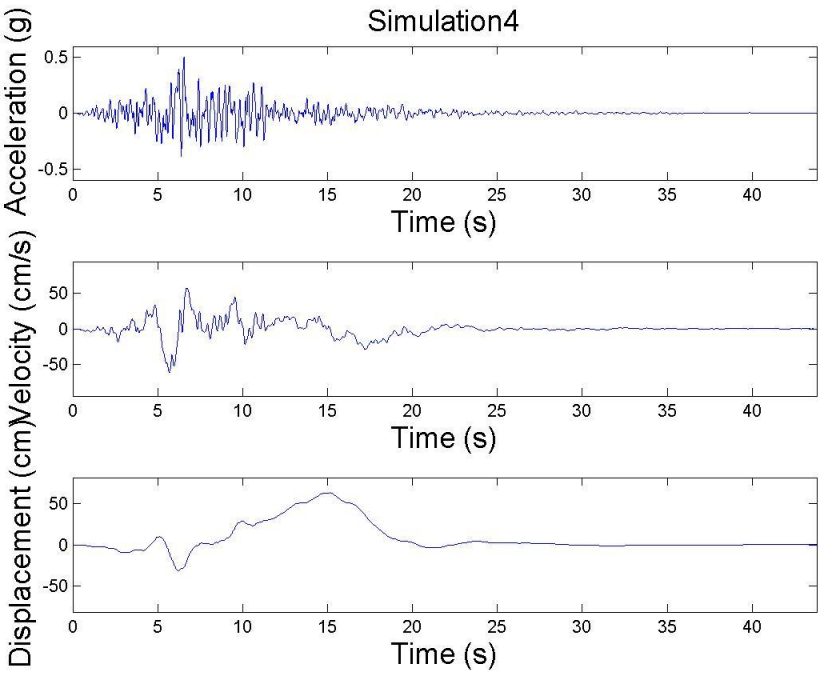

Figure 5.17: Simulated motion #4: acceleration, velocity and displacement time histories

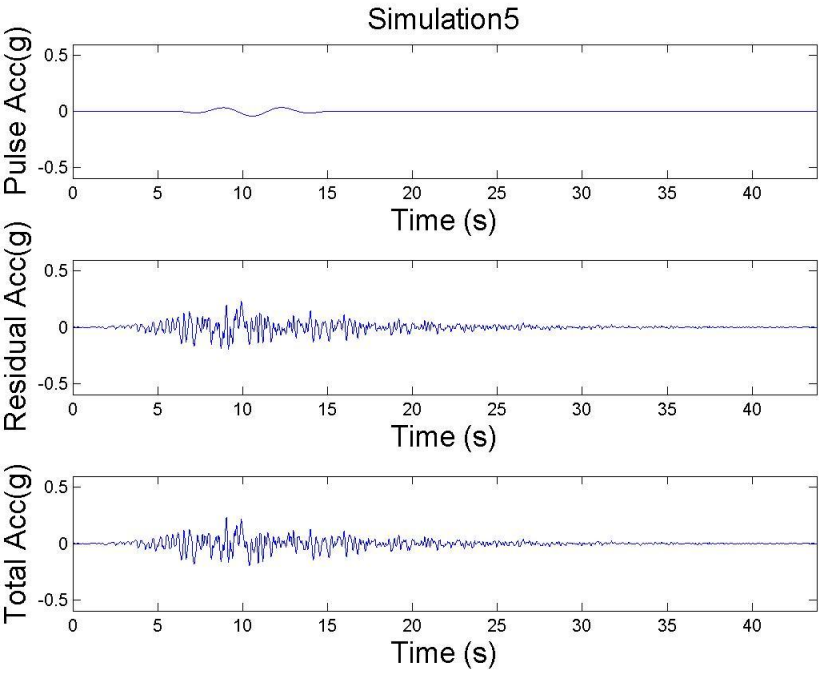

Figure 5.18: Simulated motion #5: derivative of simulated pulse (top), simulated residual motion (middle) and total simulated acceleration record (bottom)

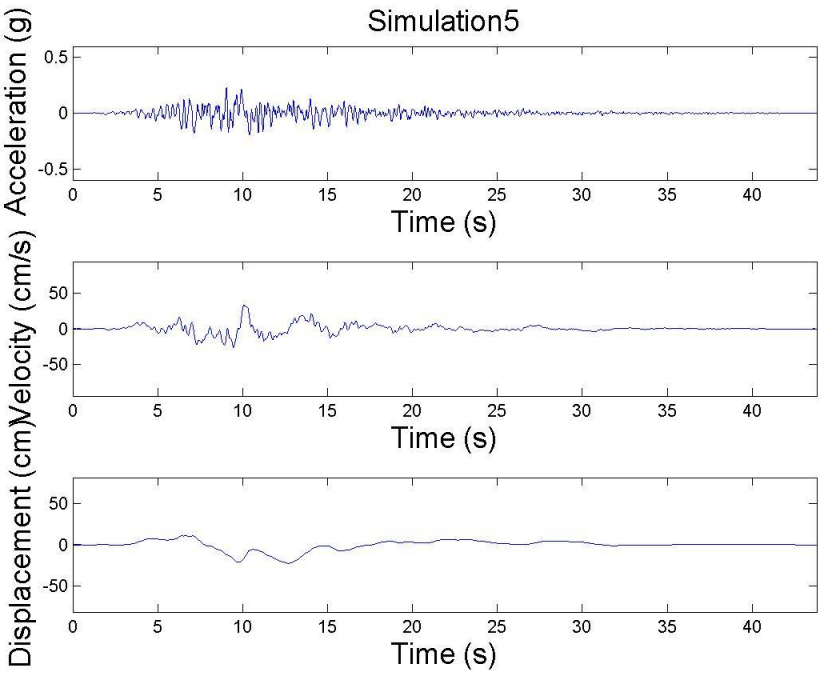

Figure 5.19: Simulated motion #5: acceleration, velocity and displacement time histories

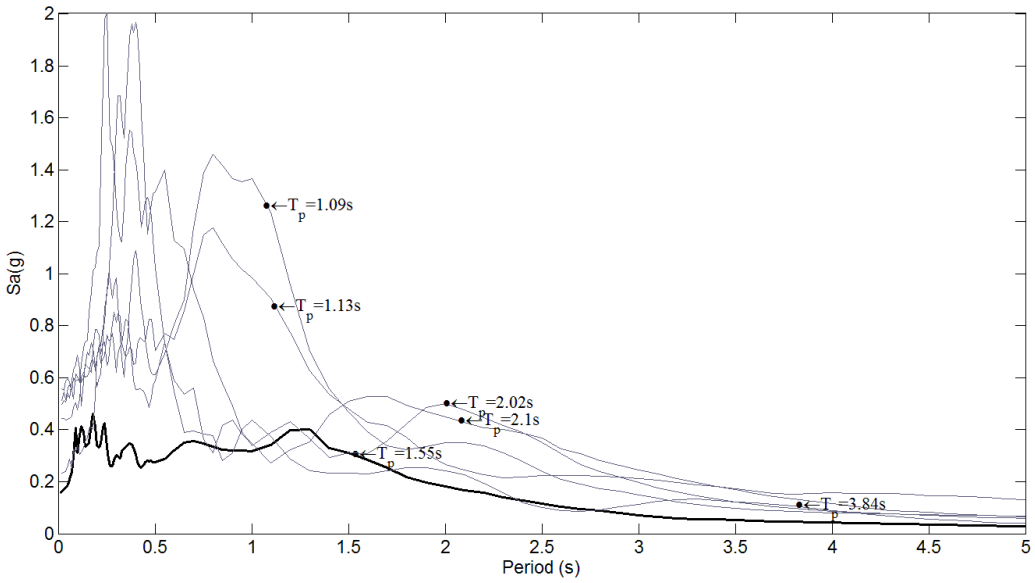

Figure 5.20: Response spectra of recorded (black) and simulated (grey) near-fault ground motions

Finally, the wavelet algorithm by Baker (2007) is applied to the synthetic ground motions to see if it detects the presence of a forward directivity pulse. Among the five simulated motions, the simulated pulses are extracted with reasonable approximation from all but the simulated motion #2. The extracted

wavelet pulses are shown in Figures 5.5-5.9 as grey lines and their periods as defined by Baker (2007) are listed in Table 5.1 under the heading $T_{p,\text{wavelet}}$. It can be seen that there is reasonable correspondence between the periods of the simulated mMP pulses and the extracted pulses for all but simulated motion #2, but in all cases the period defined for the extracted pulse is longer than the period of the simulated mMP pulse. This is also true for the recorded motion. This trend is probably due to the differences in the definition of the pulse period and in the mathematical forms of the pulses. For simulation #2, Baker's wavelet method evidently extracts a long period pulse that is present in the simulated residual motion. If we remove this pulse and extract the next pulse, we obtain the pulse shown as the dotted grey line in Figure 5.6. This pulse matches the simulated pulse and has a period of 1.13s.

Baker (2007) defines a pulse indicator, PI, to measure the likelihood that a pulse in a given near-fault ground motion record is due to the directivity effect. This measure involves the ratio of the peak velocities of the residual and total motions and the ratio of their respective energies, as measured in terms of their cumulative squared velocities. Evaluating this measure for the simulated motions, we find that only simulated motions 1, 3 and 4 have PI values greater than 0.85, which, is the threshold for unambiguous directivity pulses selected by Baker (2007). Furthermore, the pulse in simulation #1 arrives too late in the time history to qualify as a directivity pulse in accordance to Baker's definition. Thus only simulated motions #3 and #4 are identified as unambiguous pulse-like forward directivity motions by Baker's algorithm. One should keep in mind that Baker's algorithm involves some subjectivity in defining pulselike motions that are due to forward directivity. Nevertheless, if one insists on using motions that correspond to this definition, then it is possible to simulate any number of near-fault synthetic motions and then use the subset that qualifies as having forward directivity pulses for design purposes.

We also simulated five FN acceleration time histories with forward directivity pulses for each of three other sets of earthquake source and site characteristics. They are presented in the Appendix in Tables and Figures analogous to the one in this section. No discussion is provided for these additional simulations. The reader should refer back to the discussion in this section for more details.

5.4 SIMULATION OF NON-PULSELIKE NEAR-FAULT GROUND MOTIONS

For a given set of earthquake source and site characteristics, to simulate a single SN ground motion component that doesn't include a directivity pulse, we proceed exactly in the same manner as described for the residual of pulselike motions in Section 3. At the present, we assume that the predictive equations developed for the residuals are also applicable to non-pulselike motions. However, work is in progress to develop separate predictive equations by use of a database of non-pulselike near-fault ground motions. We anticipate that the differences between the two sets of predictive models will be small.

5.5 PROBABILITY OF PULSE OCCURRENCE AND SIMULATION OF NEAR-FAULT GROUND MOTIONS

Not all near-fault sites experience pulselike ground motions in the SN direction. As reviewed in Chapter 2, several researchers have investigated this matter and have come up with models that predict the probability of observing a pulse, given the earthquake source and site characteristics. We find the model by Shahi and Baker (2011) to be the most appropriate one and use it to determine the relative proportion of simulated SN ground motion components that are pulselike and non-pulselike.

To simulate a single SN ground motion component, we proceed as follows: Given the set of earthquake source and site characteristic variables $F, M_w, R, V_{s30}, \theta$ and s, we first compute the probability of observing a pulse in the SN direction. Combining Eqs. 2.25-2.29 and setting $\alpha = 90^{\text{o}}$, we compute

$$\Pr(\text{SN pulse}|F,R,s,\theta) = \frac{0.67}{1+\exp(0.642+0.167R-0.075s)}F + \frac{0.53}{1+\exp(0.128+0.055R-0.061s+0.036\theta)}(1-F) \quad (5.1)$$

where the symbols s and θ are used for both strike-slip and non-strike-slip faults (instead of d and ϕ for the latter). Note that R and s are in kilometers and θ is in degrees. For each simulation, we first use a random number generator to uniformly sample a number between 0 and 1. If the sampled number is less than or equal to $\Pr(\text{SN pulse}|F,R,s,\theta)$, a pulselike ground motion is generated as described above. If the generated number is greater than $\Pr(\text{SN pulse}|F,R,s,\theta)$, a non-pulselike ground motion is generated as described above. This process can be repeated to generate as many near-fault synthetic ground motions as necessary for the given design scenario. The suite of synthetic ground motions generated at a given site will have proportions of pulselike and non-pulselike motions that more or less match the computed probabilities of observing or not observing a pulselike motion. For the example case with the earthquake source and site characteristics belonging to NGA record #285, the predicted probability of observing a pulse in the SN direction is 0.17. Thus, 17% of simulated motions must have velocity pulses included in them.

6 Summary, Conclusions and Future Work

6.1 SUMMARY AND CONCLUSIONS

In this report, we developed a parameterized stochastic model of near-fault ground motion in the strike-normal direction. Since not all near-fault ground motions contain a forward directivity pulse, even those that are located in the forward directivity region, the model was formulated to produce both pulselike and non-pulselike ground motions.

The model for pulselike motions consists of two parts: a 5-parameter idealized model of the directivity velocity pulse, and a 7-parameter model of the residual motion. The pulse model is a modified version of an idealized velocity pulse model earlier developed by Mavroeidis and Papageorgiou (2003). The modification assures that the pulse has zero residual displacement at the end of the motion. The model for the residual is the modulated filtered, white-noise process formulated by Rezaeian and Der Kiureghian (2008) with its gamma modulating function replaced by a 4-parameter modulating function that is more appropriate for near-fault ground motions. By fitting the two sub-models to a database of extracted pulses and residuals of recorded near-fault pulselike ground motions, we develop predictive equations for the 12 model parameters in terms of earthquake source and site characteristics. Correlation coefficients between the model parameters are empirically estimated by analysis of the regression residuals. These correlations embody the dependencies that exist between the various characteristics of pulselike ground motions, for example the relation between the pulse amplitude and the intensity of the residual motion, or the relation between the pulse period and the duration of the motion. To simulate a pulselike ground motion for a given set of earthquake source and site characteristics, we use these predictive equations and correlation coefficients to generate a set of model parameters; these parameter values are then used together with a simulated band-limited, white-noise process in the model formulas to generate a sample realization. One can repeatedly generate sets of model parameters and use them to generate an ensemble of synthetic near-fault pulselike ground motions for the given set of earthquake source and site characteristics. The resulting ensemble of synthetic motions have the same statistical characteristics as the motions in the database, including the record-to-record variability for the given set of earthquake source and site characteristics.

The model for non-pulselike near-fault ground motions consists of a 7-parameter model identical to that of the residual part of pulselike motions. By fitting the model to a database of recorded non-

pulselike near-fault ground motions, we can develop predictive equations for the model parameters in terms of earthquake and site characteristics. Furthermore, correlation coefficients between the model parameters can be empirically estimated by analysis of the regression residuals, thus capturing the dependencies that may exist between the various characteristics of the motion, such as its intensity and duration or intensity and predominant frequency. Samples of non-pulselike motions can then be generated in the same manner as samples of the residuals of pulselike motions. At the present stage of our study, it is assumed that the predictive equations and correlations for non-pulselike motions are identical to those of the residuals of pulselike motions. In the next stage of the study, we will perform independent fittings to a database of non-pulse near-fault ground motions and develop specialized predictive equations and correlation coefficients. We anticipate that the differences between the two sets of predictive equations and correlation coefficients will not be large.

To account for the fact that not all near-fault ground motions at a given site contain velocity pulses, first the probability of occurrence of a directivity pulse is calculated. A predictive model for this probability in terms of earthquake source and site characteristics is developed by Sashi and Baker (2011). For a prescribed set of earthquake source and site characteristics, this probability is first computed and then strike-normal ground motions with and without a pulse are simulated according to the predicted proportions.

Two types of synthetic ground motions were investigated in this study: (a) Synthetic motions generated using model parameters that are obtained by fitting the model to a recorded motion. These motions essentially represent different realizations of near-fault ground motions for the same earthquake. (b) Synthetic motions generated using randomly selected values of the model parameters for prescribed earthquake source and site characteristics. These motions represent realizations of near-fault ground motions from different earthquakes with similar source and site characteristics. The variability observed in the latter set of synthetic motions reflects the natural variability inherent in real near-fault ground motions for earthquakes having similar source and site characteristics. For both cases, comparisons were made between the characteristics of simulated and recorded motions and a number of interesting and important observations were made. Even though the selected models cannot reproduce all features of recorded motions, overall they provide synthetic motions that are realistic and faithfully produce those features that are particularly important from the viewpoint of designing bridges and long-period structures. This includes the characteristics of the directivity pulse present in the synthetic motion and its effect on the corresponding response spectrum in the long period range.

The synthetic near-fault ground motions generated by the method proposed in this study can be used for a variety of applications. They can be used for nonlinear dynamic analysis of tall buildings, base-

isolated structures, bridges or other structures located at near-fault sites. Such structures can be particularly vulnerable to near-fault motions if they possess resonant periods that are long and close to the period of the directivity pulse. A suite of the synthetic motions can be used for performance-based analysis by Monte Carlo simulation, where expected estimates of costs of damage or downtime must be made. Finally, the synthetic motions offer a possibility for parametric analysis to understand the influences of various assumptions in the design stage.

6.2 FURTHER STUDIES

In this study, ground motions are identified as pulselike by use of the wavelet classification algorithm developed by Baker (2007). The advantages of this algorithm are that it is automated, objective and repeatable, and it does not require the exercise of judgment by the user. However, there is no collective agreement on what the definition of a pulse or a pulselike motion is, and Baker's algorithm is just one of the proposed methods to perform classification. Baker's algorithm may not identify as pulselike a motion that other experts would consider pulselike, and vice versa. Nonetheless, in general, Baker's classification is in agreement with other findings. This method is used in this study not only to classify ground motions, but also for extracting the velocity pulse to which a theoretical model is then fitted. It is reasonable to expect that pulselike synthetic motions generated by use of Baker's classification approach ought to also be classified as pulselike by his algorithm. As shown in Chapter 5, this is not the case for all of the simulated "pulselike" ground motions. Future work will look into this matter in order to improve the model. It should be noted in this connection that so far we have defined each residual motion in the data base as the total ground motion minus the extracted pulse. In order to better characterize the ground motion for subsequent model parameter identification, it might be better to define the residual component by subtracting the fitted idealized pulse from the total recorded ground motion rather than the actual extracted pulse. This way, less record information is lost in the fitting procedure. Furthermore, it might be better to develop predictive regression models in terms of alternate parameters, such as the ratio of the pulse amplitude to Arias intensity of the total motion or measures of energy in the motions with and without the pulse. One alternative model for the pulse amplitude was explored in Chapter 3, but not yet fully developed. We intend to explore these alternative modeling and estimation approaches to improve the simulation model.

In this study, no lower bound is imposed on the shear-wave velocity of the upper 30m of the soil column (V_{s30}) at sites where ground motions are recorded and simulated. The database includes ground motions recorded at sites with V_{s30} as low as 163m/s at the El Centro Array #3 station that recorded the 1979 Imperial Valley earthquake. However, for soft rock and soil sites, generally defined by shear-wave

velocities lower than 760m/s, the response of the site to the input bedrock motion is not linear, and tends to be highly non-linear at very soft sites. Surface motions at such softer sites are strongly dependent on the detailed properties and layering of the soil profile at the site. V_{s30} alone is not a sufficiently good descriptor of the soil profile, as two sites with different layering and properties, thus different soil effects, can still have the same V_{s30}. Even with additional information, such as depth factors $Z_{1.0}$ and $Z_{2.5}$ used in the NGA database, V_{s30} cannot adequately describe individual soil profiles. The best way to properly account for the effects of local soils and soil nonlinearity is to simulate rock motions and then use them as input bedrock motions into a soil profile in order to compute the surface motion. The surface motion can be obtained by performing 1-dimensional equivalent visco-elastic model analysis of the site using a program such as SHAKE. If very high strain levels are expected, or if basin and topographic effects are deemed important, then 2- or 3-dimensional analyses should be performed.

To improve the modeling of the local soil effect, we have two options. One is to limit the data to near-fault ground motions recorded on rock sites. This is not practical, since this would severely limit the size of our database, making it virtually impossible to do any meaningful statistical analysis. The second approach is to take each recording on a non-rock site and through back-calculation and use of detailed local site information determine the corresponding bedrock motion. This requires detailed knowledge of each recording site, which unfortunately is not available for many of the near-fault records in the database. We intend to continue exploring ways of better accounting for the site effects.

A number of improvements can be made in the development of the predictive equations. Firstly, different forms of the regression models can be explored, guided by physical considerations where possible. For example, replacing $\ln R$ by $\ln(R + c)$ may be considered, since the latter form may provide a better model for near-fault sites. However, it will require non-linear regression analysis. Furthermore, different regression equations may be considered for strike-slip and non-strike-slip faults. However, the size of the available dataset may be too small for such refinements. Finally, it is noted that the regression analysis performed in this study did not account for the variable number of records used from each earthquake in the database. This can be done by using random effects regression, as performed in Rezaeian and Der Kiureghian (2010) for far-field motions. However, the small data size may again prove to be an impediment for such refinement. This kind of analysis is currently in progress. Until then, the results reported in this report should be regarded as preliminary in nature.

This study limited its focus to modeling and simulation of the strike-normal component of the near-fault ground motion. To provide a multi-component description of the near-fault ground motion, we intend to also develop a model for the strike parallel component. One perceived difficulty with this is that the fling step for most observed strike-normal ground motion components is absent from the processed

data because of baseline correction or other filtering effects. As a result, a model for the fling step will need to be developed from physical considerations of the earthquake source.

Finally, this study was limited to the simulation of the strike-normal component of the near-fault ground motion at one station for given earthquake source and site characteristics. Ground motions arising from the same earthquake but recorded at different stations tend to display spatial variability. The three main causes of spatial variability are the incoherence effect, the wave passage effect and the site response effect. Ground motions recorded at closely spaced stations tend to exhibit more similarities than ones recorded at distantly spaced stations. This type of spatial variability can be described by a spatial correlation matrix. We intend to extend our study to model and simulate arrays of ground motions at specified locations near a fault arising from a single earthquake event. To do so, we will need to develop and assess models that describe the spatial variability of both the velocity pulse and the residual motion.

REFERENCES

Abrahamson, N. (2001). *Development of Fling Model for Diablo Canyon ISFSI.* Pacific Gas and Electric Company, Geosciences Department, Calc. No. GEO.DCPP.01.12.

Abrahamson, N., Atkinson, G., Boore, D., Campbell, K., Chiou, B., Idriss, I. M., et al. (2008). Comparisons of the NGA Ground-Motion Relations. *Earthquake Spectra , 24* (1), 45-66.

Aki, K., & Richards, P. G. (1980). *Quantitative Seismology: Theory and Methods.* San Francisco: W.H. Freeman.

Alavi, B., & Krawinkler, H. (2000). Consideration of near-fault ground motion effects in seismic design. *Proceedings, 12th World Conference on Earthquake Engineering*, (pp. 1-8). New Zealand.

Archuleta, R. J., & Hartzell, S. H. (1981). Effects of fault finiteness on near-source ground motion. *Bulletin of the Seismological Society of America , 71*, 939-957.

Baker, J. (2007). Quantitative classification of near-fault ground motions using wavelet analysis. *Bulletin of the Seismological Society of America , 97* (5), 1486-1501.

Bray, J. D., & Rodriguez-Marek, A. (2004). Characterization of forward-directivity ground motions in the near-fault region. *Soil Dynamics and Earthquake Engineering , 24*, 815-828.

Chioccarelli, E., & Iervolino, I. (2010). Near-source seismic demand and pulse-like records: A discussion for L'Aquila earthquake. *Earthquake Engineering and Structural Dynamics , 39* (9), 1039–1062.

Douglas, J., & Aochi, H. (2008). A survey of techniques for predicting earthquake ground motions for engineering purposes. *Surveys in Geophysics , 29*, 187-220.

Dreger, D., Hurtado, G., Chopra, A., & Larsen, S. (2011). Near-field across-fault seismic ground motions. *Bulletin of the Seismological Society of America , 101* (1), 202-221.

Fu, Q., & Menun, C. (2004). Seismic-environment-based simulation of near-fault ground motions. *Proceedings of the 13th World Conference on Earthquake Engineering.* Vancouver, Canada.

Iervolino, I., & Cornell, C. A. (2008). Probability of occurrence of velocity pulses in near-source ground motions. *Bulletin of the Seismological Society of America , 98* (5), 2262–2277.

Kramer, S. L. (1996). *Geotechnical Earthquake Engineering.* Upper Saddle River, New Jersey: Prentice Hall.

Mavroeidis, G. P., & Papageorgiou, A. S. (2003). A mathematical representation of nearfault ground motions. *Bulletin of the Seismological Society of America , 93* (3), 1099-1131.

Mavroeidis, G. P., & Papageorgiou, A. S. (2002). Near-source strong ground motion: characteristics and design issues. *Proc. of the Seventh U.S. National Conf. on Earthquake Engineering (7NCEE).* Boston, Massachusetts.

Menun, C., & Fu, Q. (2002). An analytical model for near-fault ground motions and the response of SDOF systems. *Proceedings of the 7th U.S. National Conference on Earthquake Engineering.* Boston, Massachusetts.

Rezaeian, S., & Der Kiuerghian, A. (2010). Simulation of synthetic ground motions for specified earthquake and site characteristics. *Earthquake Engineering & Structural Dynamics , 39*, 1155-1180.

Rezaeian, S., & Der Kiureghian, A. (2008). A stochastic ground motion model with separable temporal and spectral nonstationarities,. *Earthquake Engineering & Structural Dynamics , 37*, 1565-1584.

Shahi, S. K., & Baker, J. W. (2011). An empirically calibrated framework for including the effects of near-fault directivity in probabilistic seismic hazard analysis. *Bulletin of the Seismological Society of America , 101* (2), 742-755.

Somerville, P. (2002). Characterizing Near Fault Ground Motion for the Design and Evaluation of Bridges. *The 3rd National Conference & Workshop on Bridges & Highways.* Portland, Oregon.

Somerville, P. G. (1998). Development of an Improved Representation of Near-Fault Ground Motions. *SMIP 98: Seminar on Utilization of Strong Motion Data* , 1-20. Oakland, CA.

Somerville, P. G. (2003). Magnitude scaling of the near fault rupture directivity pulse. *Physics of the Earth and Planetary Interiors , 137*, 201-212.

Somerville, P. G., & Graves, R. (1993). Conditions that give rise to unusually large long period ground motions. *Structural Design of Tall Buildings , 2*, 211–232.

Somerville, P. G., Smith, N. F., Graves, R., & Abrahamson, N. A. (1997). Modification of Empirical Strong Ground Motion Attenuation Relations to Include the Amplitude and Duration Effects of Rupture Directivity. *Seismological Research Letters , 68*.

Somerville, P. (2000). Seismic Hazard Evaluation. *12th World Conference on Earthquake Engineering.* Auckland, N.Z.

APPENDIX

In Chapter 5, to illustrate the proposed simulation procedure, we simulated five FN acceleration time histories with forward directivity pulses for one set of earthquake source and site characteristics corresponding to NGA record #285. The results were presented and discussed in Section 5.3. For further illustration, in this appendix we present the results for sets of five simulated FN acceleration time histories with forward directivity pulses for each of three additional sets of earthquake source and site characteristics. The sets of earthquake source and site characteristics are selected to be identical to those of recorded pulselike motions in our database, NGA records #1120, # 1605 and #4100. Tables A1.1-A3.2 and Figures A1.1-A3.18 present the results in a format analogous to the corresponding ones in Section 5.3. No discussion is provided for these additional simulations. The reader can refer to the discussion in section 5.3.1 for clarification.

1. NGA RECORD # 1120:

- Recorded at the Takatori station during the 1995 Kobe earthquake in Japan.
- F = 1, M_w = 6.9, R = 1.5km, V_{s30} = 256m/s, θ = 13.3°, and s = 12.81km.

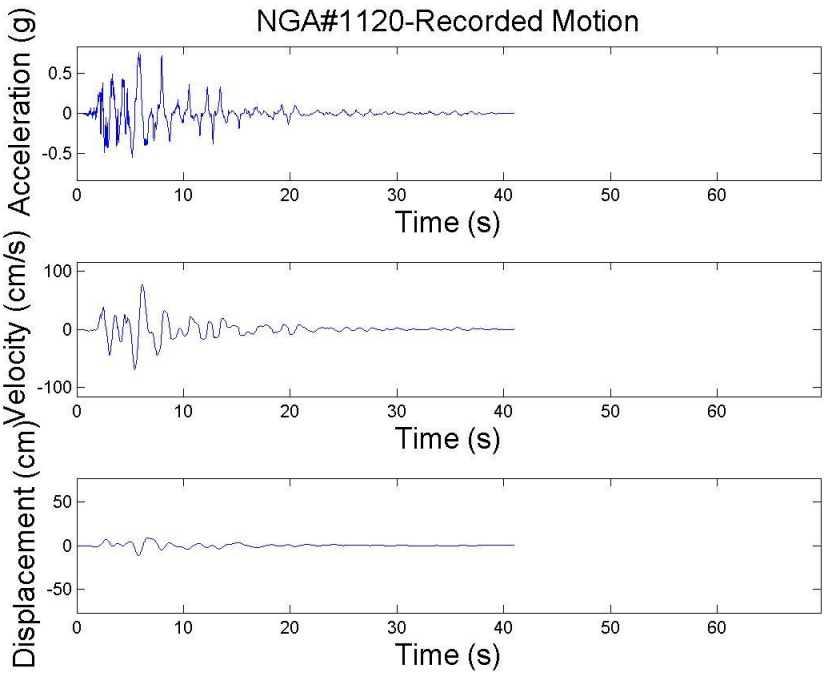

Figure A1.1: Acceleration, velocity and displacement time histories of NGA record #1120

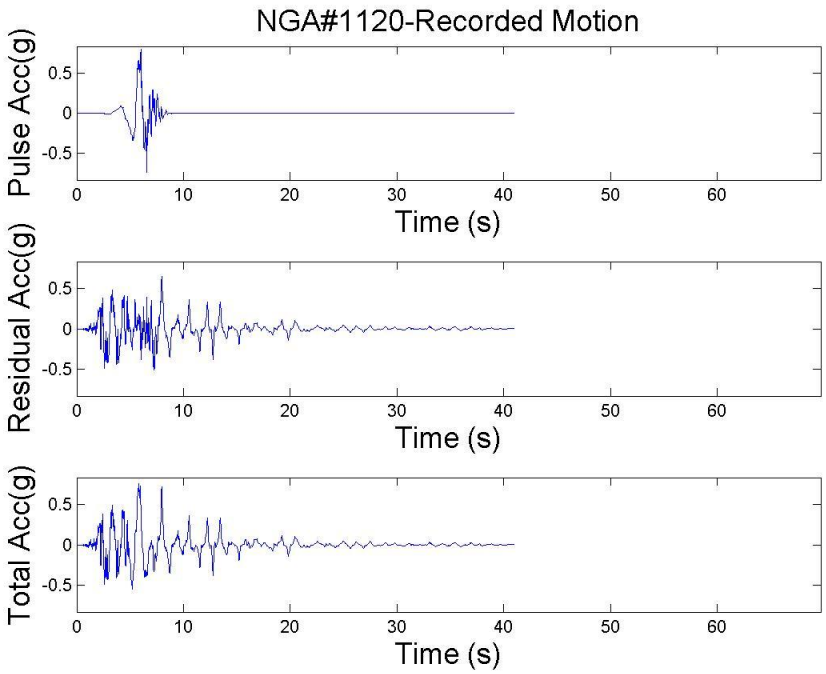

Figure A1.2: Acceleration time history (bottom), derivative of extracted velocity pulse (top), and residual acceleration time history (middle) of NGA record #1120

Table A1.1: Parameters of the recorded and simulated pulses for prescribed earthquake source and site characteristics

	V_p	T_p	γ	ν/π	$t_{max,p}$	$T_{p,\text{wavelet}}$	PI	Pulselike?
	cm/s	s		rad	s	s		
Median	64.4	4.16	2.28	1.00	6.76			
Recorded	139.5	1.66	2.23	4.60	5.80	1.54		Y
Simulation 1	24.3	3.84	2.30	1.09	7.18	4.42	0.99	Y
Simulation 2	77.2	3.91	2.41	1.75	5.13	3.93	0.04	N
Simulation 3	45.8	3.42	2.39	0.18	6.14	3.86	1.00	Y
Simulation 4	108.5	4.15	2.16	0.30	6.13	4.79	1.00	Y
Simulation 5	93.2	3.91	2.76	0.48	8.31	3.86	1.00	N

Table A1.2: Parameters of the recorded and simulated residuals for prescribed earthquake source and site characteristics

	$I_a/(\frac{\pi}{2g})$	D_{5-95}	t_{30}	$t_{max,r}$	ω_{mid}	ω'	ζ_f
	g^2s	s	s	s	Hz	Hz/s	
Median	0.098	13.3	6.33	6.43	3.65	-6.96 E-02	0.372
Recorded	0.475	11.0	2.90	2.08	2.83	-10.4 E-02	0.546
Simulation1	0.039	23.2	4.02	3.61	4.91	-29.3 E-02	0.252
Simulation2	0.251	17.1	4.33	3.35	2.63	-1.86 E-02	0.591
Simulation3	0.058	11.0	4.53	4.09	3.34	-17.6 E-02	0.232
Simulation4	0.205	9.30	3.59	3.27	1.53	-0.96 E-02	0.154
Simulation5	0.087	14.2	7.89	12.3	2.04	-0.77 E-02	0.238

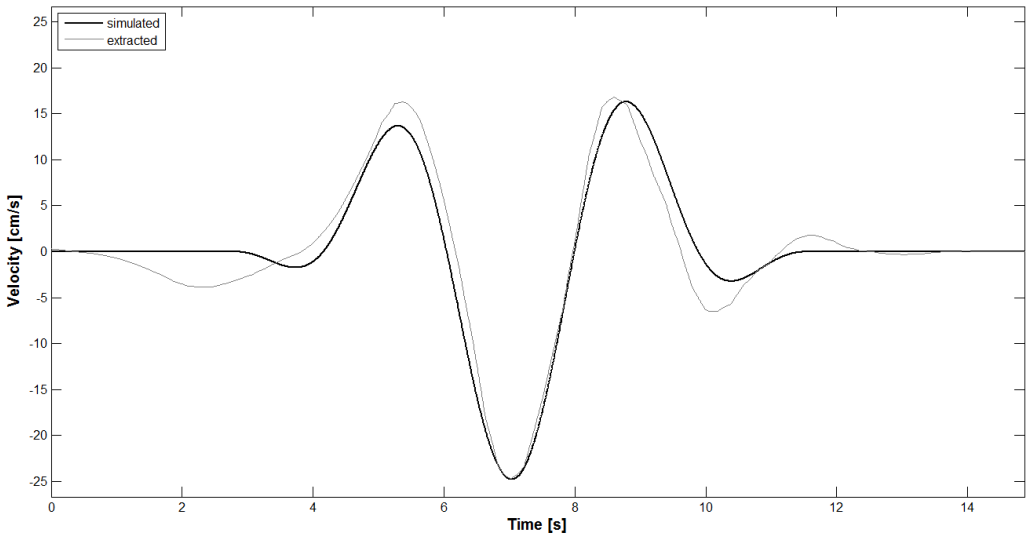

Figure A1.3: Simulated mMP velocity pulse #1 (black line) and extracted pulse from total simulated motion #1 (grey line)

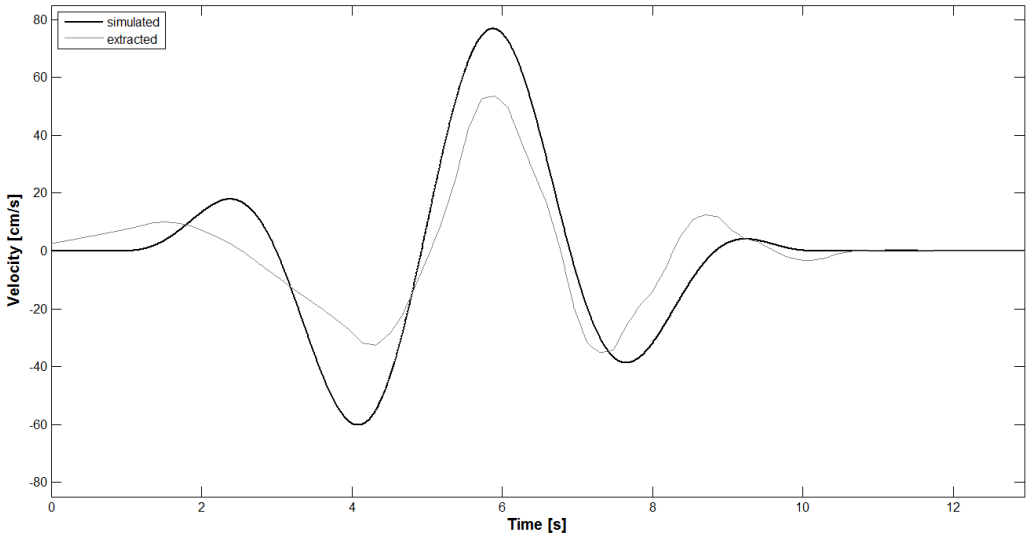

Figure A1.4: Simulated mMP velocity pulse #2 (black line) and extracted pulse from total simulated motion #2 (grey line)

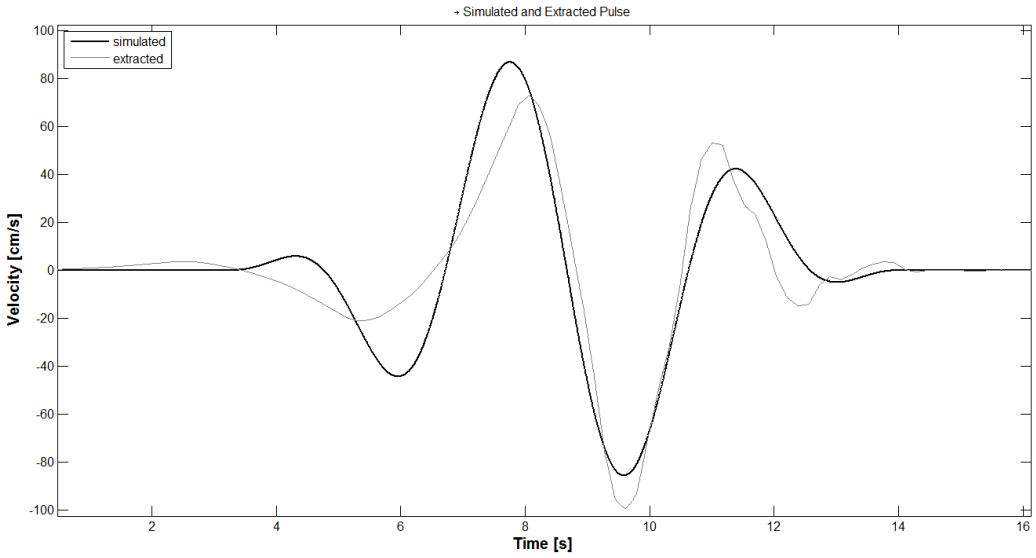

Figure A1.5: Simulated mMP velocity pulse #3 (black line) and extracted pulse from total simulated motion #3 (grey line)

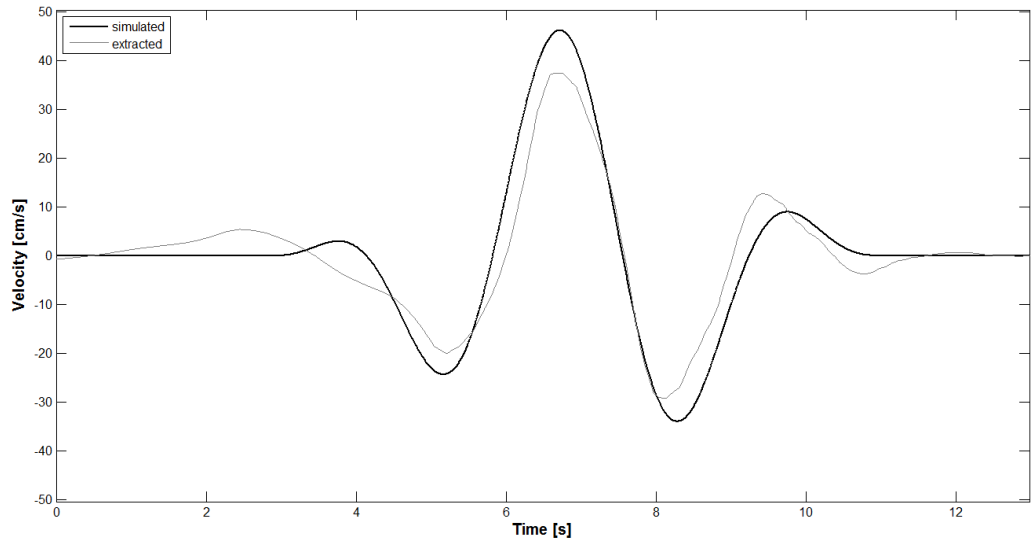

Figure A1.6: Simulated mMP velocity pulse #4 (black line) and extracted pulse from total simulated motion #4 (grey line)

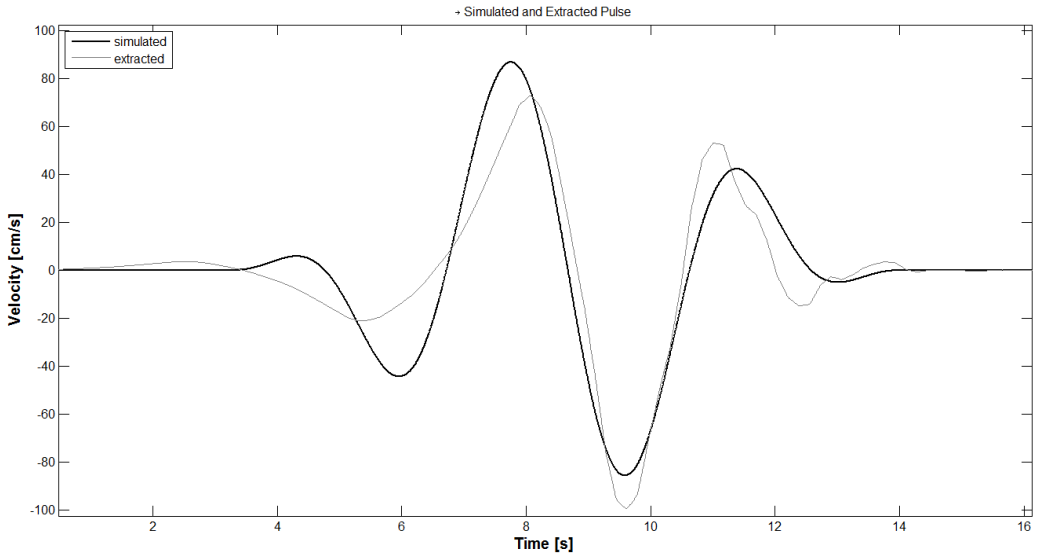

Figure A1.7: Simulated mMP velocity pulse #5 (black line) and extracted pulse from total simulated motion #5 (grey line)

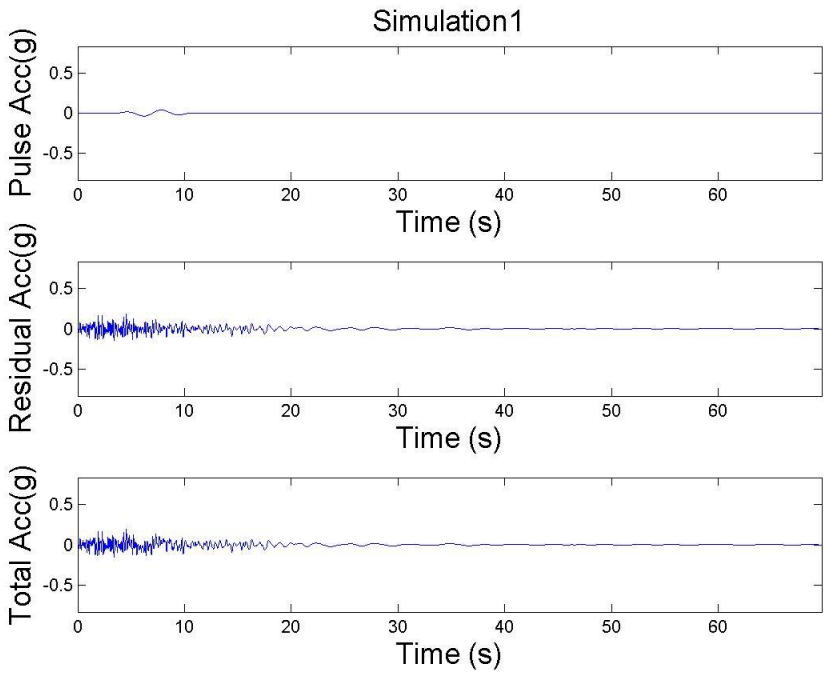

Figure A1.8: Simulated motion #1: derivative of simulated pulse (top), simulated residual motion (middle) and total simulated acceleration record (bottom)

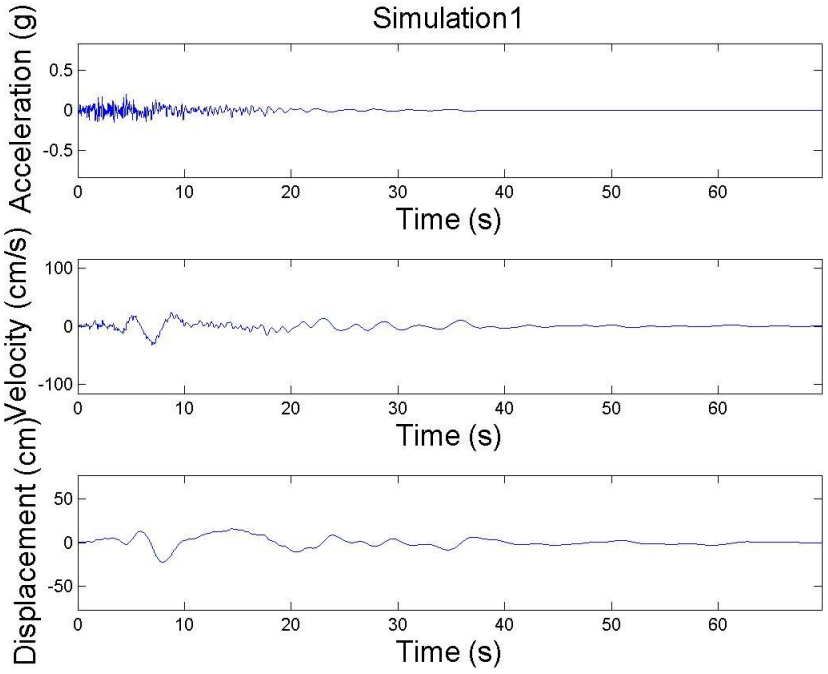

Figure A1.9: Simulated Motion 1: acceleration, velocity and displacement time histories

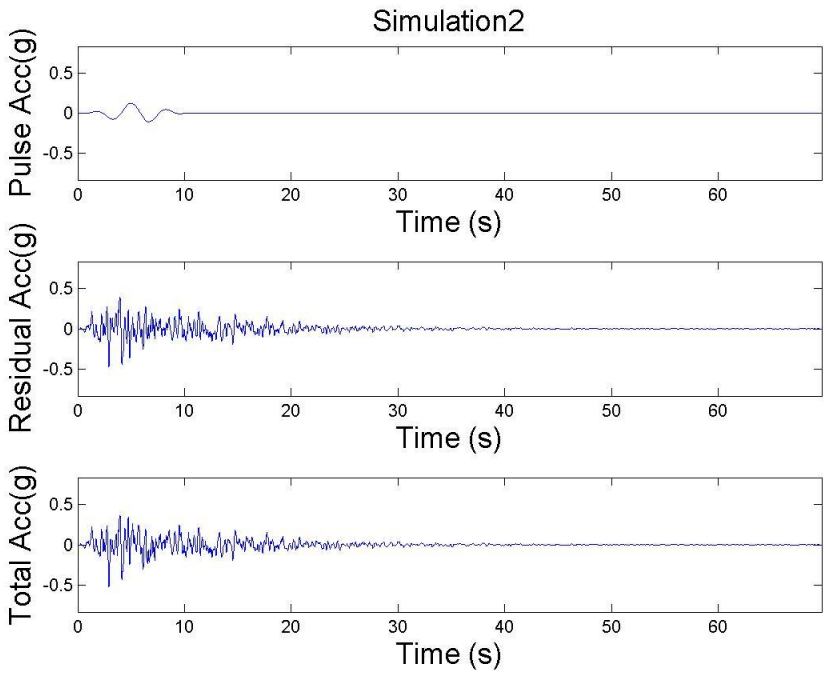

Figure A1.10: Simulated Motion 2: derivative of simulated pulse (top), simulated residual motion (middle) and total simulated acceleration record (bottom)

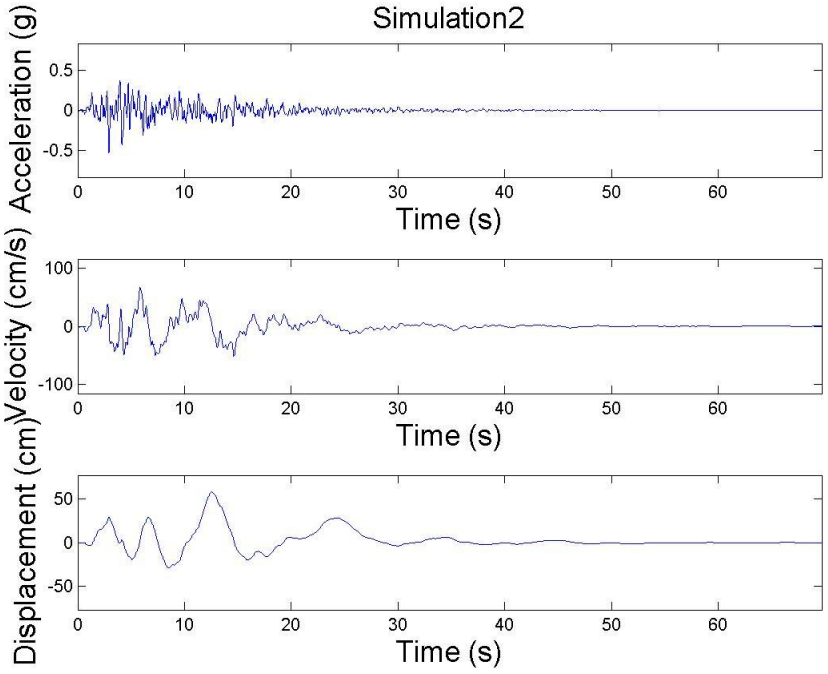

Figure A1.11: Simulated Motion 2: acceleration, velocity and displacement time histories

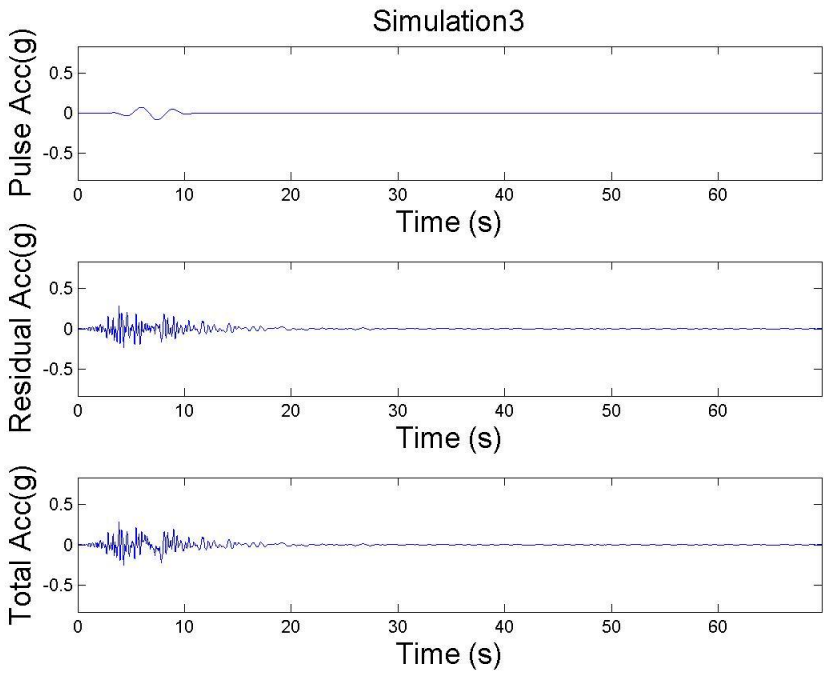

Figure A1.12: Simulated Motion 3: derivative of simulated pulse (top), simulated residual motion (middle) and total simulated acceleration record (bottom)

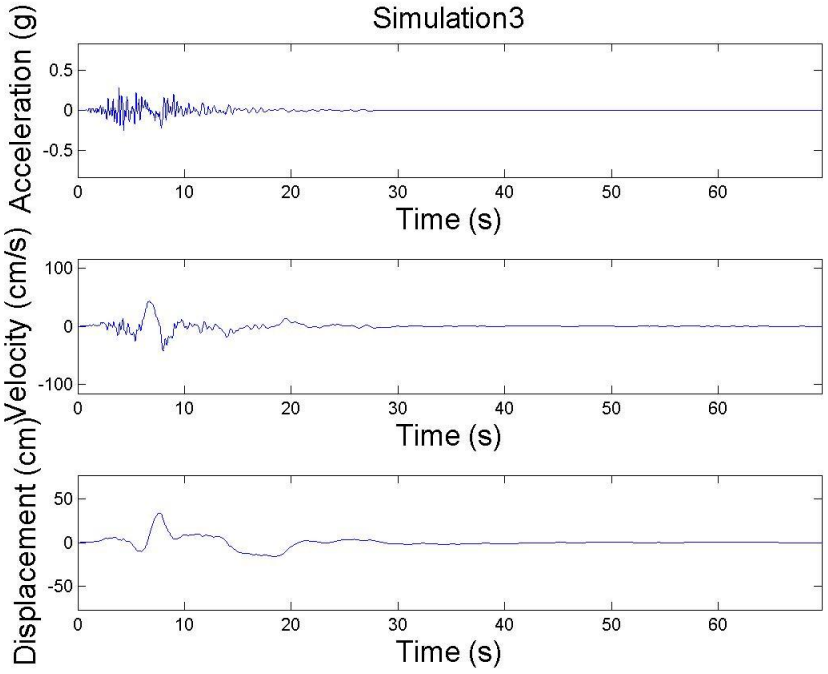

Figure A1.13: Simulated Motion 3: acceleration, velocity and displacement time histories

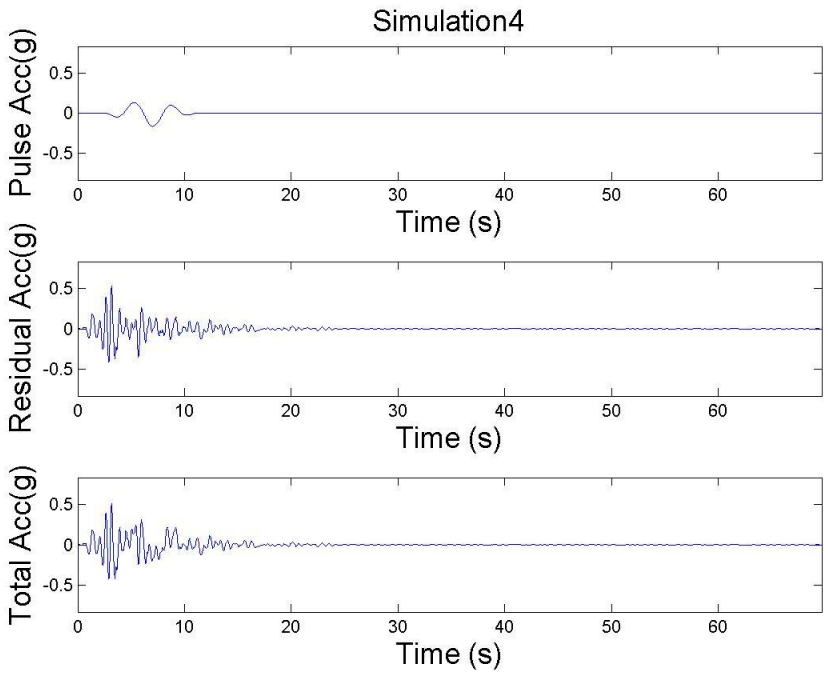

Figure A1.14: Simulated Motion 4: derivative of simulated pulse (top), simulated residual motion (middle) and total simulated acceleration record (bottom)

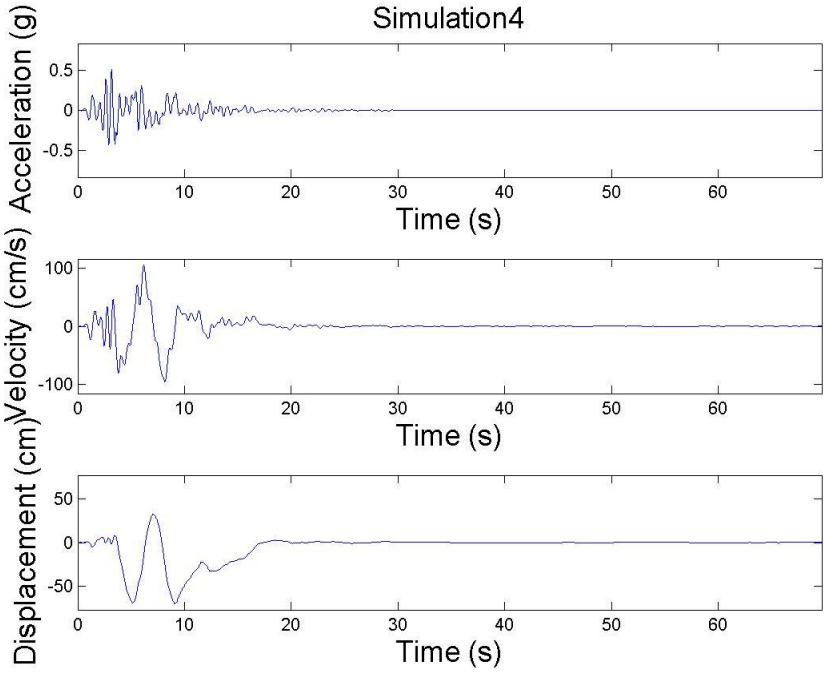

Figure A1.15: Simulated Motion 4: acceleration, velocity and displacement time histories

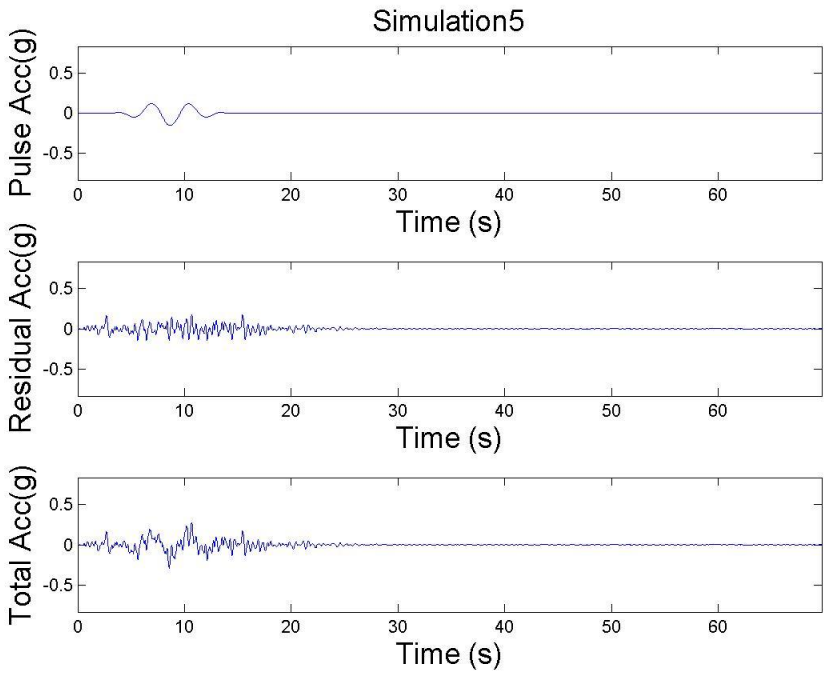

Figure A1.16: Simulated Motion 5: derivative of simulated pulse (top), simulated residual motion (middle) and total simulated acceleration record (bottom)

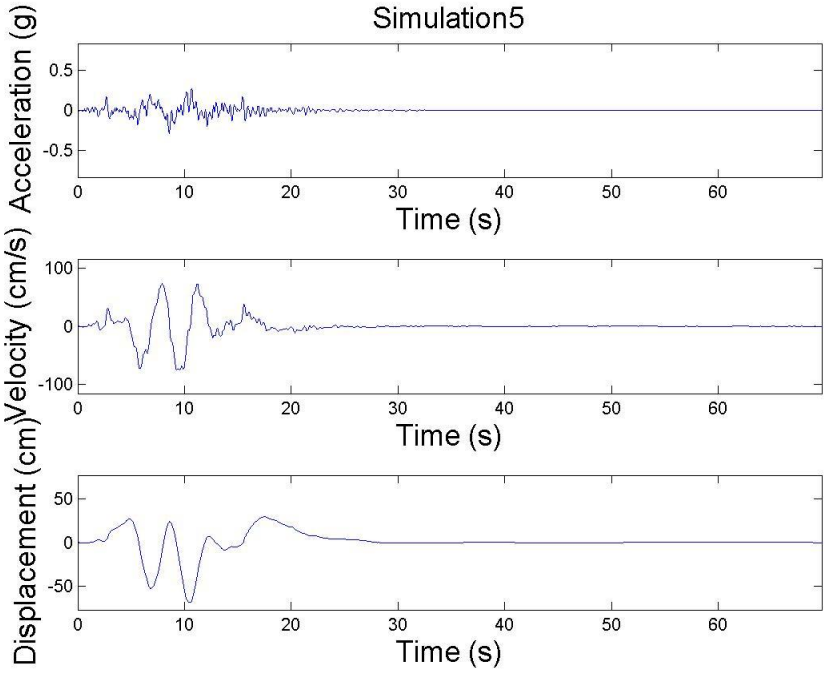

Figure A1.17: Simulated Motion 5: acceleration, velocity and displacement time histories

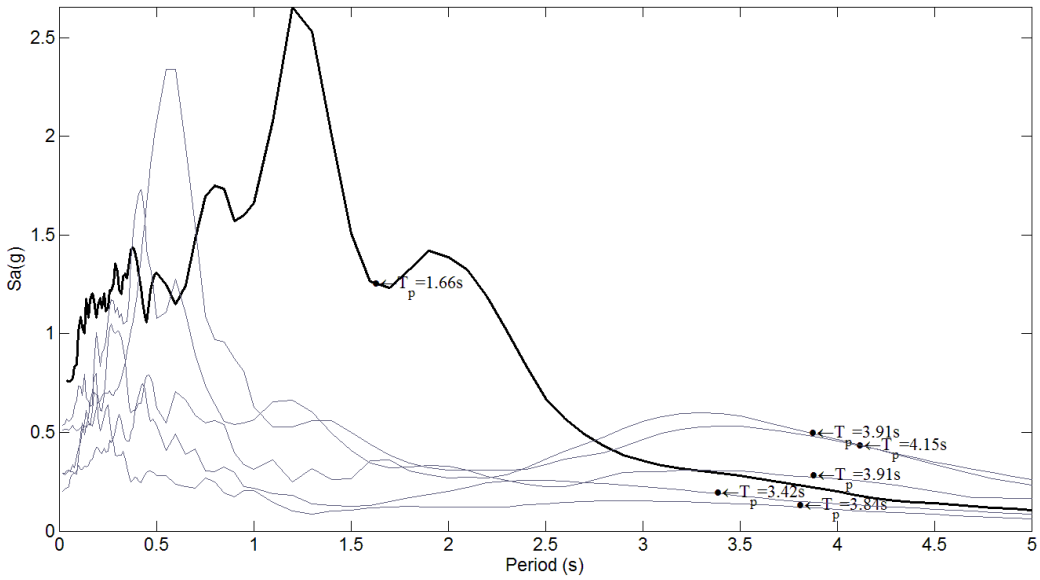

Figure A1.18: Response spectra of recorded (black) and simulated (grey) near-fault ground motions

2. NGA RECORD # 1605:

- Recorded at the Duzce station during the 1999 Duzce earthquake in Turkey.
- F = 1, M_w = 7.14, R = 6.6km, V_{s30} = 276m/s, θ = 25.3°, and s = 1.45km.

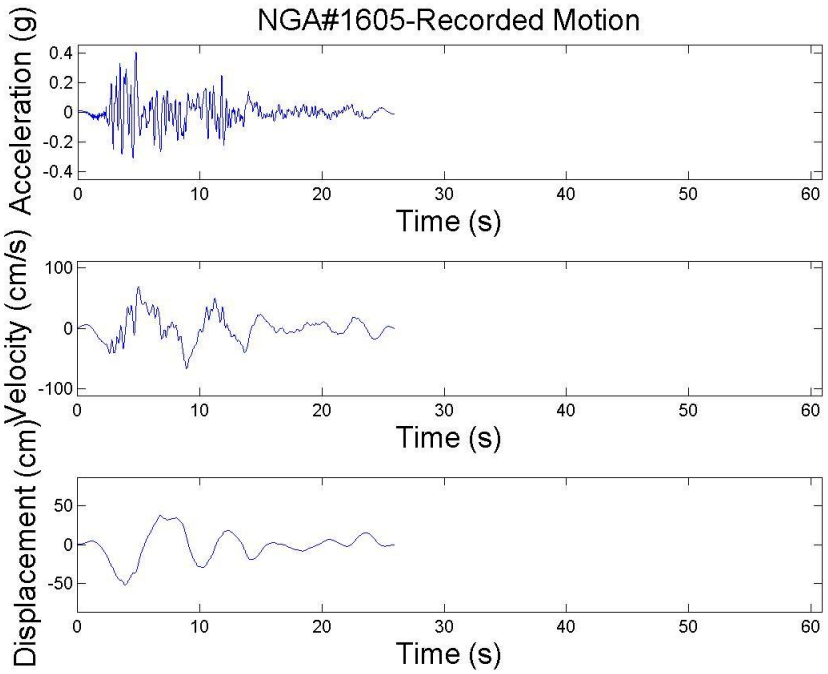

Figure A2.1: Acceleration, velocity and displacement time histories of NGA record #1605

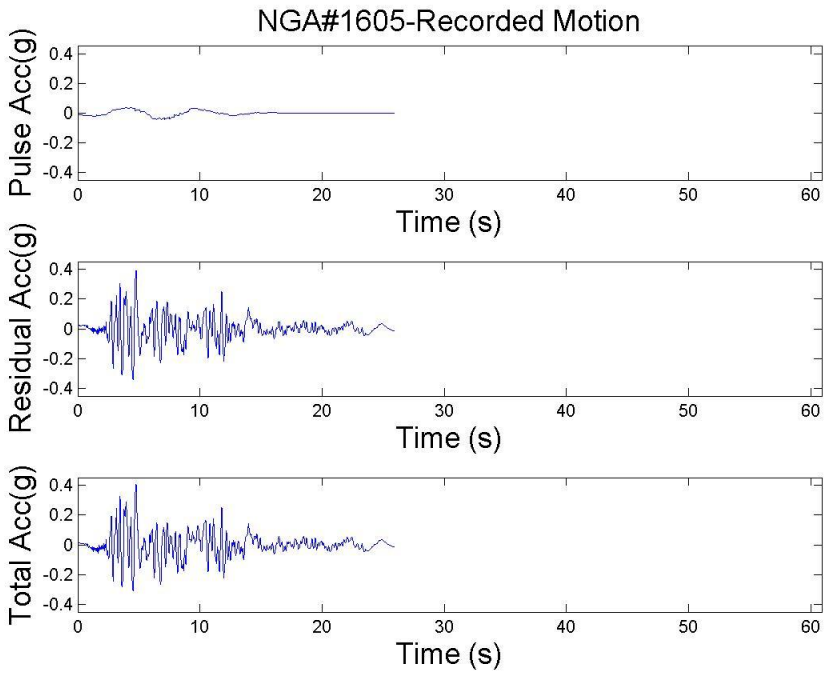

Figure A2.2: Acceleration time history (bottom), derivative of extracted velocity pulse (top), and residual acceleration time history (middle) of NGA record #1605

Table A2.1: Parameters of the recorded and simulated pulses for prescribed earthquake source and site characteristics

	V_p	T_p	γ	ν/π	$t_{max,p}$	$T_{p,\text{wavelet}}$	PI	PulseLike?
	cm/s	s		rad	s	s		
Median	50.3	4.52	2.40	1.00	10.46			
Recorded	41.7	6.41	3.12	0.70	6.17	5.96		Y
Simulation 1	66.6	3.21	2.24	1.87	10.64	3.40	1.00	Y
Simulation 2	40.0	4.41	2.39	0.18	12.03	4.97	1.00	Y
Simulation 3	49.6	4.55	2.13	1.80	11.97	5.25	1.00	Y
Simulation 4	25.7	6.18	2.47	1.22	12.45	7.03	1.00	N
Simulation 5	86.2	5.17	2.38	1.40	13.16	6.44	1.00	Y

Table A2.2: Parameters of the recorded and simulated residuals for prescribed earthquake source and site characteristics

	$I_a/(\frac{\pi}{2g})$	D_{5-95}	t_{30}	$t_{max,r}$	ω_{mid}	ω'	ζ_f
	g^2s	s	s	s	Hz	Hz/s	
Median	0.066	18.3	9.66	10.15	3.48	-6.06 E-02	0.343
Recorded	0.168	11.2	3.49	3.53	2.23	1.68 E-02	0.141
Simulation1	0.094	17.4	7.69	8.42	3.54	0.23 E-02	0.361
Simulation2	0.010	19.9	11.66	16.43	3.49	-14.3 E-02	0.291
Simulation3	0.100	18.7	11.35	11.46	6.75	-22.0 E-02	0.159
Simulation4	0.030	20.3	10.96	11.15	3.78	-13.4 E-02	0.170
Simulation5	0.210	17.5	10.11	10.51	2.18	0.25 E-02	0.364

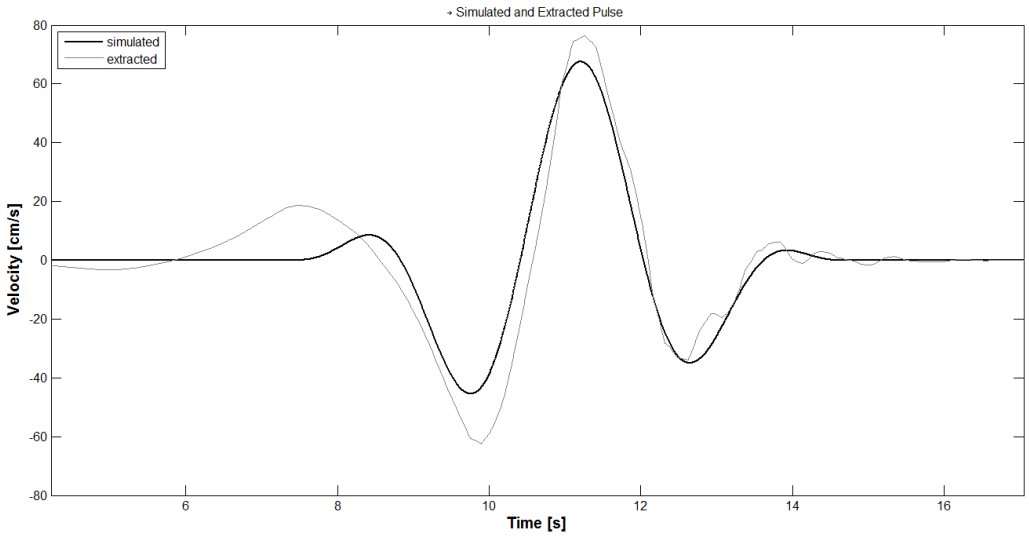

Figure A2.3: Simulated mMP velocity pulse #1 (black line) and extracted pulse from total simulated motion #1 (grey line)

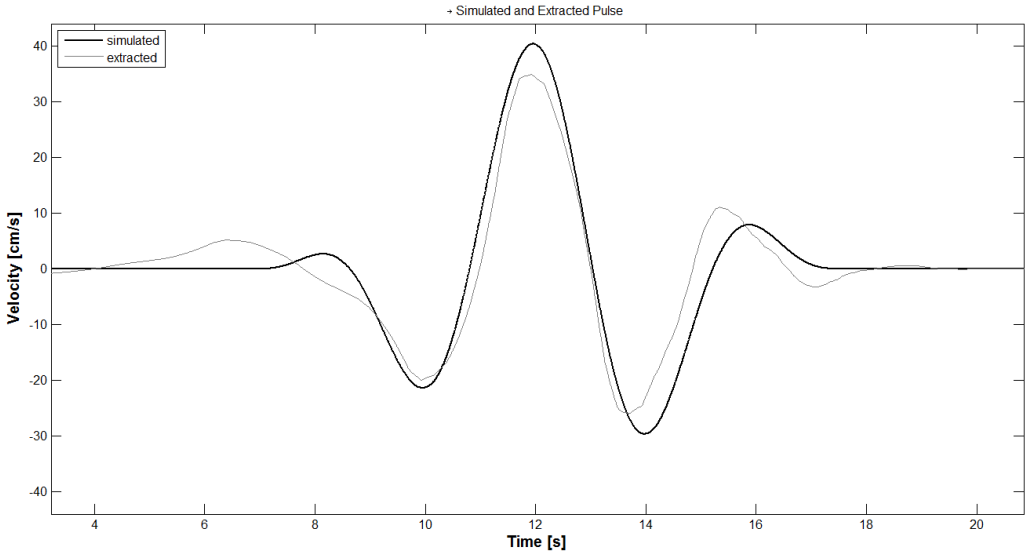

Figure A2.4: Simulated mMP velocity pulse #2 (black line) and extracted pulse from total simulated motion #2 (grey line)

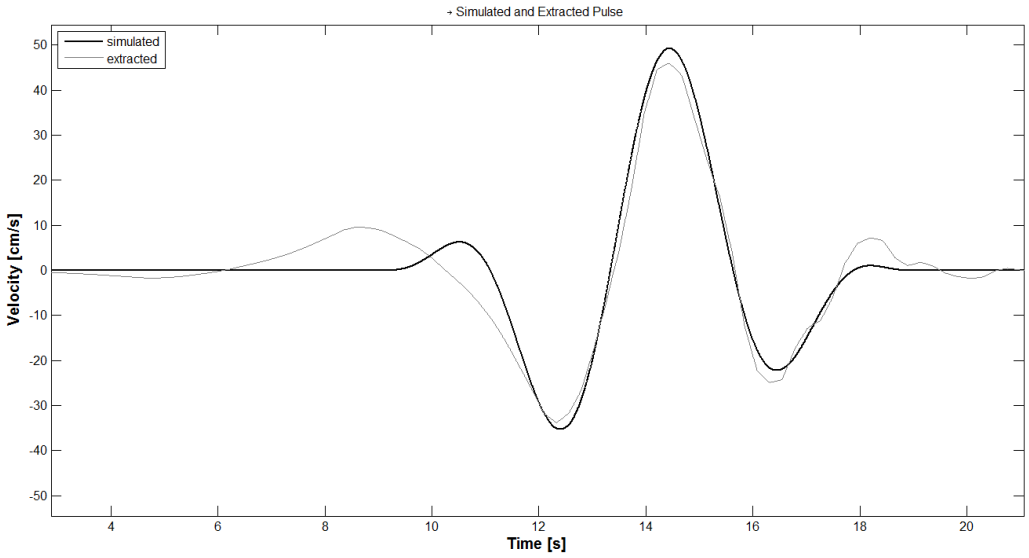

Figure A2.5: Simulated mMP velocity pulse #3 (black line) and extracted pulse from total simulated motion #3 (grey line)

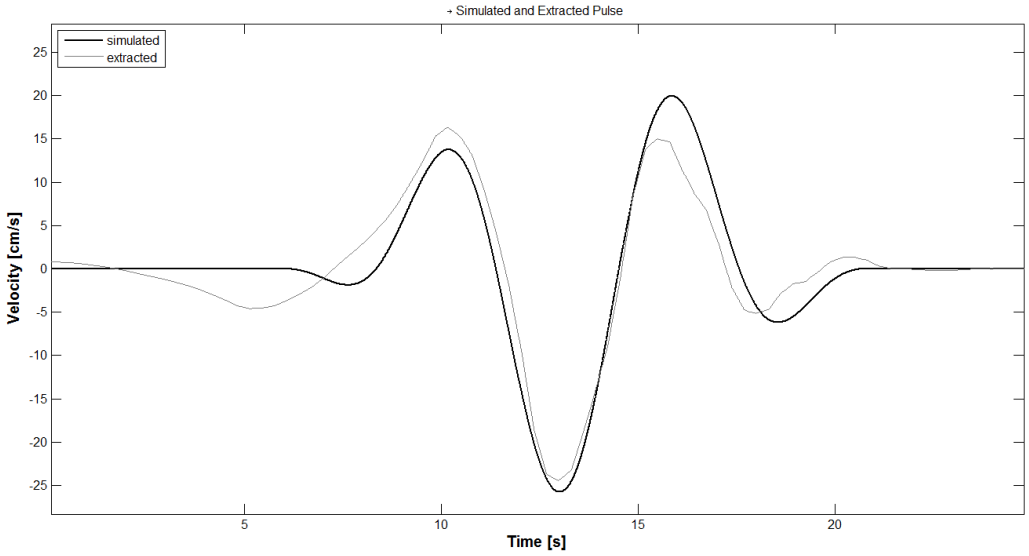

Figure A2.6: Simulated mMP velocity pulse #4 (black line) and extracted pulse from total simulated motion #4 (grey line)

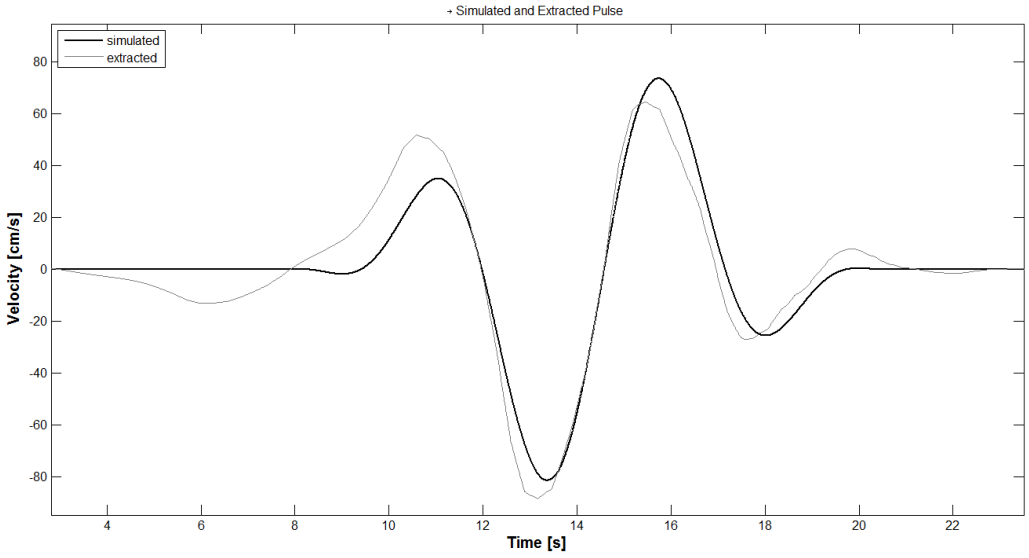

Figure A2.7: Simulated mMP velocity pulse #5 (black line) and extracted pulse from total simulated motion #5 (grey line)

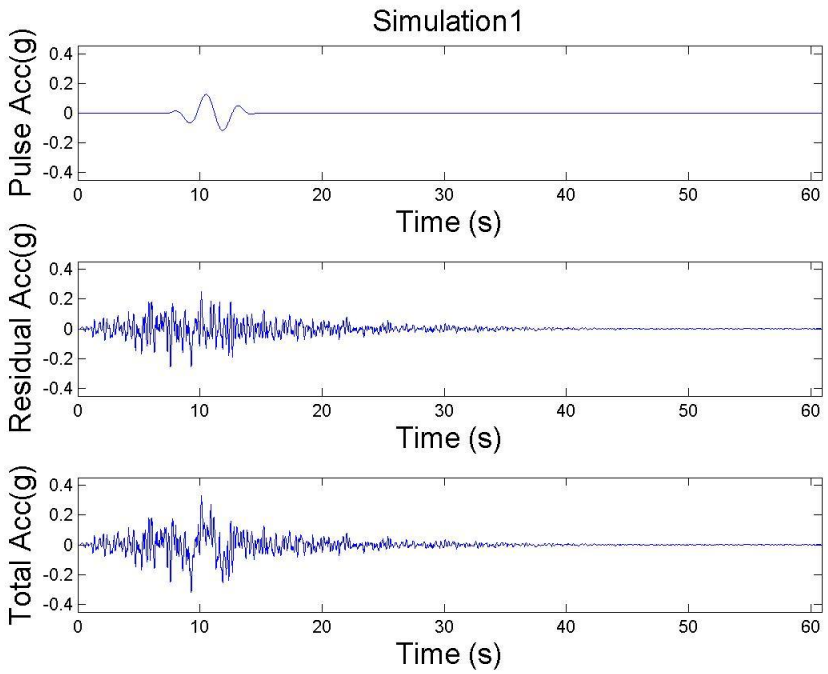

Figure A2.8: Simulated Motion 1: derivative of simulated pulse (top), simulated residual motion (middle) and total simulated acceleration record (bottom)

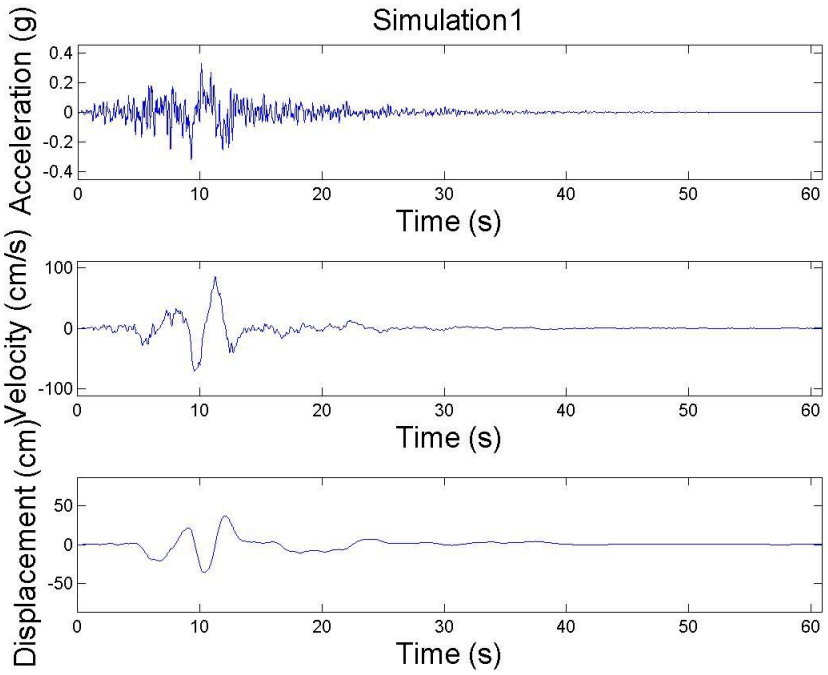

Figure A2.9: Simulated Motion 1: acceleration, velocity and displacement time histories

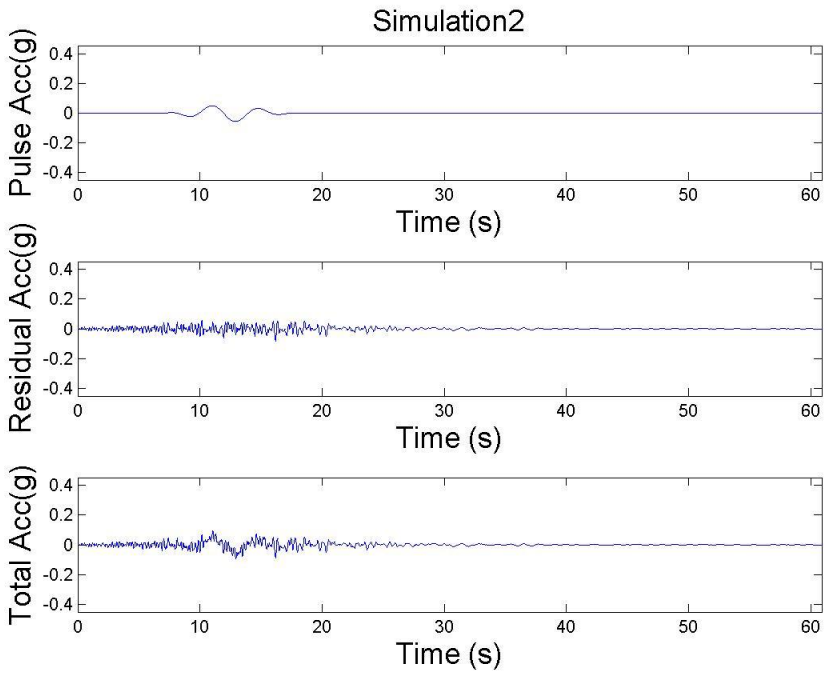

Figure A2.10: Simulated Motion 2: derivative of simulated pulse (top), simulated residual motion (middle) and total simulated acceleration record (bottom)

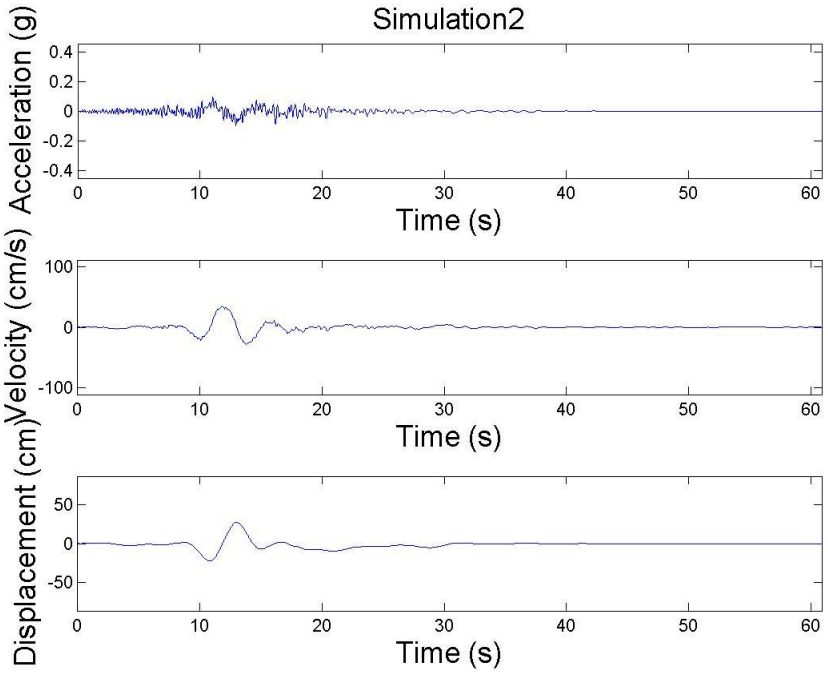

Figure A2.11: Simulated Motion 2: acceleration, velocity and displacement time histories

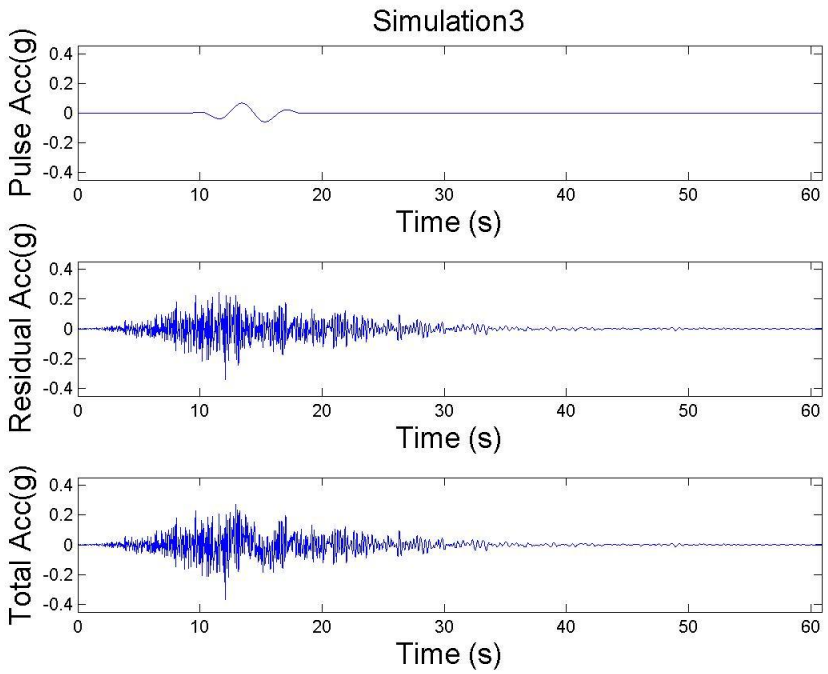

Figure A2.12: Simulated Motion 3: derivative of simulated pulse (top), simulated residual motion (middle) and total simulated acceleration record (bottom)

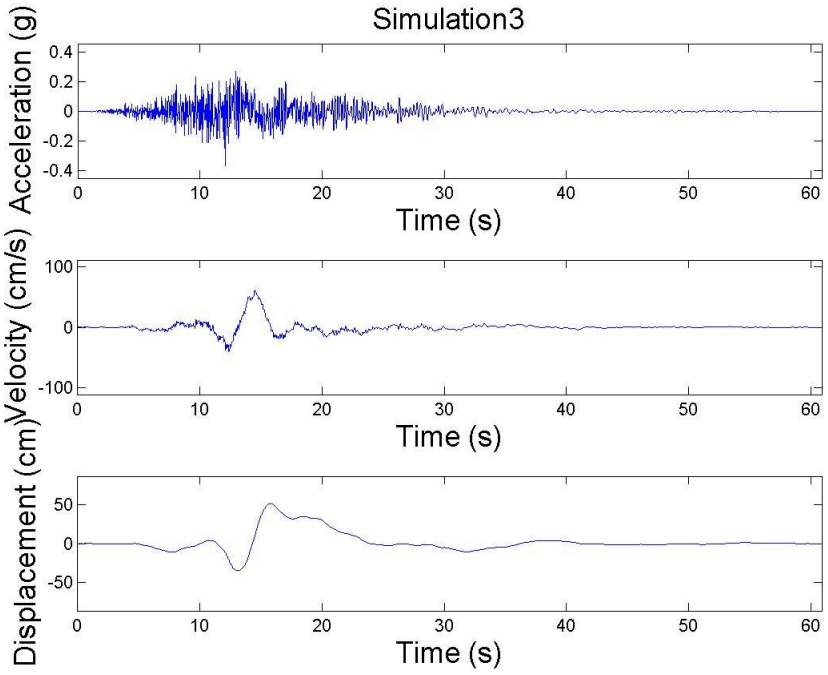

Figure A2.13: Simulated Motion 3: acceleration, velocity and displacement time histories

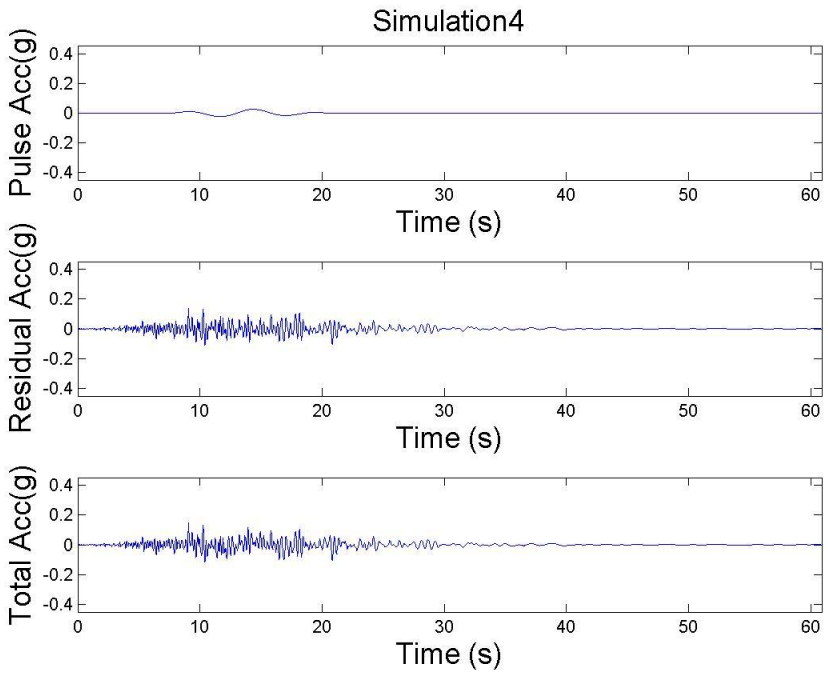

Figure A2.14: Simulated Motion 4: derivative of simulated pulse (top), simulated residual motion (middle) and total simulated acceleration record (bottom)

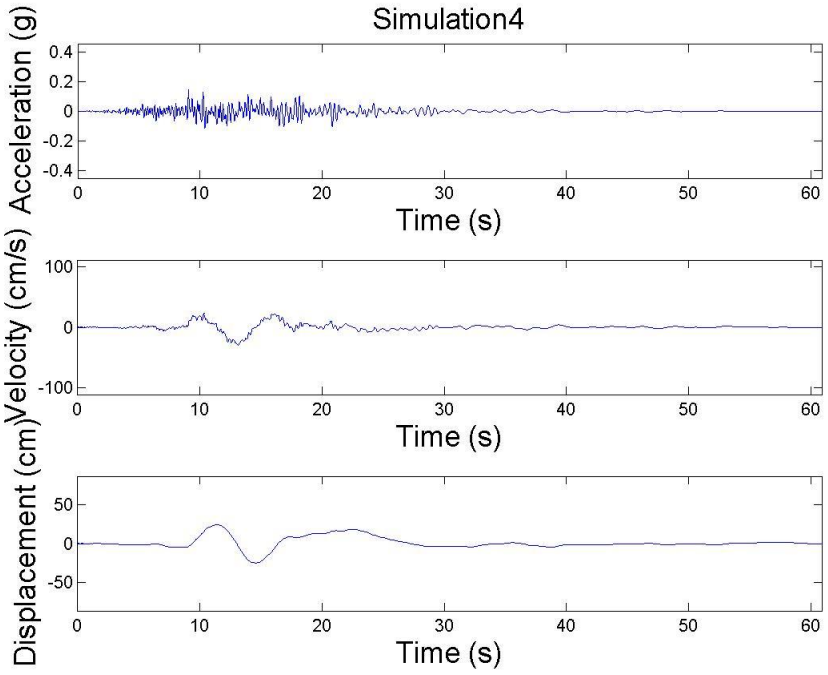

Figure A2.15: Simulated Motion 4: acceleration, velocity and displacement time histories

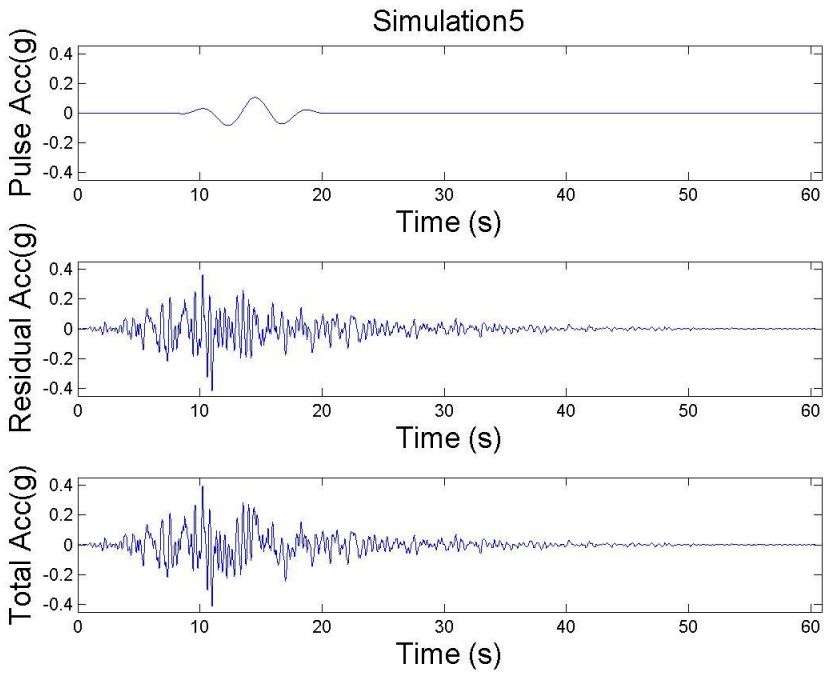

Figure A2.16: Simulated Motion 5: derivative of simulated pulse (top), simulated residual motion (middle) and total simulated acceleration record (bottom)

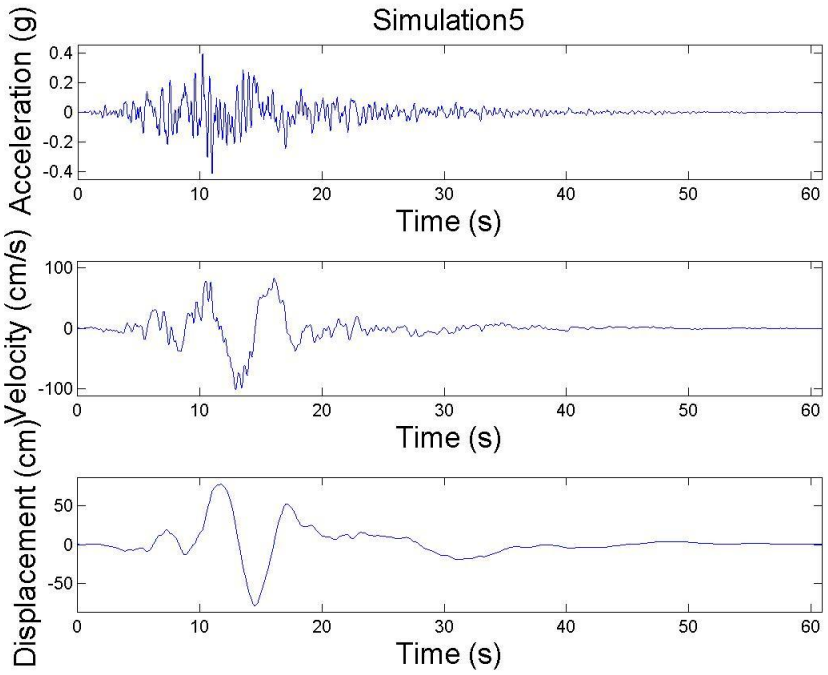

Figure A2.17: Simulated Motion 5: acceleration, velocity and displacement time histories

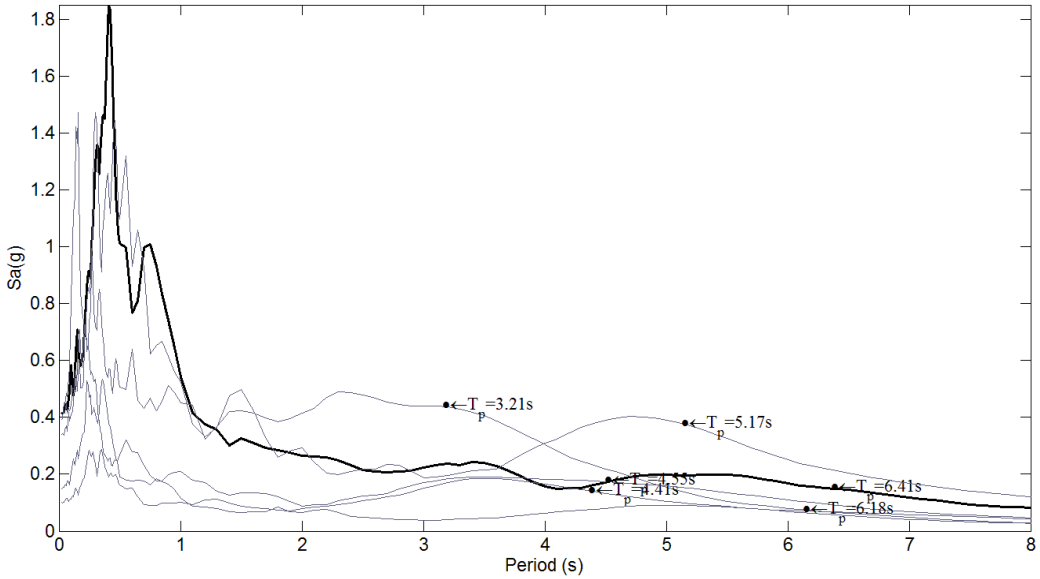

Figure A2.18: Response spectra of recorded (black) and simulated (grey) near-fault ground motions

3. NGA RECORD # 4100:

- Recorded at the Parkfield-Cholame 2WA station during the 2004 Parkfield California earthquake.
- F = 1, M_w = 6.0, R = 3.0km, V_{s30} = 184.8m/s, θ = 3.1°, and s = 10km.

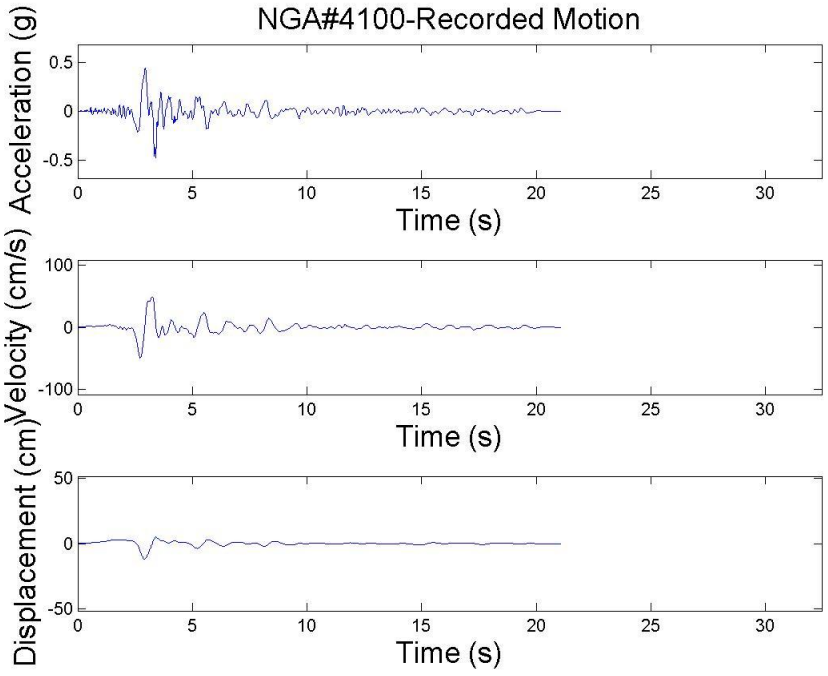

Figure A3.1: Recorded Acceleration, velocity and displacement time histories of NGA record #4100

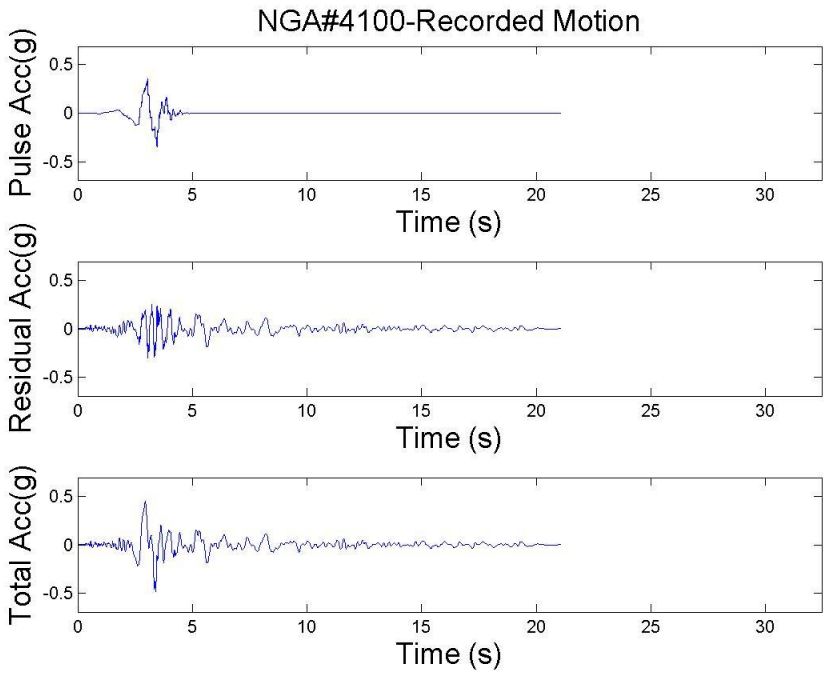

Figure A3.2: Acceleration time history (bottom), derivative of extracted velocity pulse (top), and residual acceleration time history (middle) of NGA record #4100

Table A3.1: Parameters of the recorded and simulated pulses for prescribed earthquake source and site characteristics

	V_p	T_p	γ	ν/π	$t_{max,p}$	$T_{p,\text{wavelet}}$	PI	PulseLike?
	cm/s	s		rad	s	s		
Median	46.6	1.39	2.24	1.00	2.99			
Recorded	46.2	1.05	2.12	-0.92	3.04	1.08		
Simulation 1	37.4	1.52	2.07	0.69	3.32	8.38	0.14	N
Simulation 2	89.9	0.86	2.06	0.17	2.17	1.10	1.00	Y
Simulation 3	36.8	1.67	2.26	1.42	5.35	1.97	0.97	N
Simulation 4	38.7	1.80	2.31	0.59	3.10	1.90	1.00	Y
Simulation 5	45.6	1.89	2.22	1.05	2.65	2.29	1.00	Y

Table A3.2: Parameters of the recorded and simulated residuals for prescribed earthquake source and site characteristics

	$I_a/(\frac{\pi}{2g})$	D_{5-95}	t_{30}	$t_{max,r}$	ω_{mid}	ω'	ζ_f
	g^2s	s	s	s	Hz	Hz/s	
Median	0.057	7.00	2.58	2.50	4.36	-15.0 E-02	0.390
Recorded	0.058	8.85	3.00	3.02	2.66	2.06 E-02	0.366
Simulation1	0.084	8.93	3.40	2.36	3.43	-22.9 E-02	0.679
Simulation2	0.055	6.73	2.62	3.48	3.26	-15.1 E-02	0.440
Simulation3	0.062	8.96	3.96	2.99	5.22	-44.2 E-02	0.172
Simulation4	0.050	10.8	2.73	2.69	5.41	-34.7 E-02	0.193
Simulation5	0.094	4.94	2.52	2.53	5.23	-5.75 E-02	0.365

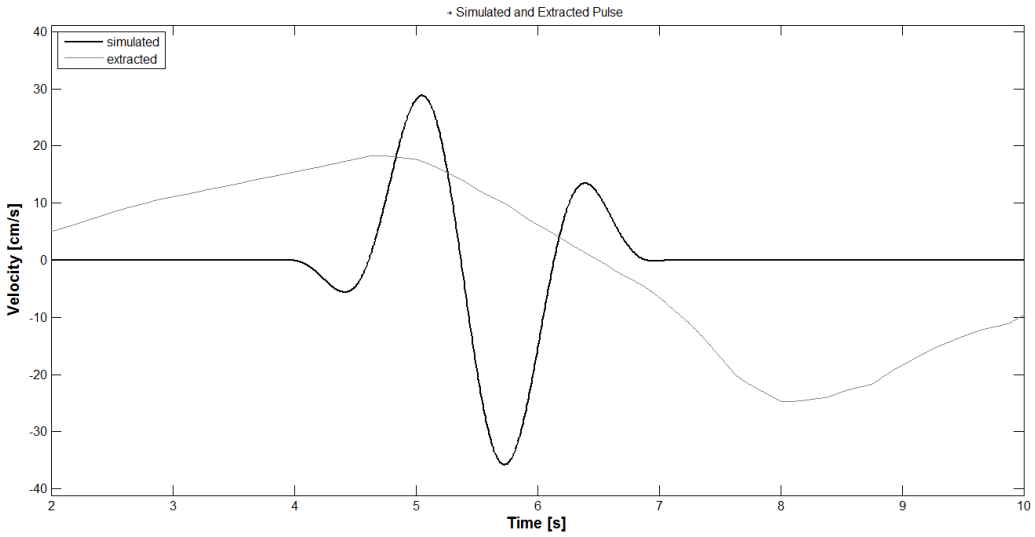

Figure A3.3: Simulated mMP velocity pulse #1 (black line) and extracted pulse from total simulated motion #1 (grey line)

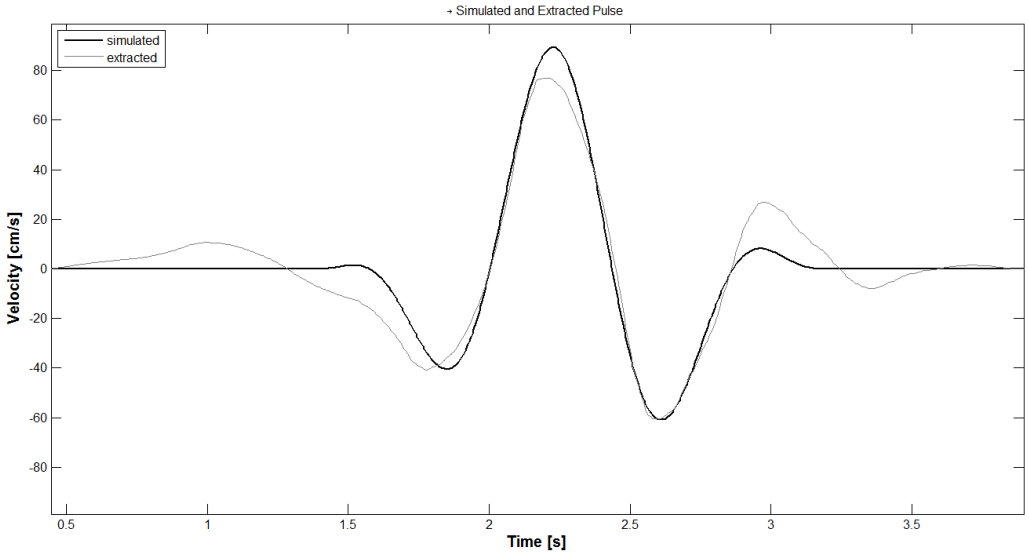

Figure A3.4: Simulated mMP velocity pulse #2 (black line) and extracted pulse from total simulated motion #2 (grey line)

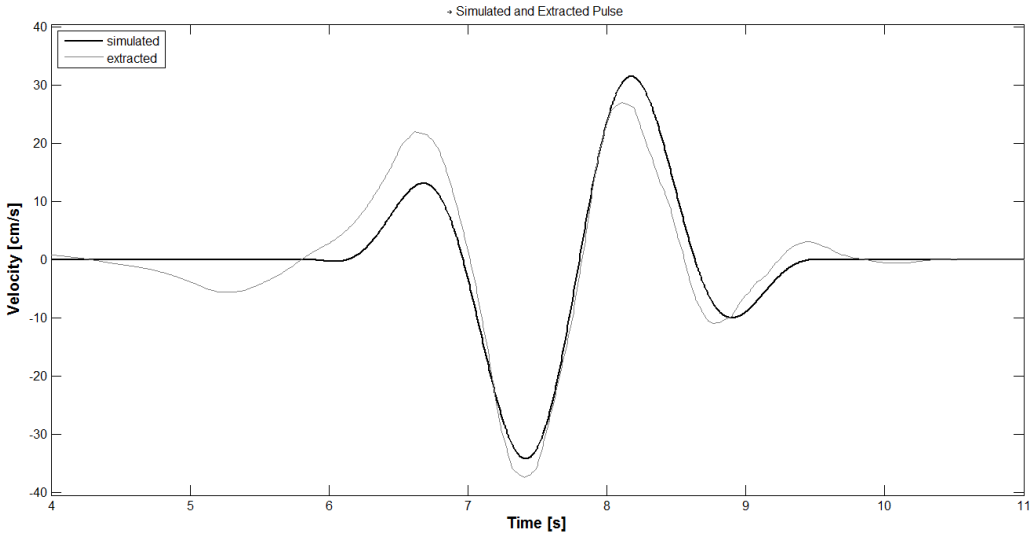

Figure A3.5: Simulated mMP velocity pulse #3 (black line) and extracted pulse from total simulated motion #3 (grey line)

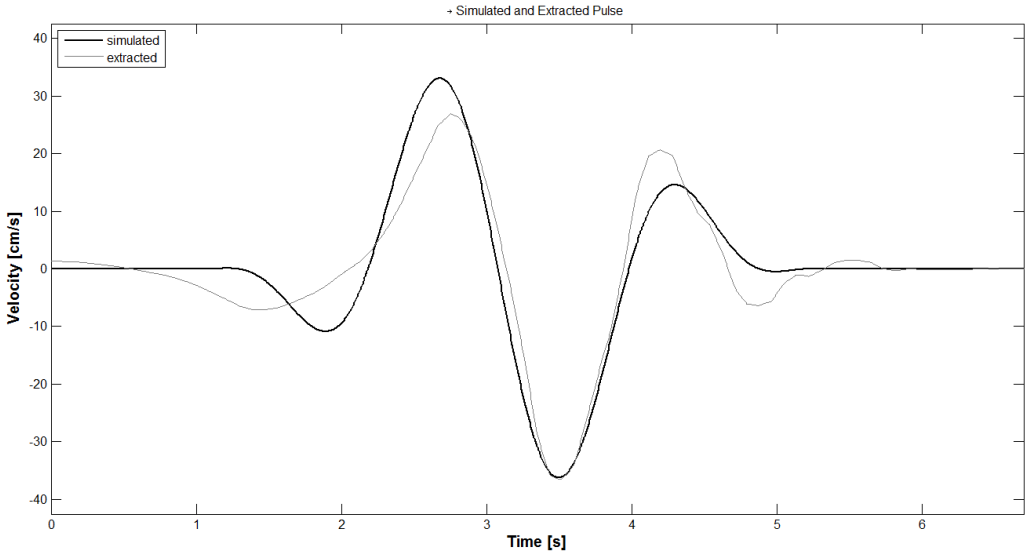

Figure A3.6: Simulated mMP velocity pulse #4 (black line) and extracted pulse from total simulated motion #4 (grey line)

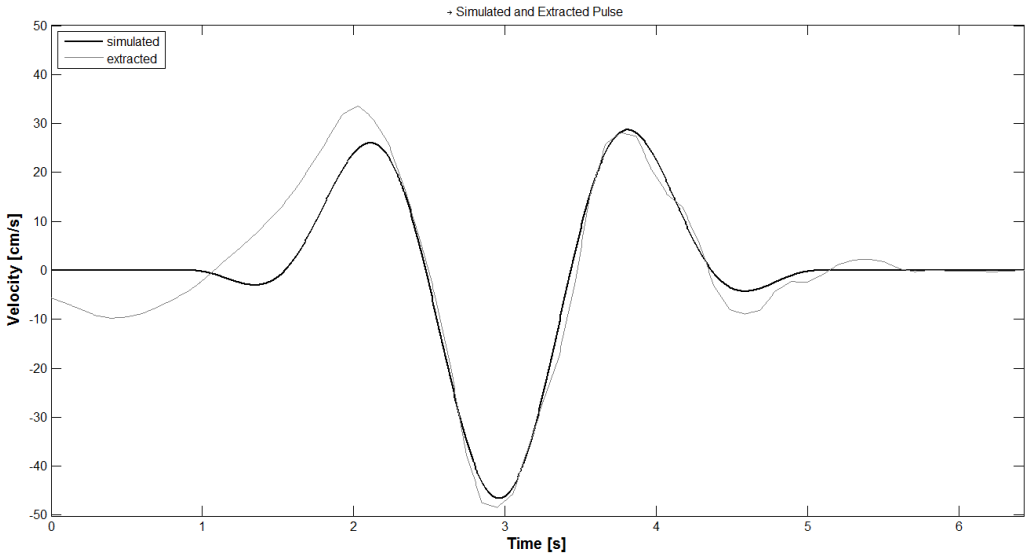

Figure A3.7: Simulated mMP velocity pulse #5 (black line) and extracted pulse from total simulated motion #5 (grey line)

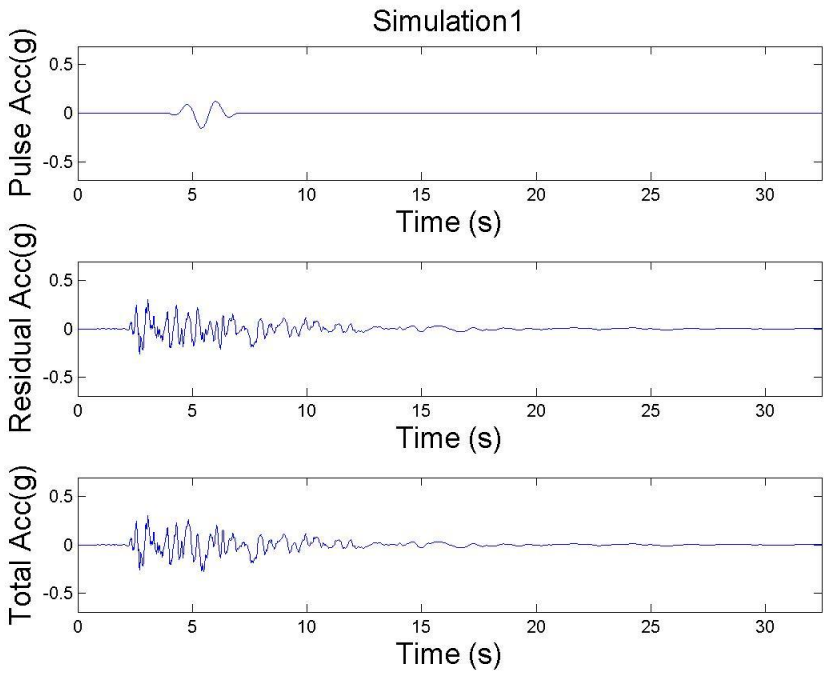

Figure A3.8: Simulated Motion 1: derivative of simulated pulse (top), simulated residual motion (middle) and total simulated acceleration record (bottom)

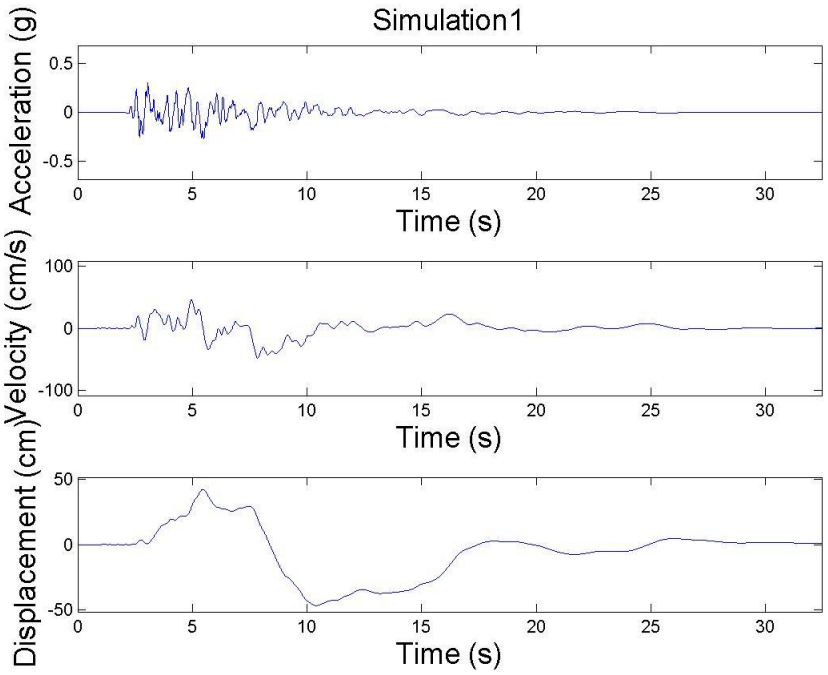

Figure A3.9: Simulated Motion 1: acceleration, velocity and displacement time histories

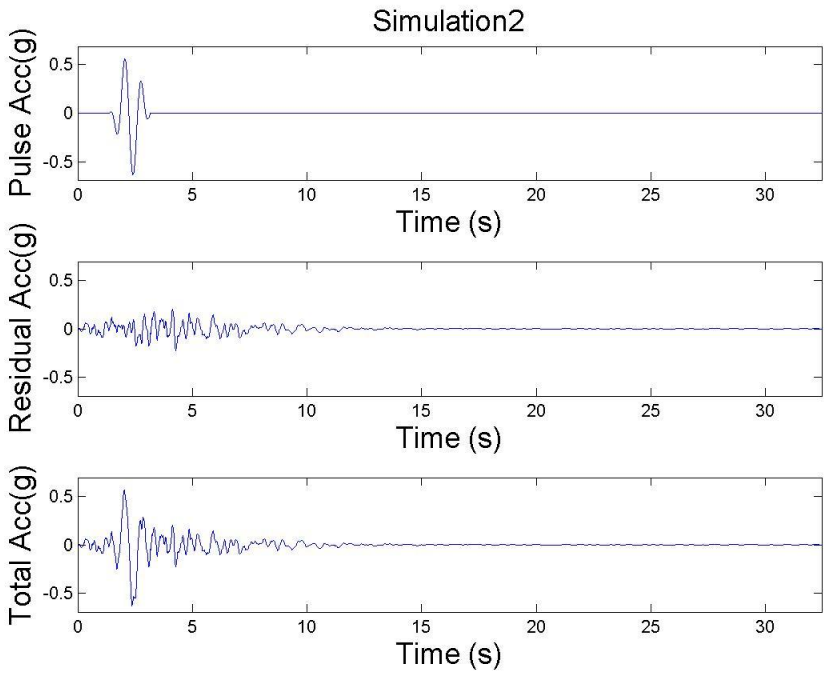

Figure A3.10: Simulated Motion 2: derivative of simulated pulse (top), simulated residual motion (middle) and total simulated acceleration record (bottom)

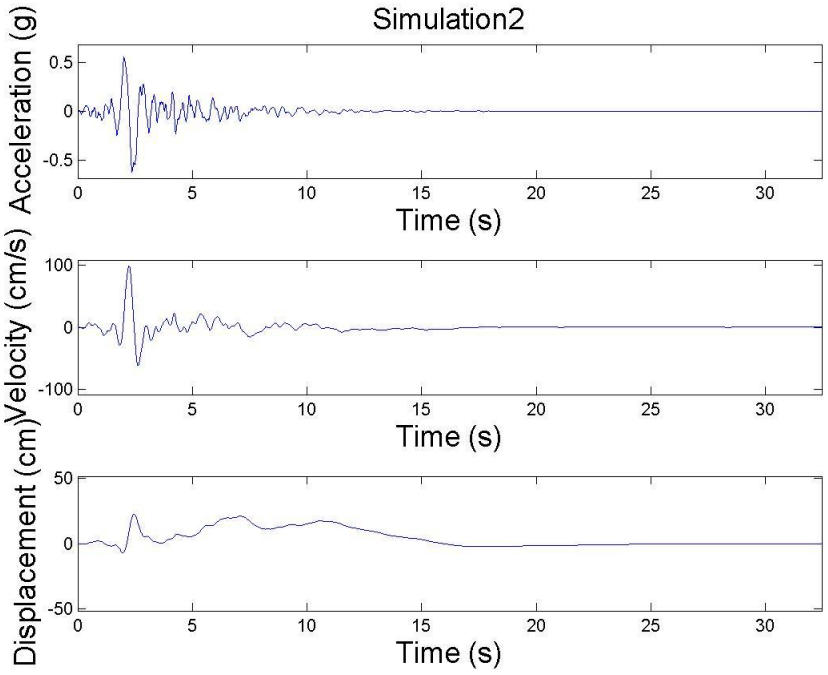

Figure A3.11: Simulated Motion 2: acceleration, velocity and displacement time histories

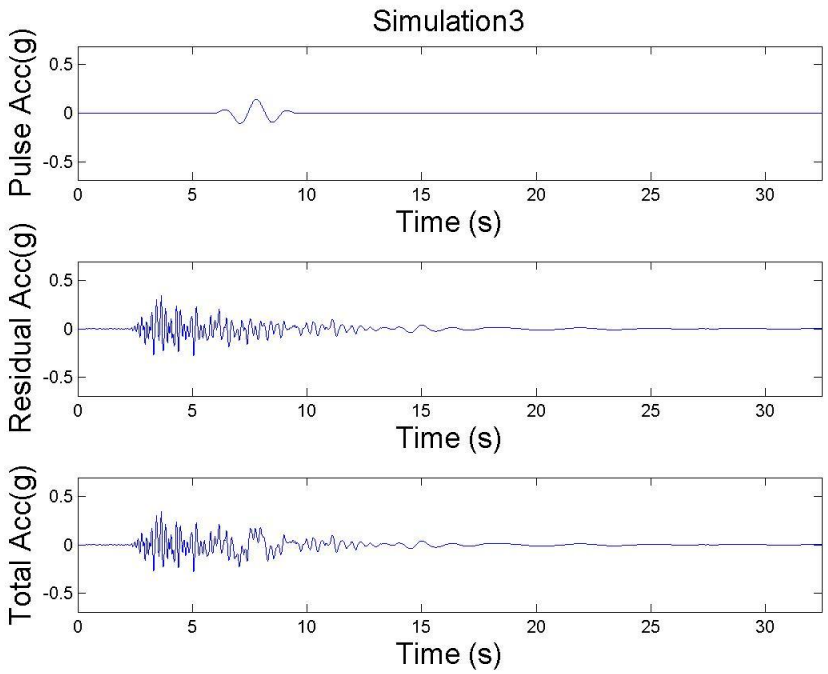

Figure A3.12: Simulated Motion 3: derivative of simulated pulse (top), simulated residual motion (middle) and total simulated acceleration record (bottom)

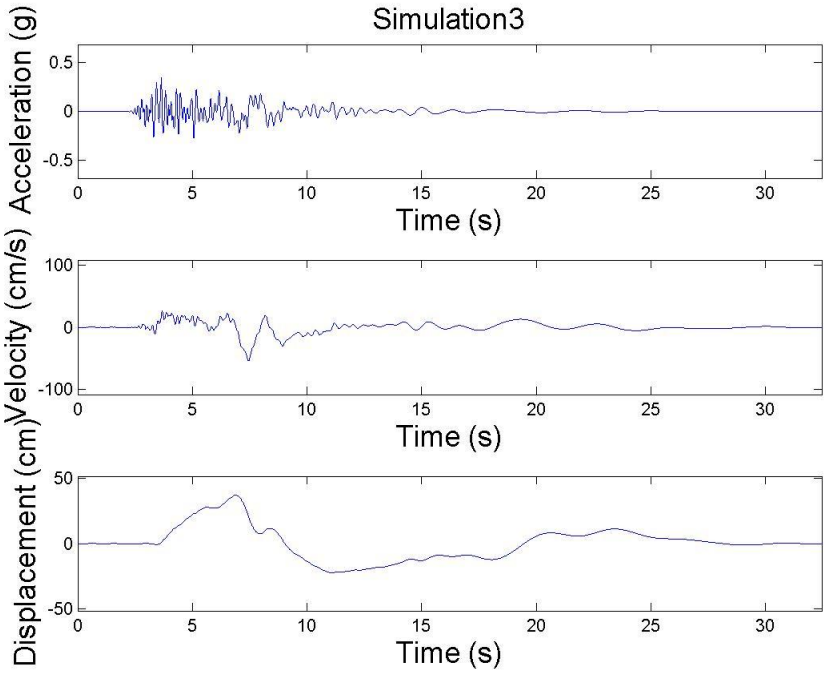

Figure A3.13: Simulated Motion 3: acceleration, velocity and displacement time histories

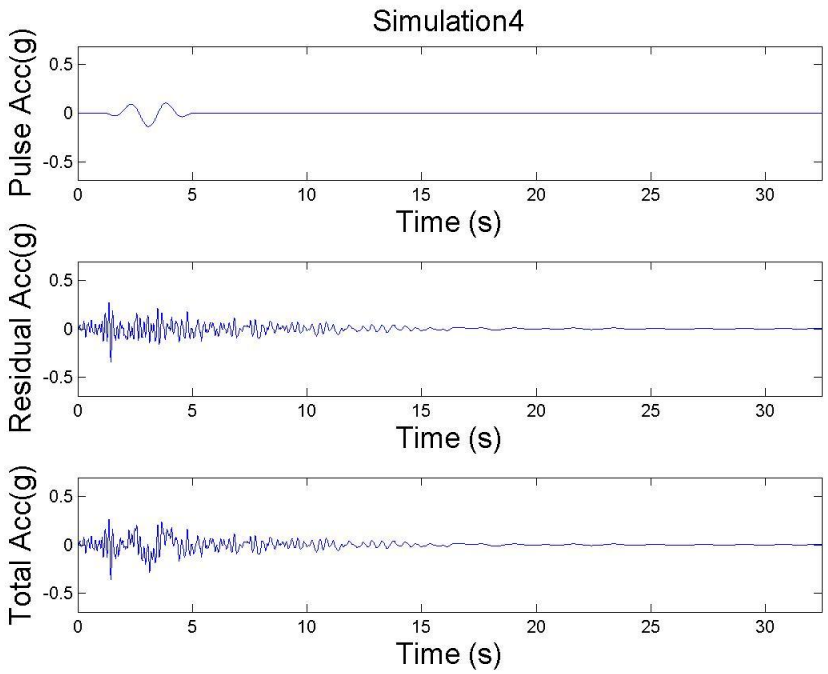

Figure A3.14: Simulated Motion 4: derivative of simulated pulse (top), simulated residual motion (middle) and total simulated acceleration record (bottom)

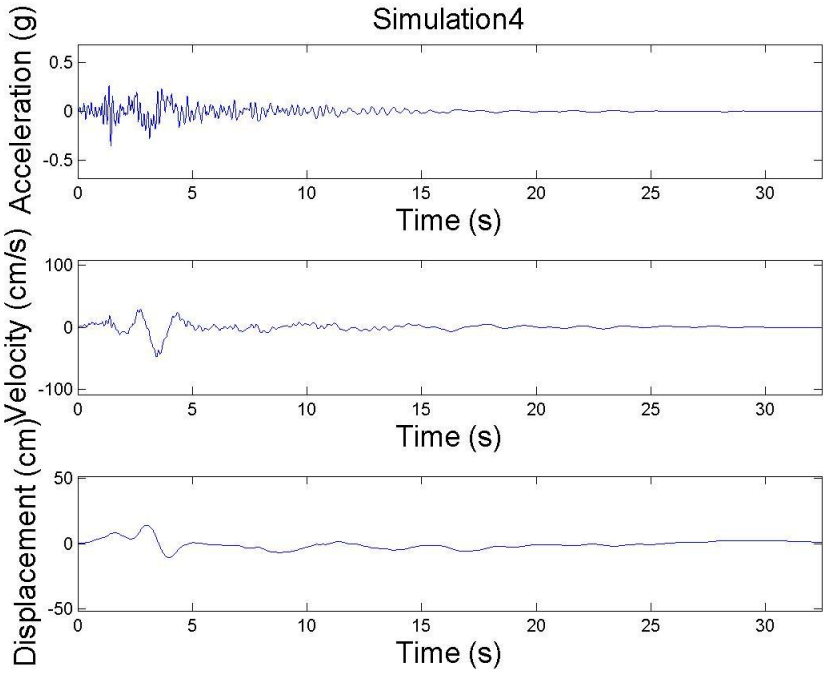

Figure A3.15: Simulated Motion 4: acceleration, velocity and displacement time histories

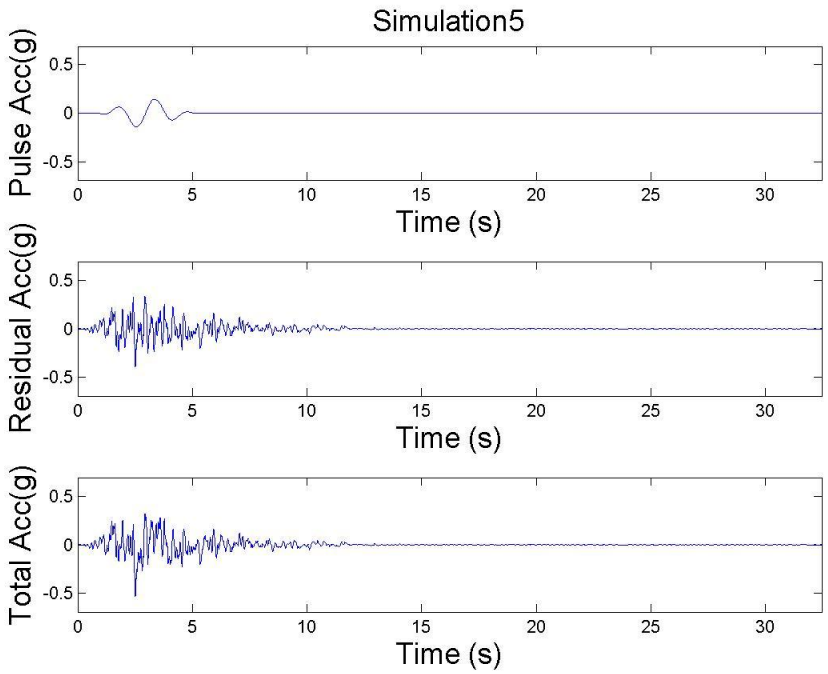

Figure A3.16: Simulated Motion 5: derivative of simulated pulse (top), simulated residual motion (middle) and total simulated acceleration record (bottom)

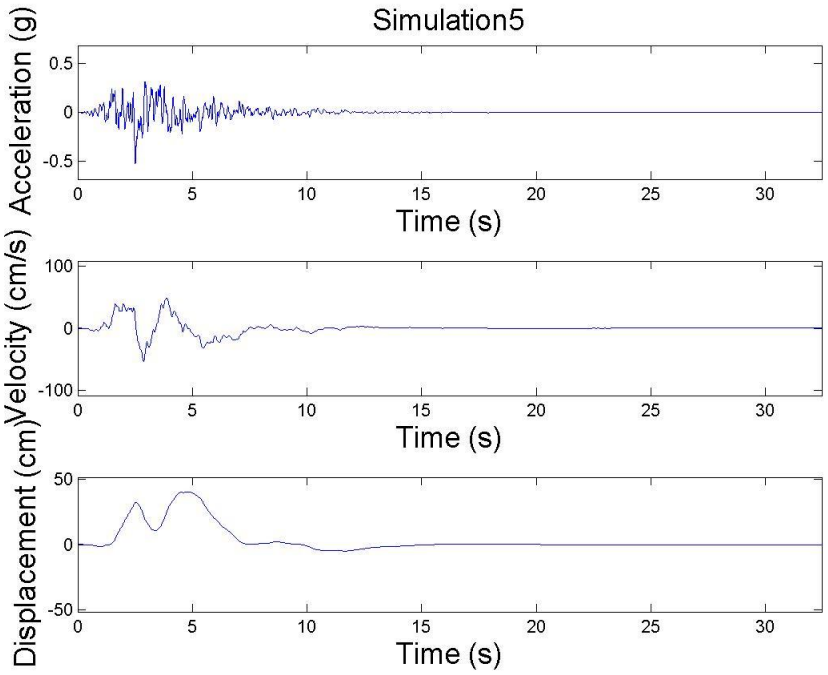

Figure A3.17: Simulated Motion 5: acceleration, velocity and displacement time histories

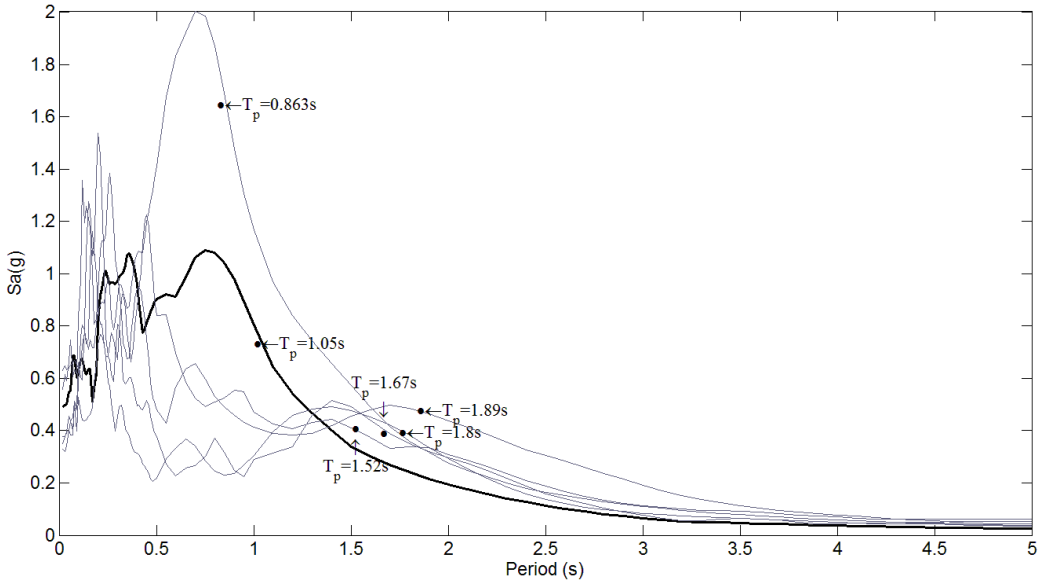

Figure A3.18: Response spectra of recorded (black) and simulated (grey) near-fault ground motions